Optical Communications for Small Satellites

by

Ryan W. Kingsbury

B.S., Rose-Hulman Institute of Technology (2004)

S.M., Massachusetts Institute of Technology (2009)

Submitted to the Department of Aeronautics and Astronautics
in partial fulfillment of the requirements for the degree of

Doctor of Philosophy in Communications and Networking

at the

MASSACHUSETTS INSTITUTE OF TECHNOLOGY

September 2015

© Massachusetts Institute of Technology 2015. All rights reserved.

Author . . . .
Department of Aeronautics and Astronautics
August 6, 2015

Certified by. . . . .
Kerri L. Cahoy
Assistant Professor of Aeronautics and Astronautics
Thesis Supervisor

Certified by. . . . .
David W. Miller
Professor of Aeronautics and Astronautics

Certified by. . . . .
David O. Caplan
Senior Technical Staff, MIT Lincoln Laboratory

Certified by. . . . .
Jonathan C. Twichell
Senior Technical Staff, MIT Lincoln Laboratory

Accepted by . . . .
Paulo C. Lozano
Associate Professor of Aeronautics and Astronautics
Chair, Graduate Program Committee

Optical Communications for Small Satellites

by

Ryan W. Kingsbury

Submitted to the Department of Aeronautics and Astronautics
on August 6, 2015, in partial fulfillment of the
requirements for the degree of
Doctor of Philosophy in Communications and Networking

Abstract

Small satellites, particularly CubeSats, have become popular platforms for a wide variety of scientific, commercial and military remote sensing applications. Inexpensive commercial off the shelf (COTS) hardware and relatively low launch costs make these platforms candidates for deployment in large constellations that can offer unprecedented temporal and geospatial sampling of the entire planet. However, productivity for both individual and constellations of CubeSats in low earth orbit (LEO) is limited by the capabilities of the communications subsystem. Generally, these constraints stem from limited available electrical power, low-gain antennas and the general scarcity of available radio spectrum.

In this thesis, we assess the ability of free space optical communication (lasercom) to address these limitations, identify key technology developments that enable its application in small satellites, and develop a functional prototype that demonstrates predicted performance. We first establish design goals for a lasercom payload architecture that offers performance improvements (joules-per-bit) over radio-frequency (RF) solutions, yet is compatible with the severe size, weight and power (SWaP) constraints common to CubeSats. The key design goal is direct LEO-to-ground downlink capability with data rates exceeding 10 Mbps, an order of magnitude better than COTS radio solutions available today, within typical CubeSat SWaP constraints on the space terminal, and with similar COTS and low-complexity constraints on the ground terminal. After defining the goals for this architecture, we identify gaps in previous implementations that limit their performance: the lack of compact, power-efficient optical transmitters and the need for pointing capability on small satellites to be as much as a factor of ten better than what is commonly achieved today.

One approach is to address these shortcomings using low-cost COTS components that are compatible with CubeSat budgets and development schedules. In design trade studies we identify potential solutions for the transmitter and pointing implementation gaps. Two distinct transmitter architectures, one based on a high-power laser diode and another using an optical amplifier, are considered. Analysis shows that both configurations meet system requirements, however, the optical amplifier offers better scalability to higher data rates. To address platform pointing limitations, we define a staged control framework incorporating a COTS optical steering mechanism that is used to manage pointing errors from the coarse stage (host satellite body-pointing). A variety of fine steering solutions are considered, and microelec-

tromechanical systems (MEMS) tip-tilt mirrors are selected due to their advantage in size, weight and power.

We experimentally validate the designs resulting from the trade studies for these key subsystems. We construct a prototype transmitter using a modified COTS fiber amplifier and a directly-modulated seed laser capable of producing a 200 mW average power, pulse position modulated optical output. This prototype is used to confirm power consumption predictions, modulation rate scalability (10 Mbps to 100 Mbps), and peak transmit power (e.g., 24.6 W for PPM-128). The transmitter optical output, along with a simple loopback receiver, is used to validate the sensitivity of the avalanche photodiode receiver used for the ground receiver in the flight experiment configuration. The MEMS fine steering mechanisms, which are not rated for space use, are characterized using a purpose-built test apparatus. Characterization experiments of the MEMS devices focused on ensuring repeatable behavior (± 0.11 mrad, 3-σ) over the expected operating temperature range on the spacecraft (0 °C to 40 °C). Finally, we provide an assessment of the work that remains to move from the prototype to flight model and into on-orbit operations. Space terminal packaging and integration needs, as well as host spacecraft interface requirements are detailed. We also describe the remaining ground station integration tasks and operational procedures.

Having developed a pragmatic COTS-based lasercom architecture for CubeSats, and having addressed the need for a compact laser transmitter and optical fine steering mechanisms with both analysis and experimental validation, this thesis has set the stage for the practical use of lasercom techniques in resource-constrained CubeSats which can yield order-of-magnitude enhancements in communications link efficiency relative to existing RF technologies currently in use.

Thesis Supervisor: Kerri L. Cahoy
Title: Assistant Professor of Aeronautics and Astronautics

Thesis Committee Member: David W. Miller
Title: Professor of Aeronautics and Astronautics

Thesis Committee Member: David O. Caplan
Title: Senior Technical Staff, MIT Lincoln Laboratory

Thesis Committee Member: Jonathan C. Twichell
Title: Senior Technical Staff, MIT Lincoln Laboratory

Acknowledgments

First and foremost I would like to thank my thesis advisor, Prof. Kerri Cahoy, for her guidance and support that have led me through the last three years. I am continually impressed with her tireless work ethic and devotion to her students. Perhaps most importantly, I'm thankful that she has given me the latitude to explore topics which interest me even if they didn't directly align with existing research efforts.

I am also grateful to the rest of my thesis committee and mentors whose advice and suggestions have formed the very core of what I have learned while writing this dissertation. Jonathan Twichell, William Farr and Malcolm Wright have all provided me with great insight into a variety of cross-domain design trades which are difficult to grasp from the literature alone. David Caplan has provided me an enormous amount of advice and practical suggestions for the transmitter design and his strong belief in the value of experimental results have positively shaped this work. Prof. David Miller's very pragmatic approach to control system design and implementation has also come in especially helpful to someone like myself who was trying to tackle a controls-heavy problem with a dearth of controls experience.

Next, I would like to acknowledge the funding sources which made this project and my PhD studies possible. MIT Lincoln Laboratory generously provided academic funding during my first year as a PhD student and put me at the center of MIT's first CubeSat mission, MicroMAS. It was the MicroMAS mission that piqued my interest in CubeSat communications systems. The NASA Space Technology Research Fellowship program(Grant NNX13AM69H) for generously covering my academic expenses over the last two years, and for providing me with an excellent on-site opportunity with the Jet Propulsion Laboratory's Optical Communications Group. And finally, a grant from the Jet Propulsion Laboratory's Strategic University Research Partnership program that made the experimental aspects of this thesis a reality.

I am grateful beyond words to Amy for moving to Boston with me so that I could pursue this dream. Her companionship and devotion are what enabled me to make it through this stressful phase of my life. I can't wait to see what the future holds in store for us.

Finally I want to express my deepest appreciation to my family for their love and support over the years.

Contents

List of Figures

9

List of Tables

List of Acronyms

ADC Analog to Digital Converter

ADCS Attitude Determination and Control System

APD Avalanche Photodiode

ASIC Application-Specific Integrated Circuit

AWGN Additive White Gaussian Noise

BER Bit Error Rate

BIST Built-In Self-Test

BW Bandwidth

CCD Charge-Coupled Device

CDR Clock and Data Recovery

COTS Commercial Off The Shelf

CRC Cyclic Redundancy Check

CW Continuous Wave

DAC Digital to Analog Converter

DC Direct Current

DOD Department of Defense

DPSK Differential Phase Shift Keying

EDFA Erbium Doped Fiber Amplifier

EHS Earth Horizon Sensor

ER Extinction Ratio

FAA Federal Aviation Administration

FBG Fiber Bragg Grating

FOR Field Of Regard

FOV Field Of View

FPGA Field Programmable Gate Array

FSK Frequency Shift Keying

FSO Free-Space Optical

FWHM Full-Width Half-Maximum

GEO Geosynchronous Equatorial Orbit

GEVS General Environmental Verification Standard

GFSK Gaussian Frequency Shift Keying

GPS Global Positioning System

HPBW Half-Power Beam Width

HPLD High-Power Laser Diode

ICD Interface Control Document

IR Infrared

ISI Inter-Symbol Interference

ISS International Space Station

LED Light Emitting Diode

LEO Low Earth Orbit

LLCD Lunar Laser Communications Demonstration

LPF Low Pass Filter

LUCE Laser Utilizing Communications Equipment

MEMS Microelectromechanical System

MEO Medium Earth Orbit

MOPA Master Oscillator Power Amplifier

MPE Maximum Permitted Exposure

MSA Multi-Source Agreement

MTI Mirrorcle Technology Inc.

NDA Non-Disclosure Agreement

NEP Noise Equivalent Power

NHZ Nominal Hazard Zone

NIR Near Infrared

NODE Nanosatellite Optical Downlink Experiment

NRZ Non-Return-to-Zero

OCSD Optical Communication and Sensor Demonstration (now AeroCube-7)

OICETS Optical Inter-Orbit Communications Engineering Test Satellite

OOK On-Off Keying

OPALS Optical Payload for Lasercom Science

OSA Optical Spectrum Analyzer

PCB Printed Circuit Board

PMT Photomultiplier Tube

POD Precision Orbit Determination

PPM Pulse Position Modulation

PRBS Pseudo-Random Binary Sequence

PSK Phase Shift Keying

ROI Region Of Interest

RX Receive

RZ Return-to-Zero (Keying)

SEE Single Event Effects

SER Symbol Error Rate

SERDES Serializer-Deserializer

SLER Slot Error Rate

SNR Signal-to-Noise Ratio

TEC Thermoelectric Cooler

TIA Trans-Impedance Amplifier

TID Total Integrated Dose

TLE Two-Line Elements

TOSA Transmitter Optical Sub-Assembly (laser)

TX Transmit

UAV Unmanned Aerial Vehicle

VLSI Very Large Scale Integration

WDM Wavelength Division Multiplexing

XOR Exclusive OR

YDFA Ytterbium Doped Fiber Amplifier

Chapter 1

Introduction

Communications infrastructure is a critical component of any satellite system design. In many cases, the scientific return of a mission is directly impacted by the capabilities of the communications subsystem. These limitations are particularly evident on resource-constrained small satellites such as "CubeSats" [10]. CubeSats typically weigh less 5 kg and have a largest dimension no greater than 30 cm (e.g. "3U" form-factor).

Over the past ten years, the CubeSat community has seen tremendous growth by launching hundreds of satellites as secondary payloads. The community has its roots in academia, but now both military and commercial groups are quickly realizing the advantages of these tiny platforms. CubeSats have limited resources and capabilities compared with larger satellites, for example in power systems and propulsion, but they can provide an adequate platform for some missions (e.g., passive observations).

Remote sensing is one niche where CubeSats have proven to be especially attractive. Even though CubeSats cannot carry large or heavy sensors, they can be constructed and launched in large quantities for modest cost. As of 2015, the launch cost for a 3U to low Earth orbit (LEO) is approximately $200 k and total missions budgets (hardware development plus launch) are generally in the $500 k to $3 M range [11]). Constellations of remote sensing CubeSats can provide improved spatial and temporal sensing performance for the fraction of the cost of a traditional constellation [12].

Remote sensing missions, which tend to produce large amounts of science data, place particularly high demand on CubeSat communication solutions and are often one of the central design constraints for the mission. These constraints often stem from size, weight and power limitations that are common to satellite-based communications systems (see, e.g., [13]), but are even more restrictive for CubeSat-based designs, and consequently dictate achievable antenna gain and radio transmit power. Relevant performance metrics for these systems include the long-term average throughput (measured in bits-per-unit-time, averaged over many orbits) and the link efficiency (measured in terms of joules-per-bit, lower is desirable).

Wide transmission beamwidths waste energy. Link efficiency can be improved by directing a larger portion of the transmitted energy towards the ground station. This can be accomplished with higher transmit antenna gain, through the use of higher carrier frequencies that give higher gain for a given aperture, or both. Indeed, the

CubeSat community has slowly been migrating from VHF to UHF and, most recently, into the microwave bands.

Taken to an extreme, optical carriers can also be used for wireless communications. At optical frequencies, extremely high gains can be realized with physically small apertures. Achieving accurate pointing of the aperture becomes a significant engineering challenge in these systems. Unlike RF systems which commonly have beam footprints hundreds or thousands of kilometers in diameter, lasercom system beam diameters will often only be a few kilometers.

Laser communication (lasercom) systems have been demonstrated on a handful of missions, such as MIT Lincoln Laboratory's Lunar Laser Communications Demonstration (LLCD) which was part of NASA's Lunar Atmospheric Dust Environment Explorer (LADEE) mission to the moon. The LLCD payload is capable of providing a 622 Mbps downlink from lunar orbit using a 0.5 W transmit laser [14, 15]. As a whole, the mass and power of the LLCD system is approximately 32 kg and 137 W. To date, lasercom systems have only been demonstrated on large (> 100 kg) spacecraft.

This thesis addresses the technical challenges associated with bringing the benefits of lasercom technology to resource-constrained nanosatellites such as CubeSats. The remainder of this chapter introduces existing CubeSat capabilities, particularly the communications and attitude determination and control subsystems. Next, a survey of lasercom prior art is presented along with its applicability to CubeSat-scale lasercom. Finally, the chapter describes the organization of this thesis and the specific contributions it makes to the field.

1.1 CubeSat Capabilities

Most CubeSats today are built using drastically different design, test and verification processes than what are commonly found in larger spacecraft. Hallmarks of the traditional aerospace design process (e.g., redundancy, use of radiation hardened components, extensive thermal testing, etc.) are abandoned in favor of reducing complexity, shortening schedule and reducing cost through use of commercial components. These practices have proven viable in the relatively benign radiation and thermal environment found in most LEO orbits.

1.1.1 Power Generation

Like larger satellites, CubeSats generally make use of photovoltaic cells for power generation that are either body-mounted or mounted on deployable panels. Secondary batteries, such as lithium-ion cells, provide power through orbit eclipse and when spacecraft-to-sun orientation is not optimal for power generation. Overall power production capability is generally limited by the surface area on the spacecraft for solar cells. Many CubeSat designs now incorporate deployable panels to help address this limitation. Even with these improvements, and the use of cutting-edge solar cells, the orbit-average power generation capability of 3U CubeSats typically range from

10 W to 20 W [16, 17, 18]. Power generation limitations are often cited as one of the major limitations of CubeSats relative to larger satellites.

1.1.2 Attitude Determination and Control

CubeSat attitude determination and control systems (ADCS) have improved significantly over the last ten years. The earliest missions were flown without any form of active attitude control. On these missions, attitude determination was accomplished with coarse sun sensors or simply by interpreting the solar array currents on each of the body faces. Subsequent missions incorporated passive attitude control techniques, such as permanent magnets or gravity gradient stabilization. More recently, CubeSats have flown active attitude control systems capable of three-axis stabilization through the use of miniaturized reaction wheels and magnetorquers. A wide variety of sensors, ranging from infrared horizon sensors to lost-in-space-capable star trackers have also become available to help solve the attitude determination problem. On orbit results from these three-axis stabilized CubeSats show that $\pm 3°$ (3-σ) is achievable with current technology [4, 19, 20].

Some space-based astronomy applications have spurred the development of more sophisticated staged control systems. These systems, such as ExoplanetSat, use a piezo stage to compensate for residual pointing error from the coarse-pointing reaction wheel stage [21]. To date there, however, there have not been any on-orbit demonstrations of staged pointing control on a CubeSat platform.

1.1.3 Communications

Like larger satellites, CubeSats rely on radio frequency (RF) communication systems. These solutions tend to be robust and have low SWaP but also tend to be very restricted in terms of throughput. In fact, of the 144 CubeSat transceivers launched prior to March 2014, the vast majority carried low-rate (1200 bps) amateur radio transceivers [22]. These solutions generally operate with efficiency of approximately 1.0×10^{-3} J/bit. Higher performance RF solutions do exist for CubeSats but they are costly and often require hard-to-obtain ground infrastructure (e.g., a large diameter tracking dish).

The Micro-sized Microwave Atmospheric Satellite (MicroMAS), developed jointly by the MIT Space Systems Lab and MIT Lincoln Laboratory and launched in 2014, is an example of a CubeSat mission that carries a high-performance radio modem. MicroMAS incorporates a commercial radio modem from L3 Communications West that provides a 1.5 Mbps user data rate, a full three orders of magnitude faster than most CubeSat solutions. Unfortunately, the system demands a very large ground antenna (18 m parabolic dish) in order to provide sufficient link margin. A difficult regulatory process also accompanied the engineering challenges associated with using this solution. The overall link efficiency of the MicroMAS downlink signal is approximately 6.67×10^{-6} J/bit.

Despite the high link rate of the MicroMAS radio modem, when the satellite-to-ground access times are factored in, the average continuous throughput of the

communications subsystem is a modest 26.6 kbps.[1] For MicroMAS, this is barely sufficient to support its science mission; other remote sensing missions, particularly those with imagers, have throughput demands far exceeding this capability.

CubeSat communications solutions are fundamentally limited by the size of the antenna/aperture than can be accommodated on the satellite. One work-around for this limitation is the design and incorporation of deployable antenna structures. Another solutions is to migrate to a higher carrier frequency which allows higher gain to be achieved from a given size antenna. Higher frequencies also generally allow for a wider channel bandwidth. A handful of CubeSat research groups are in the progress of developing CubeSat radio systems for use in the microwave bands (mainly S-band and X-band) [23, 24, 25]. Initial results have been promising, but missions using these solutions still suffer from significant regulatory hurdles and still require costly ground infrastructure.

1.2 Existing Satellite Optical Communication Systems

1.2.1 Large Satellite Demonstrations

Several satellites have demonstrated lasercom techniques in the near-earth regime (i.e. LEO and geosynchronous orbit, GEO) over the past 20 years [26, 27, 5, 13]. There has been great interest, particularly within the defense community, in using narrow optical beams to establish robust satellite crosslinks that are difficult to intercept and jam. In this section, notable near-earth lasercom missions will be reviewed as they are most relevant to CubeSat missions which typically ride-share to LEO. We start with GEO satellites and then move on to LEO satellites which have markedly different pointing requirements.

GEO Satellites

LCE (1994) The Laser Communication Experiment (LCE), developed by the Communications Research Laboratory in Japan flew on the ETS-VI satellite in 1994. This mission was the first purpose-built lasercom satellite for demonstrating space-to-ground laser communications. The satellite failed to reach its intended geostationary orbit, however, the optical communications demonstration was still carried out from a high elliptical orbit [7]. LCE weighed 22.4 kg, consumed around 90 W of electrical power and was capable of bidirectional communications at 1.024 Mbps. Additional design specifications are provided in Table 1.1.

Despite the difficulties that arose from the off-nominal orbit, most of the LCE mission goals were accomplished. In addition to building space heritage for the myriad of mechanical and opto-electronic components in the lasercom system, valuable data concerning the properties of the space-to-ground optical channel were collected

---

[1]This estimate incorporates the variety of assumptions about orbital geometry, link parameters and pass utilization efficiency, and a single ground station.

Optical Transmitter

Telescope	7.5 cm
Wavelength	0.83 µm
Source	Laser Diode (AlGaAs)
Power	13.8 mW (average)
Beam Divergence	30 µrad or 60 µrad
Point-ahead mechanism	two-axis piezo
Data Rate	1.024 Mbps
Modulation	OOK, manchester encoded

Optical Receiver

Telescope	7.5 cm
Wavelength	0.83 µm
Detector	Si-APD
Data Rate	1.024 Mbps

Coarse Tracking System

Detector	CCD
Acquisition range	26.2 mrad (half cone angle)
Field of view	8 mrad
Actuator	Two-axis gimballed mirror

Fine Tracking System

Detector	Si photodiode quadcell
Field of view	0.4 mrad

Table 1.1: High-level design parameters for LCE (adapted from [7])

during the mission. The closed-loop tracking system which relied on an uplink beacon laser was also proven out although worse-than-expected uplink channel impairments impaired the fine-tracking mechanism. Finally, the mission provided some of the first bidirectional optical propagation measurements.

ARTEMIS (2001) This European-led mission demonstrated bidirectional lasercom between a GEO orbit and the European Space Agency Optical Ground Station (OGS) in Spain [28]. This mission improved upon LCE but incorporated narrower beam divergences (and the requisite pointing mechanism) which allowed higher data rates. A summary of the ARTEMIS specifications is provided in Table 1.2.

The main contributions made by the ARTEMIS program were a better understanding of atmospheric impairments, particularly at low zenith angles. The stationary position afforded by a GEO mission allows for repetitive measurement of link parameters over many days. Data from this mission was instrumental in improving propagation models and for guiding the design of follow-on lasercom missions.

	Space Terminal	Ground Terminal
Aperture	25 cm	101 cm
Transmitter		
Optical source	GaAlAs LD, single-mode	Ar laser pumped Ti:Sapphire laser
Power out	10 mW (avg)	300 mW (max)
Wavelength	819 nm (nominal)	847 nm
Modulation	2-PPM, 2.048 Mbps (fixed)	NRZ, 49.4 Mbps (fixed)
Beam divergence	8.5 μrad	
Receiver		
Detector	Si-APD	Si-APD
Field of view	70 μrad	87.3 μrad

Table 1.2: High-level design parameters for ARTEMIS (adapted from [8])

GeoLITE (2001) Developed at MIT Lincoln Laboratory, this mission carried an experimental lasercom communication payload to a GEO orbit. Unfortunately, nearly all of the details of the mission are classified but sponsoring agencies have heralded the mission as a success [29]. It is included here for completeness.

LEO Satellites

The process of establishing ground-to-LEO lasercom links faces far different challenges than the ground-to-GEO configuration. Free-space path losses are greatly reduced thanks to the shorter link range, however, the fast apparent velocity of the satellite makes link setup and acquisition much more demanding. Highly precise pointing mechanisms must also be able to support high slew rates while maintaining accuracy. Additionally, the link must traverse different atmospheric cross-sections (e.g. low-elevation vs. high-elevation) which can lead to large fluctuations in signal quality.

RME (1994) Although not strictly a communications satellite, the Relay Mirror Experiment (RME) satellite, developed by Ball Aerospace, was one of the first LEO satellites to complete bidirectional measurement of scintillation and attenuation [30]. This satellite was also able to act as a crude (i.e. passive) communication satellite using its relay mirror.

Acquisition and closed-loop tracking of the satellite was achieved through the use of a downlink beacon laser. Once acquired, uplink lasers with beam divergences of 30 μrad to 90 μrad were used to illuminate the satellite. The uplink signal was measured by RME and could be used to measure fine pointing errors in addition to irradiance of the uplink signal.

The primary contribution of RME was a better understanding of the temporal spectrum of the scintillation. This data has been used to dimension the interleaving systems that are used on modern lasercom systems.

STRV-2 (2000)   The Space Technology Research Vehicle 2 (STRV-2) which was built with funding from the US Ballistic Missile Defense Organization carried a lasercom terminal along with a handful of other experiments. The lasercom payload, which was designed by the AstroTerra Corporation, had the ambitious goal of closing 1 Gbps LEO-to-ground links. The entire payload, including the two-axis gimbal, weighed < 15 kg and consumed 100 W when operating [31].
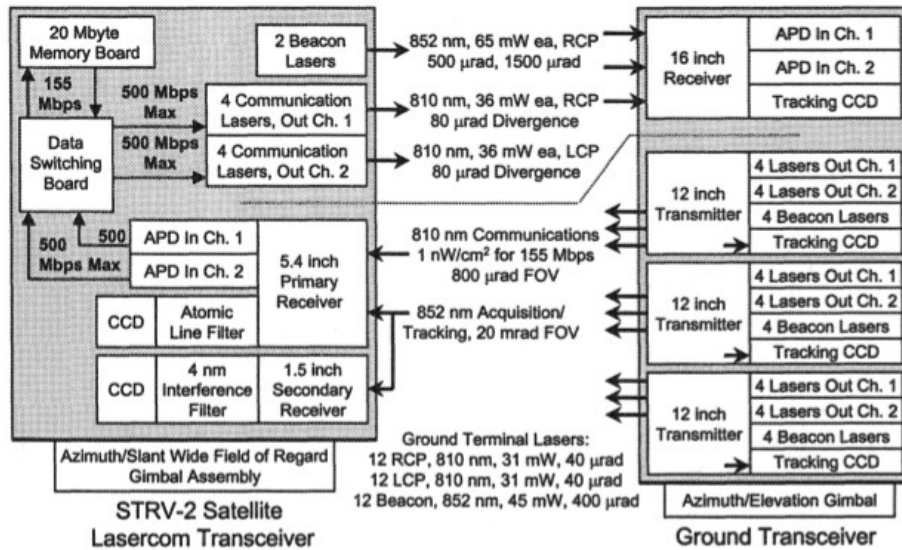
Figure 1-1: Block diagram of the STRV-2 lasercom payload [1]

Unfortunately, this mission was never able to achieve communications due to problems with the acquisition sequence. Beacon beam divergences and tracking receiver field of regard were sized based on expected performance of the host spacecraft attitude control system and ephemeris data. After many attempts, it was discovered that both attitude control performance and ephemeris knowledge were significantly below expectations. Funding for the demonstration was cut before workarounds could be found [1].

In [1], numerous recommendations are made to future designers of LEO lasercom systems. Most of these revolve around adding flexibility to the acquisition process, especially the beam divergences, in order to deal with unexpected issues on-orbit. Another recommendation is to allow real-time control of the lasercom payload using an RF-link. We incorporate this recommendation into the CubeSat lasercom terminal design as described in Section 2.2.1.

OICETS/LUCE (2005)   The Laser Utilizing Communications Equipment (LUCE) payload was carried aboard the Japanese Optical Inter-orbit Communication Engineering Test Satellite (OICETS) in 2005. The primary objective of LUCE was to demonstrate inter-orbit communications between OICETS (LEO orbit) and ARTEMIS (GEO orbit, discussed above). A secondary objective of LUCE was to demonstrate LEO-to-ground communication using the optical ground stations in Japan and Europe [32].

LUCE Payload Specifications

Mass	140 kg
Power	220 W (during comm.)

Optical Transmitter

Telescope	26 cm cassegrain-type
Wavelength	848 nm or 847 nm (LD)
Power	100 mW (average)
Beam Divergence	5.5 µrad
Data Rate	49.3724 Mbps
Modulation	OOK, NRZ

Tracking System

Coarse mechanism	Two-axis gimbal
Coarse sensor (accuracy)	CCD ($\pm 0.01°$)
Fine mechanism	Two piezo-actuated mirrors
Fine feedback (accuracy)	quadcell (± 0.92 µrad)
Point-ahead mechanism	Additional two-axis piezo mirror

Ground Receiver (KIODO Experiment)

Receive Telescope	40 cm transportable
Beacon Telescope	Two 5 cm
Acquisition	open-loop
Tracking	closed-loop w/tracking camera (± 100 µrad)

Table 1.3: High-level design parameters for LUCE (adapted from [9])

Experiments between LUCE and a ESA ground station in Germany demonstrated operation between a LEO satellite and a small (40 cm) transportable telescope like the one proposed for the CubeSat ground terminal (Section 2.2.2). The 50 Mbps link achieved uncoded bit error rates of 2×10^{-6} under nighttime clear-sky conditions. Like most lasercom missions, this experiment used an uplink beacon for initial acquisition followed by closed-loop tracking on both ends of the link [33].

OPALS The Optical Payload for Lasercom Science (OPALS) is an experimental lasercom terminal that was developed by the NASA Jet Propulsion Laboratory for use on the International Space Station. Despite its large SWaP (50 kg, 84 cm × 86 cm × 117 cm,100 W), the OPALS design shares many similarities to the CubeSat-scale lasercom system design presented in this thesis. OPALS is a downlink-only system that provides 50 Mbps link rates from LEO to meter-class ground terminals. The pointing, acquisition and tracking system on OPALS relies on an uplink beacon at 976 nm to improve pointing knowledge. OPALS also uses a bistatic design on the space segment, which features co-mounted but independent optical trains

attached to a single gimbal.

1.2.2 Small Satellite Demonstrations

RISESAT   A Japanese team is currently designing RISESAT which has an optical downlink capability in addition to a number of other experiments [2]. This mission is much larger than a CubeSat at 50 cm × 50 cm × 50 cm and 50 kg, however, the optical subsystem is a small fraction of the satellite.

The optical payload, called the "Very Small Optical TrAnsmitter for component validation" (VSOTA), is a transmit-only design that can operate at both 980 nm and 1550 nm. The transmitters are able to produce 540 mW and 80 mW with beamwidths of 0.2° and 0.07°, respectively. Physically, the VSOTA is split into two fiber-coupled modules, one (VSOTA-E) carries the electronics and diode control circuitry while the other (VSOTA-COL) carries the apertures and final laser amplifiers (Figure 1-2). As a whole the VSOTA has a mass of < 1 kg and consumes < 10 W while providing link rates up to 100 kbps.
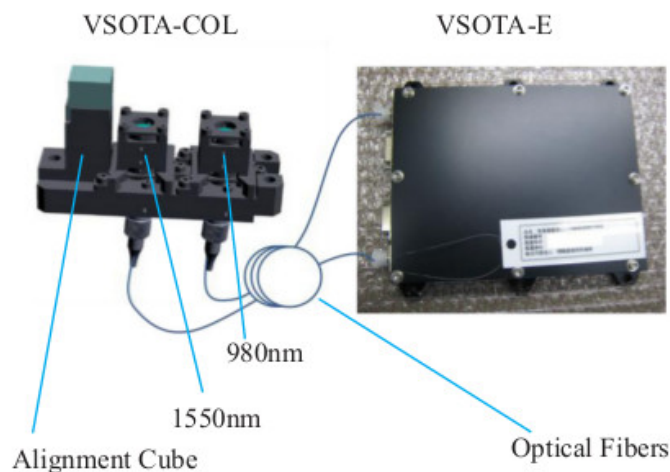
Figure 1-2: The VSOTA payload for RISESAT [2]

RISESAT's optical transmitter lacks steering capability and relies on precise pointing of the entire spacecraft. The predicted attitude control accuracy for RISESAT is 0.1° which should be sufficient for the wider (0.2°) beam at 980 nm. During nominal operations, this is expected to be completed in an open-loop fashion. An experimental goal of the mission is to measure the pointing error on the satellite bus. This measurement will be accomplished by imaging an uplink beacon signal, and through simultaneous measurement of downlink irradiance at spatial distributed ground receivers (spaced at roughly 1 km). Even though an uplink laser signal present, it will not be used by the satellite for closed-loop tracking.

A variety of ground stations ranging from a 1.5 m telescope down to a modest 20 cm are slated for use with RISESAT. All of these ground stations leverage commodity detectors such as photodiodes (PDs) or avalanche photodiodes (APDs).

Overall the performance specifications for RISESAT's lasercom capability are relatively modest since the design relies solely on body-pointing and since the transmit laser power is small. One interesting aspect of RISESAT is the use of the corner-cube reflector (CCR) for precision orbit determination (POD) using time-of-flight laser ranging.

1.3 CubeSat Optical Communications

This section introduces existing efforts to bring optical communications techniques to CubeSats. It also addresses the concept of operations for CubeSat optical communications with an emphasis on differences from optical communications on larger satellites. This section closes with high-level CubeSat lasercom feasibility results that are based upon radiometric link analyses.

1.3.1 CubeSat Optical Communication Demonstrations

FITSAT-1

FITSAT-1, developed at the Fukuoka Institute of Technology, was a pioneering satellite for CubeSat-scale free-space optical communications. Launched in 2012, this 1U ($10\,\text{cm} \times 10\,\text{cm} \times 10\,\text{cm}$) mission carried two arrays of high-power light-emitting diodes (LED) along with an experimental RF transceiver [25]. The mission was able to use a passive attitude control system (permanent magnets) since the optical transmitter was highly diffuse.

FITSAT-1 was capable of transmitting at two visible wavelengths: $526\,\text{nm}$ and $625\,\text{nm}$. The transmitters were both made of arrays of dozens of LEDs that were installed on the face of the satellite using available space around the satellite's solar cells. By maintaining a low transmit duty cycle, this small CubeSat was able to achieve an impressive $200\,\text{W}$ peak optical transmit power.

Although visible to the naked eye on the ground, the main attempts at using the system for digital data transfer were conducted using a $25\,\text{cm}$ telescope and photomultiplier tube (PMT). This system, which was pointed open-loop, was able to recover the $5\,\text{kHz}$ modulation imparted on the signal [3]. Both a $10\,\text{nm}$ optical bandpass filter and an electrical bandpass filter were used to improve signal-to-noise ratio.

Although FITSAT-1 represented an important first-step in CubeSat-scale lasercom, the design had notable limitations. First, the wide beamwidth ($120°$ half-power beamwidth) largely negates the main benefit of lasercom: high-gain apertures. Second, LEDs such as those used on FITSAT-1, are not nearly as monochromatic as laser-based sources. Optical energy from LEDs is typically spread over $> 10\,\text{nm}$ of spectrum. This limits spectral filtering that is feasible at the receiver which leads due SNR degradation due to background light (e.g. from stars).

Figure 1-3: Photograph of FITSAT-1 showing a patch antenna (brown) surrounded by LEDs [3]

AeroCube-OCSD

The Aerospace Corporation's Optical Communication and Sensor Demonstration (AeroCube-OCSD) is currently in development and slated for launch in August 2015 (Figure 1-4). The AeroCube-OCSD mission consists of two identical 1.5U CubeSats ($15\,\text{cm} \times 10\,\text{cm} \times 10\,\text{cm}$). The primary goal of this mission is to demonstrate feasibility of an lasercom downlink from a CubeSat. The communication goal is to close a 5 Mbps (200 Mbps stretch goal) link over a 900 km range [34].

To accomplish this mission, AeroCube-OCSD carries a complex attitude determination and control system (ADCS). Attitude sensors include redundant three-axis magnetometers, Earth horizon sensors, sun sensors and star trackers. Actuators include three torque rods and three reaction wheels. The performance of this system, in terms of absolute pointing accuracy, is predicted to be between 0.1° and 1.0° depending on which sensors are being used. AeroCube-OCSD also carries a GPS receiver for precision orbit determination. The GPS is a key component of the lasercom link as it is used to calculate attitude for initial (blind pointing) link acquisition.

An uplink optical beacon can also be used for closed-loop pointing control. This signal is detected by a quadcell receiver that is fed by a 2.5 cm aperture. Error signals from the quadcell are sent to the ADCS for attitude correction. Interestingly, the performance of this control mode (0.1°) is predicted to be no better than open-loop pointing using the the star trackers.

AeroCube-OCSD's optical transmitter consists of a 10 W optical transmitter with

28
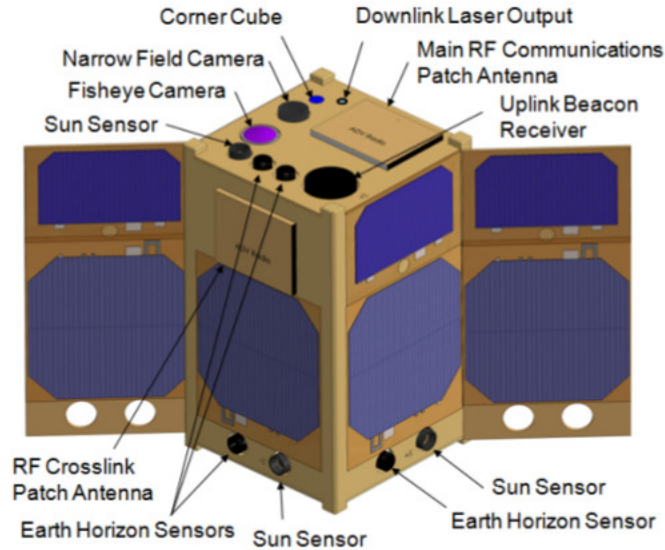
Figure 1-4: Rendering of AeroCube-OCSD [4]

on-off-keyed (OOK) modulation at 1064 nm. Their design uses a low-power modulated laser that drives a two-stage ytterbium-doped fiber amplifier (YDFA). The transmitter design is implemented in a compact $9\,\text{cm} \times 9\,\text{cm} \times 2.5\,\text{cm}$ volume. An early prototype unit was reported to achieve an output power of 14.7 W, a modulation bandwidth of 500 MHz and a "wall-plug" efficiency of approximately 25%. This is a fully custom fiber amplifier designed and built at Aerospace Corporation, to the best of our knowledge COTS solutions do not exist at these optical power levels in such a compact package. Note that this transmitter demands almost 60 W of electrical power when operating - this is well above the capabilities of most CubeSat power systems today, even for short durations (e.g., a 7 min ground station access). The downlink half-power beamwidth is fixed at 0.35 °FWHM. Depending on the data rate achieved on orbit, the link efficiency is expected to be between $1.2 \times 10^{-5}\,\text{J/bit}$ (5 Mbps) and $3.0 \times 10^{-7}\,\text{J/bit}$ (200 Mbps).

The optical ground station for AeroCube-OCSD, the Mobile Communications Atmospheric Measurements (MOCAM) station, is located at Mt. Wilson, CA. The station uses a 30 cm telescope on a high-precision mount along with a conventional avalanche photodiode (APD) for receiving the downlink signal. The expected sensitivity of the receiver is 200 photons/bit.The uplink signal (10 W) is provided by a separate 20 cm aperture on the same mount.

The concept of operations that has been described for AeroCube-OCSD illustrates the complexity of the pointing, acquisition and tracking requirements of lasercom. In the orbits leading up to the lasercom downlink attempt, the onboard GPS is used to capture precise position information. During a ground station pass, this GPS data is downlinked and analyzed on the ground to generate high-precision orbit ephemerides and a time-stamped "pointing table." The pointing table is uplinked to AeroCube-OCSD one orbit prior to the lasercom attempt so that ADCS has time to prepare

for the slew maneuver. This approach is very similar to what was employed on the STRV-2 mission. If link acquisition is unsuccessful, the satellite can perform a scan maneuver about the nominal attitude to search for the ground station.

The most notable limitation of the AeroCube-OCSD design stems from the fact that the space optics are rigidly mounted to the spacecraft body. This directly impacts concept of operations for the lasercom link and levies difficult requirements for both ADCS capabilities and precision orbit determination. For AeroCube-OCSD, this is acceptable as the mission carries a sophisticated ADCS with known performance based on prior missions. Additionally, link efficiency is degraded since the system must use a relatively wide downlink beamwidth which is commensurate with the predicted pointing capability. To achieve the desired data rates, the design compensates for the wide downlink beam by using a high transmit power that puts extreme demands on the CubeSat's power and thermal subsystems.

A CubeSat-scale lasercom design would carry much greater utility for the CubeSat community if it could be used on satellites with modest ADCS and power system capabilities.

1.3.2 Implementation Gaps

The extreme power constraints facing CubeSats and their growing use in data-intensive remote sensing applications have created a demand for more power-efficient communication solutions. Optical communication techniques are a promising solution, however, lasercom systems designs today do not lend themselves to the extreme size, weight and power restrictions found in CubeSats. Additionally, existing lasercom solutions do not follow the low-cost COTS-based implementation techniques common to most CubeSat efforts. What is needed is a lasercom system that is applicable to the "typical" CubeSat by adhering to the application SWaP limitations while being realizable with low-cost components.

After a review of prior lasercom efforts and the current state of the art in CubeSat optical communications, we identified two significant implementation gaps that must be filled to realize this goal. First, although CubeSat pointing control systems are improving, it is still necessary to use broad beams and high optical transmit power levels (e.g., AeroCube-OCSD). Ideally, a drop-in lasercom payload should be able to operate while only levying modest (e.g., $\pm 1°$, 3-σ) pointing requirements on the host CubeSat. One way to accomplish this is through the use of a fine-steering mechanism that improves upon the host's pointing capability which enables narrower, more power-efficient, transmit beams. In this thesis, we design a lasercom terminal architecture that incorporates a suitable fine-steering solution that fills this gap.

Second, laser transmitters that are both compact and built from low-cost COTS components are not available today. All lasercom missions to date have employed aerospace-rated or, at a minimum, heavily-customized and qualified commercial grade laser transmitters (e.g., OPALS). These solutions are simply too expensive for CubeSat applications where the entire hardware budget for the CubeSat is often under $500k. An ideal laser transmitter solution would leverage the low-cost COTS optical components (e.g., fiber amplifier modules) that have grown out of the fiber telecom-

munications industry. This laser transmitter should be able to support data rates achievable with current pointing solutions (i.e., 1 Mbps to 10 Mbps) but should also be able to scale to support higher data rates as pointing capabilities improve. We design, prototype and validate a fully COTS-based laser transmitter solution that is both compatible with CubeSat SWaP constraints and that provides ample modulation rate "headroom" to track future improvements in pointing capability.

1.3.3 Concept of Operations

Remote sensing missions typically have asymmetric communication requirements as the bulk of the data transfer occurs in the downlink direction. Bidirectional communications is essential for command and control of the satellite, however, a low-rate uplink is usually sufficient to meet these needs.
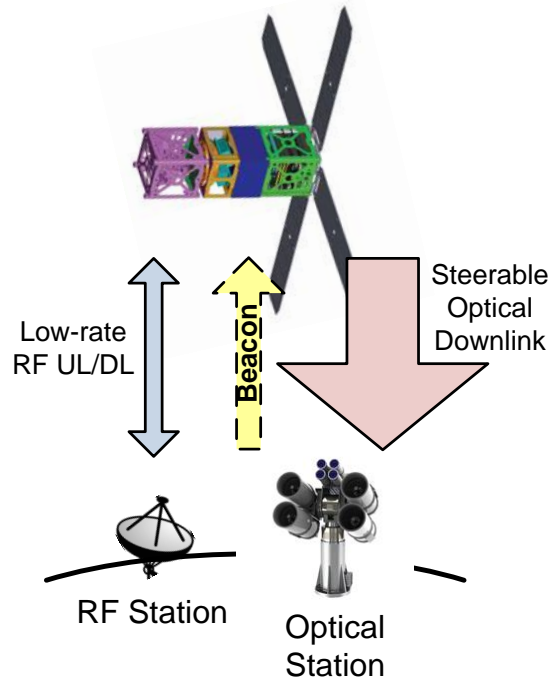
Figure 1-5: Hybrid RF and lasercom architecture consisting of a narrowband bidirectional RF link and broadband laser downlink.

In this thesis, a hybrid RF and optical communication configuration is proposed (Figure 1-5) that can meet both needs. This configuration provides a reliable low-rate RF link that will be used for command and control as well as a high-rate optical downlink that will facilitate the scientific mission. The RF link is also used for critical coordination steps that are needed to point, acquire, and track the high-rate optical link. Since the data throughput demands of the RF link are minimal, it can be a narrowband modulation (e.g., 9600 baud GFSK) that is simpler to get through the regulatory process. Alternatively, low-rate commercial satellite communication systems such as GlobalStar could be used.

Unlike larger spacecraft that must maintain specific attitudes (i.e., "station keeping") to meet mission and spacecraft health requirements (e.g., power generation and thermal control), CubeSats often perform significant attitude change maneuvers to achieve mission goals. Lasercom systems installed on larger spacecraft almost always incorporate a two-axis gimbal that is used to coarsely point the communication beam. For CubeSat applications, it is very challenging to incorporate conventional gimbal solutions within the limited size, weight and power (SWaP) resources. We propose a solution that eliminates a gimbal system in favor of body-pointing the CubeSat to track the receive terminal[2]. A radiometric analysis was used to determine if current CubeSat ADCS capabilities are sufficient to support optical communication links that are competitive with existing RF solutions.

1.3.4 Radiometric Feasibility

This section explores the feasibility of CubeSat optical communications from a radiometry standpoint. A much more detailed link analysis is presented in Chapter 2. We conduct a radiometric-based link analysis for two hypothetical CubeSat configurations: a 1U CubeSat with passive ADCS, and a 3U CubeSat with active ADCS (i.e., three-axis stabilization). The optical beamwidth is sized as dictated by the pointing capabilities of each platform. The results show that CubeSat ADCS capabilities, as they exist today, are insufficient for making lasercom an attractive alternative to RF solutions.

For each configuration, we have selected optical transmitter technologies which are suitable from a power consumption standpoint. In both cases, we assume that the receiver's performance is 1000 photons per bit, which is considered to be a conservative and easy-to-obtain performance level using COTS detector technology such as APDs [35, 36]. Aside from the receiver sensitivity, no attempt is made to match parameters between the two systems - we simply use components which are known to be readily available.

Scenario 1: 1U CubeSat with Passive ADCS

In this scenario we consider a 1U CubeSat with passive ADCS, that is patterned after the FITSAT-1 mission (Section 1.3.1). Because of the very limited pointing capabilities, the optical transmitter needs to have a broad beamwidth (e.g., 120° FWHM) to ensure that the ground station lies within the transmit beam. Since this beam has very low gain (approximately 6 dBi), the system must be capable of generating relatively high output powers. As has been stated above, available power is one of the biggest shortcomings of CubeSats. Thus, it is desirable to use a transmitter technology that offers extremely high electrical-to-optical (EO) efficiency.

High power LEDs, which have primarily been developed for lighting applications, perform well in this regard with EO efficiency exceeding 50% being commercially

---

[2]We note that solution imparts two requirements on the host: fast slew for ground station tracking ($\sim 1\,°\,s^{-1}$) and an acceptance of the need to periodically deviate from mission-defined attitude for communications downlink.

available. This class of LEDs is available with integrated optics that are capable to producing a wide range of beam patterns, including the 120° FWHM beam proposed above. Because of the limited directionality of the transmit optical signal, this system achieves a link efficiency of 1.76×10^{-1} J/bit.

Scenario 2: 3U CubeSat with Active ADCS

This scenario considers a 3U CubeSat with active ADCS that is functionally similar to the AeroCube-OCSD mission (Section 1.3.1). This design uses body-pointing alone to point the transmit beam towards the ground station. Although 3-axis stabilized CubeSats are still in early development, several missions have already demonstrated pointing accuracy of 3° (3-σ) or better [4, 19, 20]. Given this baseline pointing capability, we will assume a 6° FWHM downlink beam for this hypothetical system. This implies a pointing loss of no more than 3 dB (3-σ) .

Given the narrower beamwidth, this system to requires less optical transmit power than the LED-based system in Scenario 1. For that reason, we assume that the system will used a directly-modulated laser diode. These are readily available from commercial sources at the 1 W power level, and have EO efficiency exceeding 20%. Laser diode sources have the added advantage of narrow spectral width which allows for aggressive bandpass filtering at the ground station. This configuration achieves a link efficiency of approximately 3.08×10^{-4} J/bit.

Radiometry Conclusions

Table 1.4 contains the radiometric link budgets for each of the hypothetical scenarios. The LED-based solution for the 1U passively stabilized CubeSat is predicted to provide only about 100 bps of throughput despite consuming 20 W during transmit. This solution is certainly not competitive with the existing RF solutions available to CubeSat developers, though it could be operated without regulatory overhead (i.e., there is no licensing process for optical carriers). The laser-based solution with its narrower beam divergence can provide nearly 100 kbps, but still cannot compete with RF solutions in terms of joules-per-bit (e.g., MicroMAS L3 modem at 6.67×10^{-6} J/bit vs the hypothetical laser system at 3.08×10^{-4} J/bit).

The second point that this comparison illustrates is the squared relationship between beam divergence and link efficiency. A 10x reduction in divergence is met with a 100x increase in efficiency/throughput. Scenario 2, the 3U CubeSat with three-axis stabilization, is patterned after current CubeSat ADCS capabilities. The radiometry results show that CubeSat ADCS capabilities as they stand today are insufficient for lasercom, unless we are willing to expend a great deal more electrical power in the transmitter (e.g., like AeroCube-OCSD).

1.4   Contributions & Approach

Recent on-orbit results, such as those from LLCD, have clearly demonstrated lasercom's ability to provide more power-efficient communication links. However, there are

Table 1.4: Comparative radiometric link budgets for a 1U CubeSat with an broad beam LED transmitter (Scenario 1) and a three-axis stabilized 3U CubeSat with a narrow beam laser transmitter (Scenario 2).

	Scenario 1	Scenario 2	Units	Notes
ADCS	Passive	3-axis		
Transmitter	LED	Laser diode		
Electrical input power	20	20	W	
Wavelength	635	975	nm	
Electro-optical efficiency	0.5	0.3		
Modulation duty cycle	0.5	0.5		
Optical power	6.98	4.77	dBW	
Half-power beamwidth	120	3	deg.	
Solid angle of beam	3.14	0.002	Sr	Conical beam
Transmit antenna gain	6.02	37.7	dBi	
Channel				
Path length	1000	1000	km	20° elevation
Path loss	-265.9	-265.9	dB	Free-space
Pointing loss	-3	-3	dB	
Atmospheric loss	-2	-2	dB	
Receiver				
Aperture diameter	30	30	cm	COTS telescope
Receive antenna gain	123.4	119.7	dB	Diffraction limit
Power at detector	-134.5	-108.8	dBW	
Photons per second	113721	64841208	γ/sec	
Required photons/bit	1000	1000	γ/bit	
Predicted data rate	**114**	**64841**	**bps**	
Link efficiency	**1.76e-1**	**3.08e-4**	**J/bit**	Excludes ADCS*

* Link efficiency calculation only considers lasercom terminal power input, excludes power consumed by host ADCS.

numerous "implementation gaps" which are preventing these techniques from being utilized in resource-constrained CubeSats. This thesis addresses these gaps through the following contributions:

1. Design of a novel lasercom system architecture capable of providing high rate (10 Mbps to 100 Mbps) downlink at LEO under *severe* size, weight and power constraints using a staged control approach to improve pointing and thus link power efficiency (joules per bit).

2. Definition of an optical fine-steering control stage using a fine-steering mechanisms needed to improve pointing capability, and experimental validation of the performance and feasibility of these solutions.

3. Design, implementation and validation of a *compact*, rate-scalable laser transmitter that uses a COTS-based approach compatible with typical CubeSat development cost and risk profiles.

4. Development of "built-in self-test" capabilities for the laser transmitter that enable incremental calibration and testing of the design on orbit thereby improving the likelihood of mission success.

The content of this thesis is organized as follows. Chapter 2 presents the analyses conducted in the development of the top-level system architecture for the lasercom system including both the space terminal and ground terminal design. Technological gaps associated with implementing this system are identified with solutions including a compact high-rate laser transmitter design and a fine steering mechanism. Chapter 3 presents the design process which addresses those implementation gaps. Chapter 4 describes the experimentation validation work that shows that the designs meet system requirements. Chapter 5 concludes the thesis by identifying remaining technical challenges associated with implementing and flying the proposed system.

Chapter 2

System Architecture

In this chapter, we present trade studies and analyses that lead to the definition of a lasercom system architecture that is appropriate for CubeSats. The chapter starts by enumerating high level design motivations and assumed constraints. Next, we describe the top-level system design and analysis supporting major design decisions, such as beamwidth and the use of beacon signals. Subsequently, detailed link budget analyses are presented which establish the feasibility of both the downlink and uplink (beacon) signals. The chapter closes with top-level design constraints and performance goals as well as identification of technology gaps that exist in implementing the design.

2.1 Design Drivers & Constraints

CubeSats come in a variety of sizes but the 3U ($30\,\text{cm} \times 10\,\text{cm} \times 10\,\text{cm}$) and 6U ($30\,\text{cm} \times 20\,\text{cm} \times 10\,\text{cm}$) form-factors have become popular choices for majority of missions today. Based on actual and projected launch statistics, this is a "Goldilocks zone" where size, weight and power resources are reasonable while launch costs are relatively low [37, 38]. In this section, we motivate the design constraints assumed for developing a laser communication system architecture that is both compatible with 3U CubeSat size, weight and power (SWaP) as well as competitive with the incumbent RF-based solutions.

Figure 2-1 gives a high-level perspective of how requirements were derived for the project. Initial targets for the lasercom payload size, weight and power have been chosen so that they "fit" within the capabilities of a 3U CubeSat, while still leaving useful SWaP for other payloads. Link performance metrics, such as acquisition time and user data rate, were dictated by the performance of existing RF solutions. Finally, the state of CubeSat ADCS capabilities were used to set a baseline for the coarse pointing performance of the host CubeSat.

2.1.1 Size, Weight and Power Constraints

We strive to implement a high-rate downlink lasercom terminal design that would be of utility for a "typical" 3U CubeSat by meeting and exceeding the capabilities
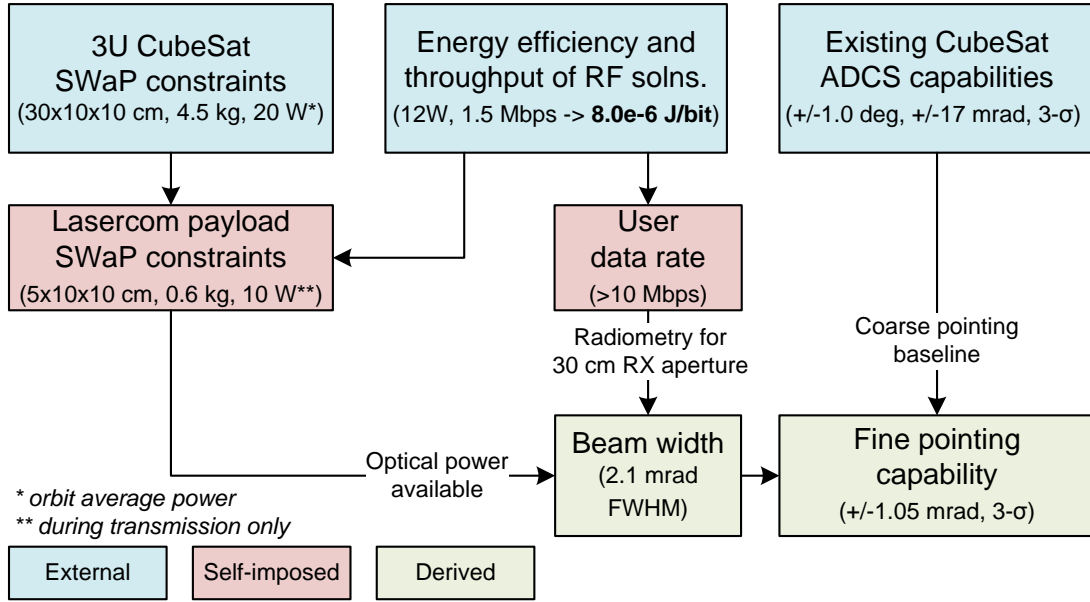
Figure 2-1: Requirements "flow-down" for the CubeSat lasercom system showing external (blue), self-imposed (red) and derived (green) requirements. Current best estimates for the various constraints are included.

provided by existing radio frequency (RF) solutions. An acceptable solution would have a SWaP footprint comparable to that of existing high-rate RF solutions. As an initial starting point for analysis, we have allocated $5\,\text{cm} \times 10\,\text{cm} \times 10\,\text{cm}$, $500\,\text{g}$, and $10\,\text{W}$ (during downlink). The $10\,\text{W}$ power allocation is comparable to existing high-rate radio solutions (e.g., the L3 Communications Cadet). The volume and mass allocations for our system include the transmit and receive apertures (i.e., the "antennas"), which make them roughly comparable to RF solutions consisting of a radio modem module and a deployable antenna.

2.1.2 Intended Orbit

Typically, CubeSats are launched as a part of "ride share" programs to various low Earth orbits (LEO). CubeSats have been deployed in a wide variety of orbits with altitudes ranging from $250\,\text{km}$ to $1000\,\text{km}$ and with inclinations from equatorial to sun-synchronous [37]. The ISS orbit (roughly $400\,\text{km}$ at $51.6°$ inclination) is a very common orbit for CubeSats due to the high frequency of resupply and crew transfer launches.

Spacecraft orbit dictates communication link ranges as well as the duration of ground station encounters. For design purposes, we assume a nominal $400\,\text{km}$ orbit at an inclination compatible with the ground station's latitude. We assume a maximum link range of $1000\,\text{km}$ which corresponds to a $20°$ elevation for a $400\,\text{km}$ object viewed from the ground station. As compared to RF systems, lasercom systems typically will not operate below $20°$ elevation angles due to increasingly severe atmospheric impairments [39].

2.1.3 Environmental Constraints

This section describes various environmental constraints that generally impact Cube-Sat development.

Thermal Design

CubeSat thermal design practices vary widely from mission to mission. Some teams employ detailed finite-element thermal models that are cross-checked and calibrated with costly thermal vacuum trials. Indeed, these practices mirror those used in traditional aerospace design flows (e.g., [40]). In contrast, other CubeSat operators will perform minimal analysis and instead just apply engineering best practices (such as PCB component dissipation analysis) [41].

Another important factor in CubeSat thermal design is the LEO operating environment. As compared to MEO, GEO or deep space, satellites in LEO always have hemispherical exposure to the Earth, its albedo, and its infrared emissions [42]. In a sense, the spacecraft and the Earth are thermally coupled to each other. This helps to limit thermal excursions.

Common CubeSat construction techniques also help to moderate thermal swings: PCB-mounted solar cells usually cover much of the CubeSat's surface. The glass composite construction of these PCBs is an effective insulator that helps the vehicle retain heat. Other sensitive components, notably battery assemblies, will often carry integrated heaters to keep them within operating range.

For this study, we have assumed an operating temperature range of $0\,°C$ to $40\,°C$ for the lasercom terminal components. This is a common design guideline used within the CubeSat community [42, 16].

Radiation Effects

Understanding the radiation environment and any effects it may have on spacecraft operations, particularly the electronics, is central to the traditional aerospace design process. Radiation requirements levied upon a mission are highly dependent on the intended orbit and the reliability requirements of the design. As mentioned previously, most CubeSats occupy LEO orbits where the radiation environment tends to be less severe [43, Table 6]. Certain LEO orbits, such as the sun-synchronous orbits that are popular for imaging missions, experience slightly higher radiation doses due to solar protons present in the polar regions due to the magnetic field irregularities and particle precipitation.

Modeling tools, such as SPENVIS [44], are used to predict expected radiation dose for a mission based on orbital parameters, shielding, and solar activity (e.g., CREME96 [45]). As an example, a mission was analyzed with SPENVIS assuming a $500\,km$, $42°$ inclination orbit and $50\,mil$ Al average shielding yielded an expected dose of $1.2\,krad(Si)$ per year [46]. Subsequent total integrated dose (TID) testing of vital COTS components within the spacecraft avionics design indicated that they can readily survive TID levels in excess of $10\,krad(Si)$. Other TID test campaigns have yielded similar results [47, 48].

Single event effects (SEE), such as "bit flips" and latch up, are less studied within the CubeSat community. This is likely a result of the costly test requirements (i.e., time on particle accelerators) and a lack of access to vendor-proprietary device details that are needed to design test plans. From a practical standpoint, however, CubeSats are able to mitigate SEE risks by incorporating appropriate subsystem reset and power-cycling functions as well as watchdog timers. The use of radiation-hardened components is very uncommon in most CubeSat designs.

Vibration & Shock

As a baseline requirement, most CubeSat programs are required to vibration and shock testing as a part of their ride share agreement with the launch provider. Standards such as the NASA General Environment Verification Standard (GEVS) commonly set the requirements for these tests [40]. Additional testing of components with suspected susceptibilities to vibration and shock is left to the discretion of the CubeSat developer.

For the lasercom terminal design considered in this thesis, the primary concern from a vibration and shock perspective are the optical components and fine-steering mechanism. Launch stress induced misalignment in the system's optical paths (particularly in the bistatic design, see section 2.3.3) either need to be reliably controlled or on-orbit calibration methods must be provided. Additionally the potential for damage to moving parts, some of which can not be conveniently secured for launch (e.g., MEMS fine-steering mechanisms), needs to be understood through testing. This level of detailed component testing fell outside of the scope of this thesis, however, there is a significant base of existing work that show that MEMS devices in particular can survive these stresses [49, 50, 51, 52, 53].

2.1.4   Regulatory Constraints

A hybrid RF and laser communication system is subject to a variety of regulatory constraints. Availability of spectrum is a common starting point for many communication system designs. The International Telecommunications Union, which coordinates allocation of the electromagnetic spectrum worldwide, only regulates carriers below 3 THz [54]. Optical carriers at visible at IR wavelengths are unregulated. This is unlikely to change, even as lasercom systems become more prevalent, because of the extremely directional nature of optical transmitters and receivers. Regulation-free access to EM spectrum is, of course, one of the enormous advantages lasercom has over RF systems.

Radio Link

The lasercom system design necessarily incorporates a radio link that is used for command and control of the satellite. This low-rate link is used to assist the pointing, acquisition and tracking process and can also provide precision orbit determination functionality [55]. Command and control functions are typically low data rate (e.g.,

$< 9.6\,\text{kbps}$), so it is envisioned that this link would be implemented as a narrow band modulation of some form.

A license must be obtained for this radio system and the associated ground station network. The underlying licensing process can be complex and is highly dependent on the satellite's country-of-origin as well as sponsor (e.g., governmental, educational, commercial, etc). In [23], this process is described in detail for CubeSats developed in the United States. In general, narrow band allocations (e.g., links that could support a few kilobits per second) are easier to obtain than broad band allocations (e.g., 5 MHz of bandwidth for a 2.5 Mbps downlink).

Laser Safety Regulations

Eye safety is an important design aspect for any system employing free-space propagation of lasers. Both ANSI and IEC provide standards for the safe use of lasers [56, 57]. These standards give guidelines on maximum permitted exposure (MPE) in terms of $\text{W}\,\text{cm}^{-2}$ as a function of wavelength for both ocular and skin exposure. The lasercom system's transmit power, beam divergence angle, and observation distance are used to judge whether the signal is eye safe.

For the downlink laser proposed in this system the signal as observed from the ground is many orders of magnitude below the MPE. The proposed system operates with a 200 mW transmit power at 1550 nm. The ANSI Z126.1 standard specifies an ocular MPE of $0.1\,\text{W}\,\text{cm}^{-2}$ at this wavelength. Assuming a 0.9 mm transmit aperture and a 2.1 mrad half-power beamwidth, the Nominal Hazard Zone (NHZ) is approximately 4.1 m. Clearly, this signal would be well below MPE as viewed from the ground but care must be exercised in ground testing.

For CubeSat missions, there may be additional laser use restrictions imposed by the launch vehicle and (if applicable) its crew. Most CubeSats must inhibit mechanical deployments, communication transmissions and, presumably, laser emissions for a predetermined time after separation from the host launch vehicle [10, 58]. Inhibit requirements are usually satisfied with a mix of hardware and software design features that are scrutinized by the launch services provider.

The eye safety of uplink laser signals, such as those used as a beacon, must also be carefully considered. The safety of bystanders in the vicinity of the ground station must be ensured through NHZ analysis. Even with relatively high transmit powers, uplink systems can usually be rendered eye safe through use of large diameter (15 cm) apertures that keep irradiance ($\text{W}\,\text{m}^{-2}$) below the MPE. As an example, the Lunar Laser Communication Demonstration mission used four 10 W transmitters that were all below MPE because the power was spread across a 15 cm aperture diameter [15].

Other Operational Restrictions: Aircraft & Other Satellites

Aircraft safety must also be considered when fielding a lasercom system. The Federal Aviation Administration (FAA) has published guidelines on the free-space use of lasers [59]. For visible wavelength lasers, which can constitute a distraction hazard for pilots, the FAA has defined strict irradiance limits that can be far below the MPE

defined by the ANSI and IEC standards. These irradiance limits are more restrictive near airports.

Fortunately, invisible wavelengths (e.g., infrared) do not have to abide by these guidelines. Invisible wavelengths, which do not present a distraction hazard, are simply required to follow the normal MPE-based safety standards. For the lasercom system presented in this work, we have opted to use a near infrared beacon laser (discussed in section 2.3.4).

In the United States, upward propagating laser emissions are controlled to some degree by the Department of Defense (DOD) Laser Clearinghouse (LCH) which provides predictive avoidance services for DOD assets. The purpose of the LCH is to prevent lasers from violating treaty agreements. The LCH establishes interface guidelines that allow laser operators to solicit permission to radiate based on laser capabilities, time of day, and orientation. The LCH compares these metrics to the known positions of sensitive assets in order to determine if operation is permissible. Both the OPALS team (NASA JPL) and the LLCD team (MIT Lincoln Laboratory) complied with LCH procedures during their missions.

It is interesting to note that the LCH only has jurisdiction over the United States and its holdings. Staff at the ESA Optical Ground Station (Tenerife, Spain) have reported that LCH approval is not part of their operational procedure [60]. It's not clear whether non-governmental users within the U.S. need to comply with LCH procedures. Astronomical observatories, which make use of uplink lasers to form guide stars, often follow LCH guidelines, especially if they are US Government funded [61].

2.1.5 Component Selection Methodology

In contrast to traditional satellite designs, CubeSat developers are generally not subject to any sort of component selection constraints (e.g., radiation hardness, packaging, etc). Relaxing these constraints opens the design space tremendously by allowing use of newer (and higher performance) components. Microprocessors and memories are one area where these gains are especially significant. Availability and cost are another motivation to employ COTS components where possible. In this study, we place a strong emphasis on the use of COTS components.

2.2 Functional Breakdown

In this section, the high level designs for both the lasercom terminal ("space segment") and corresponding ground station ("ground segment") are presented. Functions needed by each half of the system are enumerated. The space segment discussion also explains design partitioning between the lasercom terminal and the host spacecraft. This section closes with the identification of implementation gaps associated with realizing the system.

2.2.1 Space Segment

Figure 2-2 shows a functional breakdown of the space segment of the lasercom system. A high-speed electronics unit accepts data for downlink from the host spacecraft. Forward error correction and interleaving are applied to this data to make it resilient to channel impairments, then the data is stored in a buffer where it awaits transmission. A low-rate bidirectional radio link is integrated into the lasercom payload to allow command and control of the satellite as well as coordination of the high-rate optical downlink.

The optical assembly incorporates a focal plane array and associated optics for tracking the uplink beacon signal. Pointing offset knowledge from this detector informs the fine-steering mechanism, as well as the host spacecraft's attitude control system. The transmit optical path consists of a laser transmitter, the fine-steering mechanism, and appropriate collimation optics.
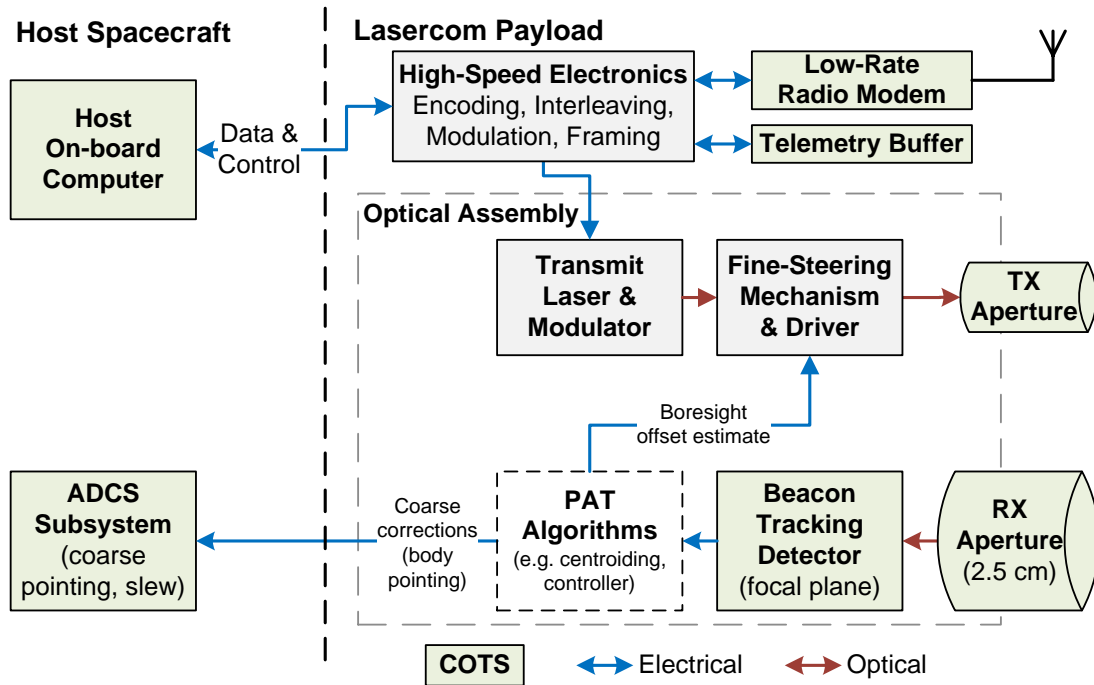
Figure 2-2: Functional block diagram for space segment design showing partitioning of functions between the lasercom terminal and the host spacecraft. Components with existing COTS solutions are highlighted in green.

The majority of the space segment building blocks have existing COTS solutions. Notable exceptions include the laser transmitter, the fine steering mechanism, and the various high-speed processing and algorithmic functions. The missing pieces and contributions made in this dissertation, mainly the laser transmitter and the fine-steering mechanism, are the subject of Chapter 3 and Chapter 4. The pointing, acquisition and tracking (PAT) algorithms are the thesis topic of graduate student Kathleen Riesing, who is a collaborator on the project.

42

2.2.2 Ground Segment

Simplicity and cost are important design drivers for the ground segment (Figure 2-3) In order for lasercom to be competitive with RF alternatives, end users would ideally be able to construct a suitable ground station using commodity hardware. By contrast, many existing lasercom systems rely on exotic components such as high performance detectors (e.g. superconducting nanowire detectors) and meter-class telescopes [15, 62]. The design presented in this thesis restricts the receive aperture to 30 cm.
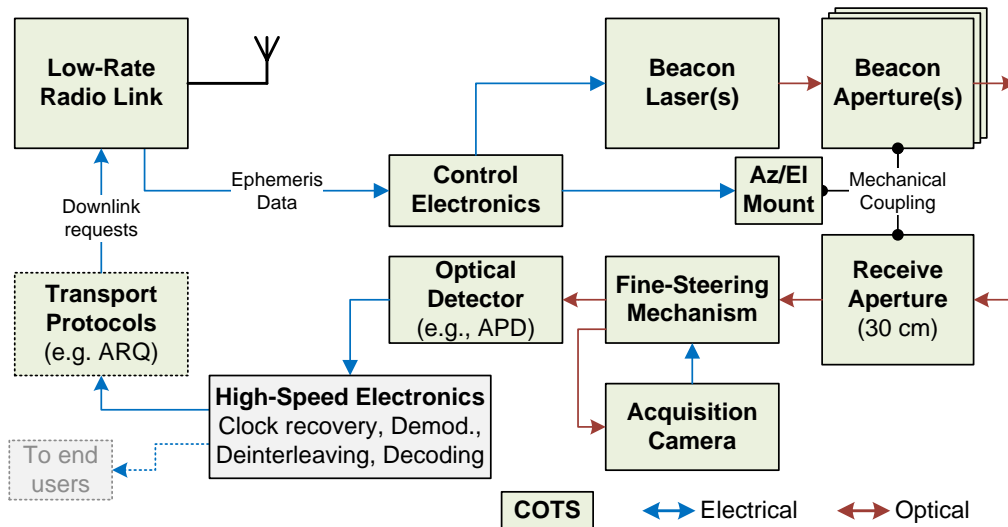
Figure 2-3: Functional block diagram for the ground segment. Components with existing COTS solutions are highlighted.

A wide variety of COTS telescopes are available in the 30 cm regime. Mounts capable of tracking LEO objects, where apparent angular motion can reach $1\,°\,s^{-1}$, are also available from commercial sources [63, 64, 65]. A fine-steering mechanism may be necessary to reject telescope pointing errors and to steer the downlink energy on to a small-area COTS detector such as an avalanche photodiode (APD). This fine steering mechanism would be informed by an acquisition camera that is sensitive at the downlink wavelength (e.g., InGaAs camera for 1550 nm downlink).

The uplink beacon signal will be transmitted by one or more apertures piggy-backed on to the receive aperture mount. The divergence of the uplink beacon signal will be sized so that the entire uncertainty region of the spacecraft's position is illuminated. Position uncertainty is expected to be composed primarily of orbit determination error (2 mrad at 1000 km acquisition range). Multiple uplink apertures will be used to help mitigate scintillation [66]. Multiple uplink apertures can also be useful for reducing the nominal hazard zone of the beacon signal.

The high-speed electronics, which convert the optical signal from the detector into an electronic data stream, largely mirror the functionality present in the space segment high-speed electronics. One notable difference is the addition of clock recovery circuitry, which is needed to recover the slot and symbol clocks from detected

signal. Clock recovery techniques have been thoroughly studied in prior lasercom projects [67, 68, 69].

Even though the majority of the ground station components are COTS, significant engineering effort is needed to assemble these components into a working ground station. Integration of the fine steering mechanism with the communications detector and acquisition camera will require a custom optics bench. Mounting the beacon apertures to the telescope mount, will require careful alignment [60]. Finally, the coarse pointing performance of the mount will need to be calibrated and validated against real LEO objects.

2.2.3   Implementation Gaps

Figure 2-2 and Figure 2-3 identify which of the major functional blocks are available as COTS products at present. For the space segment, ready-made solutions are not available for the optical transmitter or fine steering mechanism which are compatible with CubeSat SWaP constraints. These two subsystems are the most significant technical hurdles to overcome for a flight demonstration. Other missing components, such as the high-speed electronics and the pointing, acquisition and tracking (PAT) algorithms, are non-trivial but viewed as less risky since there are existence proofs. FPGAs, including commercial variants, have flown on numerous CubeSat missions. The PAT algorithms are an expected to be an application of existing staged control techniques, but some customization will likely be necessary given the limited hardware constraints [70, 71]. The development of PAT algorithms will form the basis for another student's dissertation [72].

2.3   High-Level Design Choices

Many of the high-level design decisions have been based upon assumptions about the concept of operations, particularly with regard to link setup and acquisition process. This process is first described from start to finish to set the stage for the underlying design decision narrative.

In advance of a communication's pass, the ground segment uses the RF command and control link to upload recent orbit determination information and information on the ground station location to the CubeSat. A few minutes before the start of the pass, the CubeSat autonomously (it is assumed to be out of radio range) slew from it's mission-specified attitude to an attitude where the beacon receiver aperture is pointing at the estimated direction of the ground station[1]. Simultaneously, the ground station illuminates the estimated CubeSat location with the uplink beacon signal.

Once the CubeSat beacon camera acquires the beacon signal, ground station relative attitude determination improves significantly. Knowledge of attitude error with respect to the ground station is fed to the host CubeSat ADCS to allow it to improve

---

[1]This design may result in a scenario where the primary mission has to be suspended to support the communication pass. This is a common constraint on many CubeSat missions.

44

the body pointing performance[2] The attitude error estimate is also fed to the fine-steering mechanism to further improve pointing performance of the downlink signal Once the ground station's clock and data recovery circuitry gets "lock" on a synchronization or pilot signal, communication can commence. It is likely that the RF link will be used to provide protocol-based transport reliability guarantees over the link. It is also likely that the return link will be used to provide dynamic rate adaptation in response to channel fluctuations (most notably, range).

2.3.1   Beam Divergence Selection

Beam divergence angle is the most important parameter in determining the link efficiency (joules-per-bit) of the lasercom link. This parameter also directly dictates the pointing requirements for the system, forming a trade space with data rate.

Given limited transmitter power and an assumed receiver aperture and sensitivity, what beam divergence must be used to achieve the desired data rate? How does this beam divergence compare with the current state of CubeSat ADCS technology?

To answer these questions, an iterative design approach was used that started with the power budget for the lasercom terminal. To be competitive with RF solutions, the lasercom terminal's power consumption is not to exceed 10 W during transmit (we assume the host ADCS is powered separately from the lasercom terminal, the power numbers are for the lasercom terminal only). It was predicted that half of this budget would be needed for the terminal's high-speed processing electronics (e.g., field programmable gate array (FPGA), acquisition camera, etc). The remaining 5 W were earmarked for the laser transmitter.

A radiometric analysis approach (as in Section 1.3.4) was used to predict achievable data rate for a given beam divergence. Reasonable assumptions were made for transmitter "wall-plug" efficiency (10%), free-space path loss (1000 km), and for receive aperture gain (30 cm at diffraction limited gain). We also assume a ground receiver that requires 1000 photons per bit[3]. Figure 2-4 shows the expected squared relationship between beamwidth and data rate, along with the target data rates for the system.

The region of the trade space currently accessible with $\pm 1°$ (3-σ) ADCS solutions is indicated on the plot. Previous missions with on-orbit pointing results are also shown [19, 73, 74, 75]. The reported pointing performance for these missions are sensing-limited and are with respect to an inertial frame target, rather than a ground target. Precision ground target tracking requires simultaneous high-rate slew, which presents additional engineering challenges (e.g., variable reaction wheel disturbances, star tracker image blurring, non-rigid body dynamics). Beacon-based attitude measurements (addressed in Section 2.3.2) will provide some relief to existing sensing limitations, however, we also expect high-rate slew to degrade pointing. In this work,

---

[2]Given the high angular accuracy of camera-based centroiding, it is believed that this host Cube-Sat will be "actuation limited" with this added determination knowledge.

[3]This was chosen as a starting point for an easy-to-implement receiver. Numerous COTS-based receivers have been reported in the literature that exceed this sensitivity [35, 36].
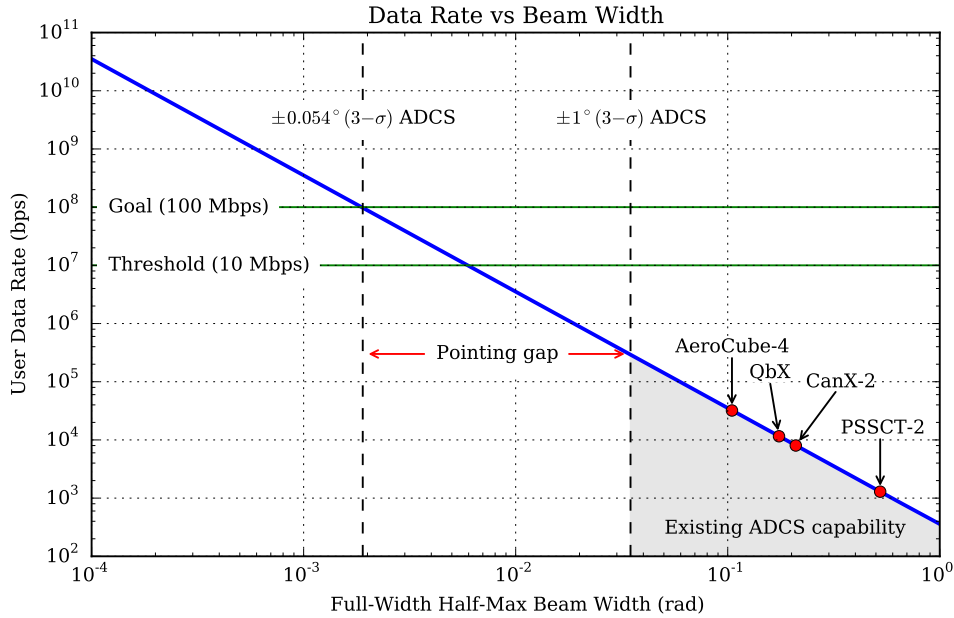
Figure 2-4: User data rate vs beamwidth in a system with a perfect receiver operating at 1000 photons per bit. The region accessible with $\pm 1°$ (3-σ) ADCS capability is shaded in gray and missions with on-orbit results are indicated.

we don't attempt to weigh these competing effects and instead proceed with the design assuming a baseline pointing capability of $\pm 1°$ (3-σ) .

We note that there is a large spread between on-orbit results and capabilities advertised by COTS ADCS component vendors. One example is the Blue Canyon Technology XACT ADCS product which claims $\pm 0.021°$ (3-σ) pointing performance [76]. This XACT unit incorporates a star tracker to address the sensing limitations of prior systems. At the time of writing, high performance systems like the XACT had not been validated on orbit and are still considered to be a rare capability among most 3U CubeSat designs.

Given the conservative assumption that the host CubeSat is only capable of providing $\pm 1°$ (3-σ) pointing, the radiometric analysis shows that a large pointing gap exists. Beam pointing performance needs to improve by roughly a factor of 20x in order to facilitate laser communications at 100 Mbps while staying within power budget.

Point-Ahead Requirements

Some lasercom systems employ "point ahead" (or equivalently, "look behind") mechanisms to compensate for terminal movement during the light propagation time. Generally this is implemented with a tip-tilt mirror or a fiber nutator. Point ahead functionality is not needed for the system presented in this thesis. The worst-case point-ahead angle for a 450 km altitude LEO object viewed from the ground is ap-
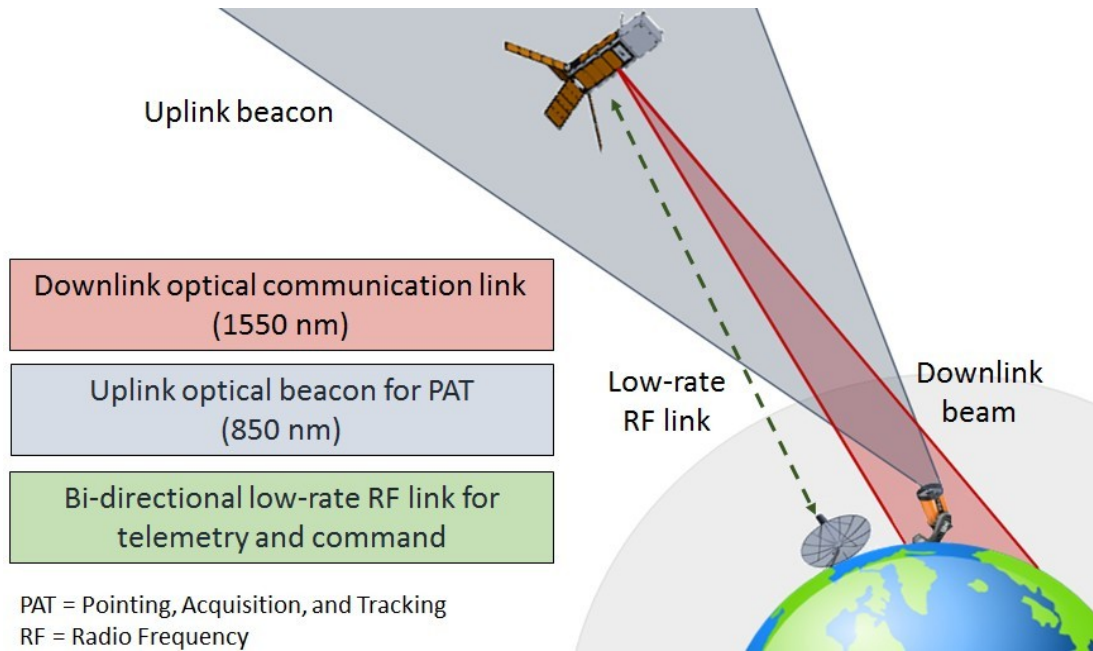
Figure 2-5: Diagram showing a lasercom system configuration integrating an uplink beacon signal. The beacon signal allows the satellite to directly measure pointing error with respect to the ground station. Wavelength diversity is normally used to isolate the ground station downlink receiver from scattered beacon light.

proximately 50 µrad which is a small fraction of the planned beam divergence.

2.3.2 Beacon vs Beaconless Design

Lasercom systems often implement beacon systems (Figure 2-5) to provide additional knowledge to the pointing, acquisition and tracking subsystem (Section 1.2) but, as was discussed in section 2.1.4, beacons often carry laser safety and operational burdens[4]. Supporting a beacon also levies requirements on the space terminal hardware such as collection optics and processing electronics. In this severely SWaP constrained application, both approaches were considered.

The notional control loop design for a beaconless system is presented in Figure 2-6. This system necessarily incorporates a variety of knowledge sources in order to determine pointing commands. The spacecraft's position must be known through some form of precision orbit determination such as uplinked ephemeris or an on-board GPS receiver. Knowledge of the spacecraft's position is compared to the (assumed fixed) location of the ground station to compute a nominal pointing vector. Finally, this pointing vector is compared to on board attitude measurements to derive correction signals that are fed to the attitude actuators.

All of the above steps introduce error sources that can impact overall performance. As an example, a hypothetical system employing 2 mrad downlink beam operating at a

---

[4]We have not identified any LEO-to-ground lasercom system designs that are truly "beaconless." Systems described as beaconless usually leverage a return optical link in place of a beacon.

1000 km acquisition range, would need to be able to provide better than 2 km position accuracy. Similarly, the attitude sensors available today aren't able to perform at this level [77].

Architecturally, the beaconless design makes the lasercom terminal performance extremely reliant on the capabilities of the host spacecraft. A complex tree of dependencies and paths for error propagation make the system difficult to analyze and prone to failure. This compromises one of the central goals of the thesis: to develop a system that is compatible with the "typical" 3U CubeSat.
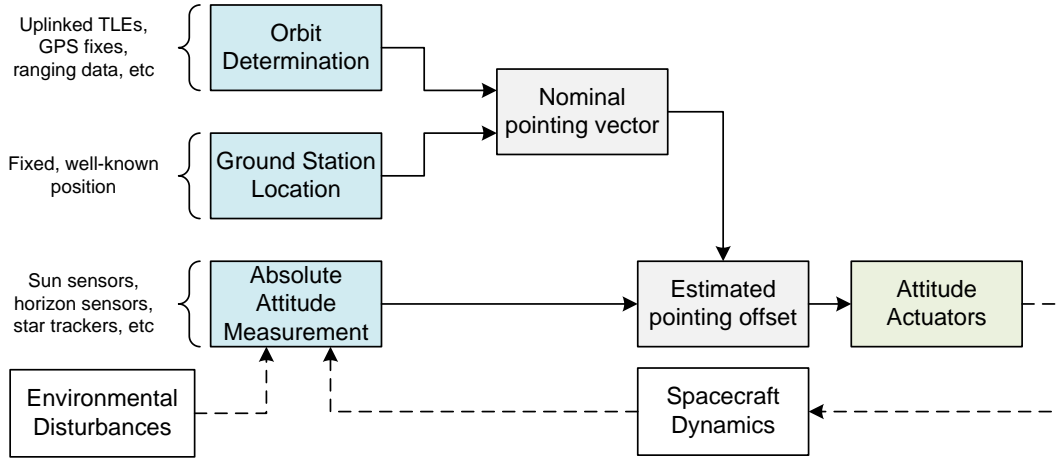
Figure 2-6: Pointing control loop without using a uplink beacon. Absolute attitude measurements (e.g., star tracker data) are fused with orbit determination and ground station location data to compute pointing error.

Figure 2-7 shows a beacon-based system control loop. The beacon enables direct measurement of the spacecraft's pointing error relative to the ground station. Typically a camera or quadcell (effectively a four-pixel camera) is used to measure the pointing offset. Knowledge of the spacecraft's absolute orientation is still needed for acquisition, but these sensors only need to perform to a level sufficient for getting the beacon signal within the field of view of the camera.

From an electronics perspective, the beacon-based system is more complex than the beaconless one. The design requires an additional sensor (e.g., a focal plane array) and processing electronics (e.g., a processor or FPGA implementing a centroiding algorithm). The main advantage, however, is that the fine pointing performance can be decoupled from the host spacecraft's pointing performance provided the coarse stage is able to meet a baseline pointing accuracy requirement. Prior work on stochastic staged control systems have shown that it is possible to provide guarantees of this decoupling given sufficient overlap between the stages [70].

In order to make this system applicable to a wide variety of CubeSats, it is highly advantageous to minimize the design dependencies between the lasercom terminal and the host spacecraft. Additionally, most current CubeSat ADCS systems are currently sensing-limited [19, 73, 74, 75]. Beacon-based attitude measurements help to address
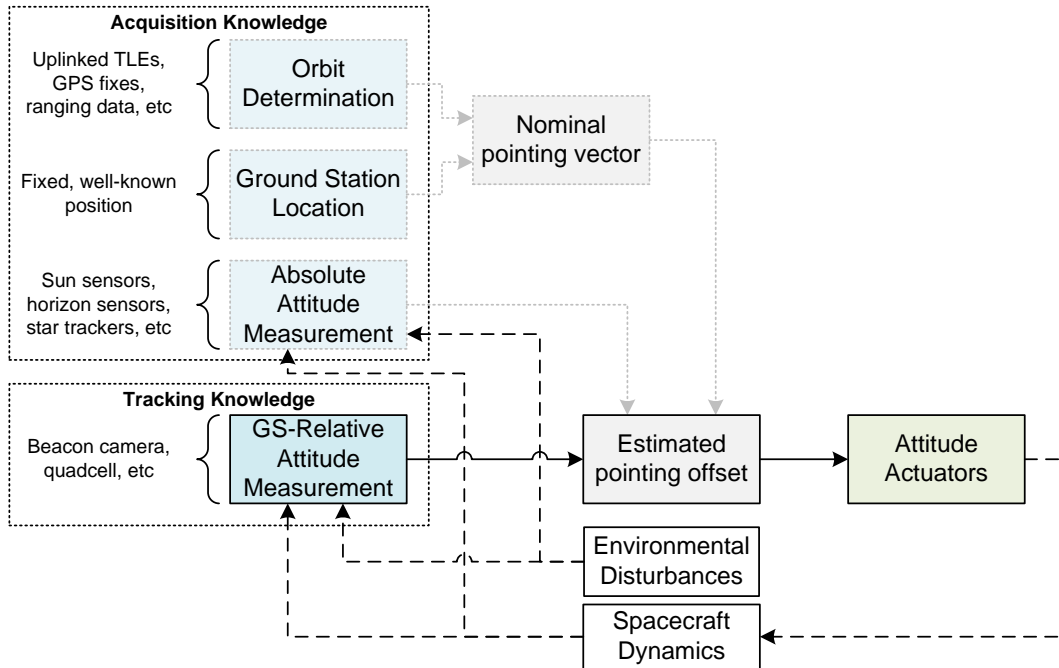
Figure 2-7: Pointing control loop using a beacon signal allows direct measurement of satellite pointing error relative to ground station. Absolute attitude measurement and orbit determination systems, or alternatively a time-consuming search process, are necessary in order to get beacon signal within field of view of relative attitude sensor (e.g., beacon camera).

these limitations. For this reason, a design incorporating a beacon has been selected for further development.

Beacon Alternatives

We note that there may be alternatives to active beacon systems. Specifically, it may be possible to use other identifiable ground signatures to provide ground-station-relative attitude knowledge to the host spacecraft. As an example, if the host spacecraft has an imaging capability, it is conceivable that this sensor could be used to identify and track either natural (terrain) or man-made (e.g. fiducial) ground features using 2D image correlation or other image feature tracking methods [78].

Similarly, if coherent sources are undesirable for regulatory reasons, it may be possible to use incoherent light sources such as high-power LEDs. COTS LEDs offer very high output power ($> 5\,\mathrm{W}$ per unit) and beamwidths down to $5°$. These beamwidths are not competitive with laser transmitters but their high output power and lightweight construction enables construction of large arrays that can produce equivalent radiance. The broad beamwidth of an LED-based beacon also simplify pointing and tracking requirements for the transmitter.

2.3.3 Optics Design: Bistatic vs Monostatic

Optical components present a variety of mechanical and thermal design challenges for aerospace applications [79]. Optical assemblies commonly carry strict thermal and alignment requirements and can be susceptible to vibration and shock damage. Satisfying these constraints usually requires special structures which can become significant terms in the mass budget. Minimizing these design complications was a guiding principle in the lasercom terminal's optical design.

From a high level, the terminal's optical assembly needs to support the following functions:

1. Coupling of the downlink transmit signal from a fiber into a free-space beam with the desired divergence angle.

2. Fine steering of the transmit signal relative to the spacecraft's body frame, subject to range and resolution requirements dictated by the PAT system design.

3. Collection of the uplink beacon signal and focusing onto a suitable detector (e.g., focal plane or quadcell).

4. Establish and maintain alignment between the uplink and downlink optical paths.

Most lasercom systems demonstrated to date perform all of these functions with a single telescope aperture. This configuration is known as monostatic and is often preferable as it only requires a single coarse pointing mechanism (e.g., a gimbal). A monostatic configuration also enables straightforward coarse alignment between the incoming and outgoing optical signals. Fine alignment, as well as point-ahead (Section 2.3.1), is implemented with fine steering mechanisms present on either the transmit path or receive path (or both).
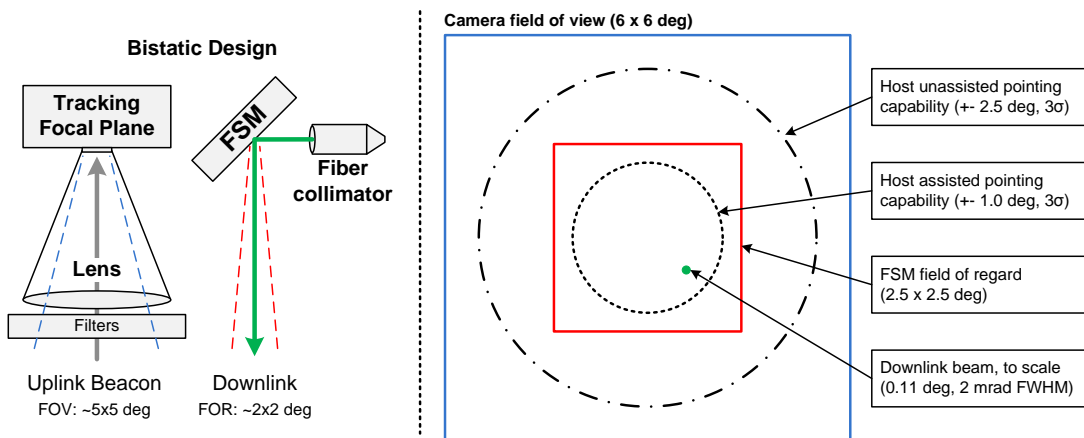
Figure 2-8: Monostatic configurations utilize a single aperture along with beam combining optics. Bistatic configurations have independent apertures for receive and transmit signals.

Lasercom systems with relatively wide beamwidths (e.g., OPALS with a 1 mrad downlink beam) open up the possibility of using independent apertures since alignment is less demanding. Designs of this type, commonly known as bistatic, normally implement a larger receive aperture (needed for light collection purposes) and a smaller transmit aperture. By separating the two signals it is possible to design and optimize the optical paths independently, minimizing scatter and allowing full duplex operation without extreme optical filters. This can be valuable in systems employing different wavelengths (e.g., 850 nm uplink beacon and a 1550 nm downlink signal). It also can enable the use of COTS lens assemblies, rather than custom optics benches.

For this project, a bistatic approach was developed around the use of COTS components. The beacon receiver uses a COTS focal plane array and integrated C-mount lens system. This beacon receiver is rigidly mounted to a transmit optical assembly that houses a fiber collimator and fine-steering mechanism. The fiber collimator, which is a COTS fixed-focus unit, establishes the desired downlink beamwidth and illuminates the fine-steering mechanism. This transmit optical arrangement, known as a "gimballed flat" configuration, was used for very early lasercom systems [80, pg 108].

One distinct disadvantage of the bistatic configuration is the lack of optical feedback between the fine-steering mechanism and the beacon tracking detector. This type of feedback could normally be used to correct for any nonlinearities in the fine-steering mechanism, Unfortunately, the very small fine-steering mirrors under consideration for this application are difficult to interface with COTS detectors due to their small diameters. Beam walk-off, which occurs when off-axis light is translated off the mirror surface, must be mitigated with a custom optics assembly. The open-loop performance of the fine-steering mechanism will be addressed in Section 3.2.

Co-boresighting Apertures

In the bistatic optical configuration, maintaining a co-boresight between the two optical paths is crucial for reliable performance. Initial alignment in the laboratory can be accomplished by illuminating a "finder card" with the 1550 nm downlink signal with the fine-steering mechanism in a known position (e.g., neutral/origin). This material fluoresces at a wavelength that can be imaged by the beacon camera when the optical bandpass filter has been removed. A centroiding process, identical to the one used for beacon tracking, can be used to infer the alignment error between the two systems.

Alignment errors that arise due to launch stresses, aging and thermal cycling must be managed on orbit. A variety of options exist for managing these problems are being considered:

1. use of ground-based optical power measurements, in conjunction with a raster or spiral scan of the steering stage to provide on-orbit calibration of alignment error

2. on-board sensing of steering mechanism position though a combined optical system

3. design of a more robust optical component mounting scheme that is more re-
   silient.

The final selection will likely be determined by cost and implementation complexity.

2.3.4   Wavelength Selection

Wavelength selection was primarily dictated by atmospheric transmittance, the avail-
ability of components needed for the transmit lasers (beacon and downlink), the
communications detector (at the ground station), and the beacon receiver. A sec-
ondary wavelength selection criteria were eye safety related operational concerns (Sec-
tion 2.1.4).

For the downlink, wavelength selection was dictated by the availability of power-
efficiency transmitter components. Early candidates included high-power "pump"
diodes (975 nm), yttrium-doped fiber amplifiers (YDFAs, at 1064 nm), and erbium-
doped fiber amplifiers (EDFAs, at 1550 nm). The wavelengths of these components
coincide with favorable atmospheric transmission windows (Figure 2-9) and efficient
COTS detectors (e.g., Si and InGaAs APDs). Section 3.1 discusses the transmitter
trade-study and down-selection criteria for a 1550 nm downlink in greater detail.
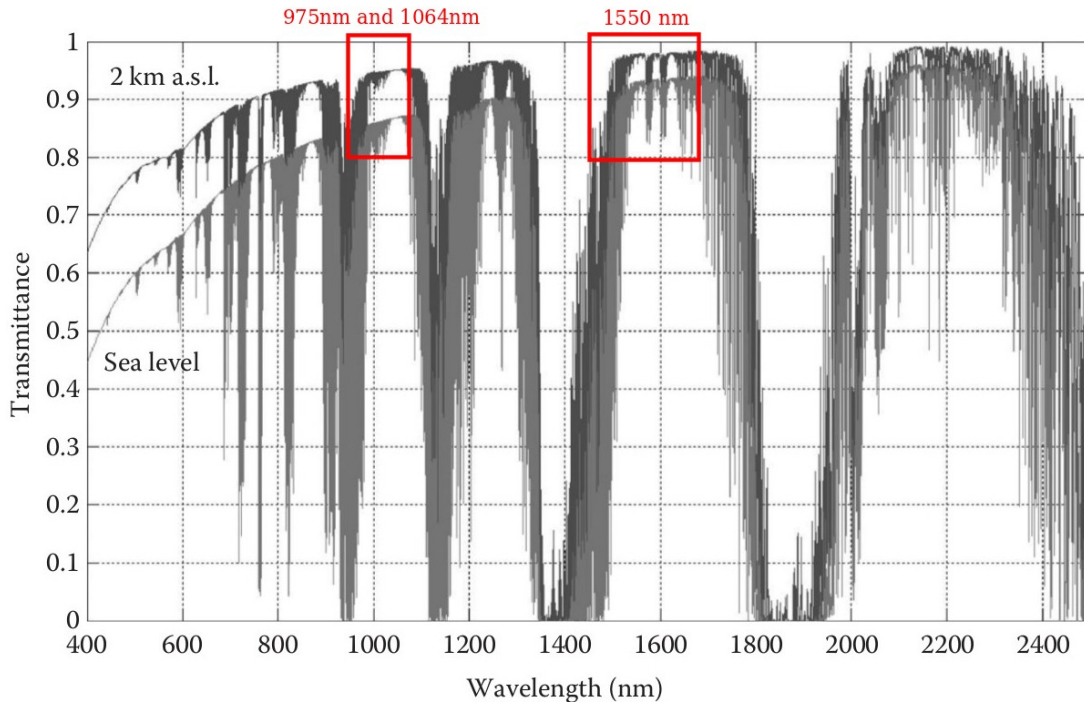
Figure 2-9: Atmospheric transmittance for an Earth-to-space path at zenith from [5].
Two observer scenarios are shown: one at sea level and another at 2 km above sea level.
Transmission windows coincide with 1000 nm and 1550 nm transmitter technologies.

The uplink beacon wavelength selection process was primarily driven by the avail-
ability of low-power detectors. The pointing subsystem design demanded a sensor

capable of resolving the beacon signal while simultaneously providing a wide field of view ($5° \times 5°$, or $87\,\text{mrad} \times 87\,\text{mrad}$) and sub-beamwidth resolution ($210\,\text{µrad}$). Focal plane arrays are frequently used for this purpose. An image is captured, then a centroiding algorithm is used to identify the position of the beacon spot within the image. A quadcell (effectively a four-pixel camera running de-focused) can also be used, but these typically have a limited FOV which then must be scanned across a larger field of regard. The focal plane array is advantageous because it allows for near instantaneous measurement of the entire pointing uncertainty region.

Low cost, low-power and compact focal plane arrays have seen enormous advancement in the past decade, primarily due to the consumer electronics industry. These devices are fabricated in silicon and are appropriate for use at visible and near infrared (NIR) wavelengths ($400\,\text{nm}$ to $1000\,\text{nm}$). At longer wavelengths (i.e., $> 1000\,\text{nm}$) silicon becomes transparent and InGaAs is used for focal plane construction. InGaAs-based sensors tend to consume more power than Si sensors due to the need for active cooling of the array. Silicon arrays are more favorable from a cost and power perspective.

Given an Si-based focal plane array, wavelength selection is confined to roughly $400\,\text{nm}$ to $1000\,\text{nm}$. Visible wavelengths ($< 700\,\text{nm}$) are highly undesirable due to eye safety and aircraft distraction hazards (Section 2.1.4). Among the invisible NIR wavelengths, eye safety is still an important design concern for the uplink beacon. The nominal hazard zone (NHZ) distance can be controlled through judicious selection of beam divergence and beam waist. Given focal plane performance parameters and the eye safety concerns, an $850\,\text{nm}$ beacon wavelength was selected.

2.3.5   Modulation

A wide variety of modulation formats are used in optical communication systems and many of them are designed to leverage the effectively-unlimited bandwidth available at optical frequencies (see, e.g., [36, 35]). Coherent techniques, which mirror modern radio designs, work by mixing a local oscillator laser with the incoming receive signal to recover the amplitude, frequency and phase of the optical signal. These systems can provide sensitivity advantages (i.e., mixing gain) but require stabilization of the transmit laser as well as alignment of the receiver local oscillator laser. Neither of these are power-friendly or COTS-friendly requirements to satisfy.

Intensity modulation (IM) is another popular technique in optical communication system designs. IM signals can be directly detected by a photodiode, photo-multiplier tube, or photon counting detector. The simplest IM scheme is on-off-keying (OOK) which uses the intensity of the transmitter to encode bits. OOK modulation is prevalent in fiber communication systems. OOK can be recovered with COTS clock recovery units and require relatively low bandwidth with respect to the link data rate. This can be advantageous when selecting a suitable detector. One downside to OOK modulation is that the receiver needs to identify a suitable threshold between "on" and "off." This can be challenging when the signal has been corrupted with noise and stray light interference.

Another popular IM scheme, which is popular in lasercom systems, is pulse po-

On-Off Keying Modulation:
Each symbol caries one bit

Pulse Position Modulation:
PPM-16 carries four bits per symbol, an always-off guard slot added for symbol timing recovery
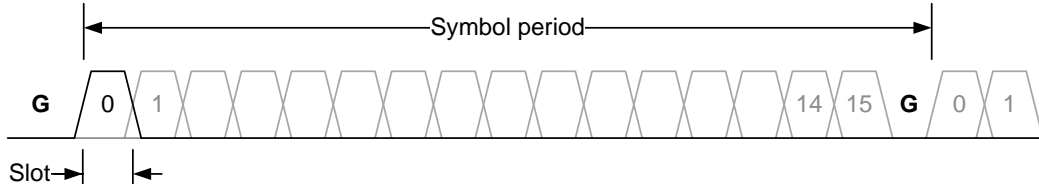
Figure 2-10: Timing examples for OOK and PPM modulation formats. PPM has higher signal bandwidth but lower duty cycle than OOK for a given data rate. Low duty cycle allows PPM to achieve higher peak transmit power from average-power-limited amplifiers.

sition modulation (PPM). M-ary PPM encodes data into symbols consisting of M slots (Figure 2-10). This allows each symbol to encode $\log_2 M$ bits per symbol. Some notable advantages of PPM over OOK are that it is "self thresholding" (the receiver simply chooses the highest intensity slot) and that it has a low duty cycle, which can be advantageous in average-power-limited transmitters. Bandwidth expansion, which is caused by moving to increasingly large M, is generally not a problem in the optical domain but it can push the capabilities of detectors which often trade bandwidth for sensitivity and coupling area.

Given the impractical nature of low-SWaP coherent lasercom systems, which require extremely stable lasers, this system focuses on the use of intensity modulated, directly detected modulation schemes such as OOK and PPM. Further examination of these choices is given in Section 3.1 since the choice of a modulation is dependent on the underlying transmitter technology.

2.3.6 Forward Error Correction & Interleaving

Forward error correction (FEC) and interleaving are particularly useful in mitigating channel impairments in free-space optical communication systems operating over a turbulent optical channel (see, e.g., [81, 82, 83, 13]). The selection of an FEC and interleaving scheme for a given communication link is a deep technical topic and enormous effort has been expended to design codes that can perform within fractions of a decibel of the Shannon limit. For the purposes of this application, we are primarily motivated by implementation simplicity rather than best-in-class performance, though a stronger code could certainly be used to enhance link performance.

The underlying physical layer has been designed to provide a 1×10^{-4} bit error rate. At this bit error rate (BER) even simple codes, such as a 7% overhead Reed-Solomon

(i.e., $RS(255, 239)$) can provide near error-free output. Reed-Solomon codes are block codes, meaning that they operate on finite length code words and are able to repair a certain number of erroneous symbols within each code word. As an example, the $RS(255, 239)$ code can repair up to eight erroneous symbols per 255 symbol code word [84].

Free-space optical channels are also characterized by long duration (i.e., milliseconds) outages which impart burst errors in the received signal [5, Sec 6.4]. Correlated channel errors, also known as burst errors, are problematic for block FEC methods (e.g., Reed-Solomon codes) because they can result in loss of entire code words. Put differently, even at the specified 1×10^{-4} BER, a $RS(255, 239)$ is ineffective due to the temporal distribution of the errors. When combined with FEC, interleaving techniques, which spread out code words in time, can mitigate the fading channel impact [81, 82, 83, 13]. Free-space optical communication systems commonly employ 1 s deep interleaving, though the exact value depends on the channel coherence time and the capabilities of the FEC [5].

It is important to note that the interleaving process adds end-to-end latency to the communications link. For the "store and dump" concept of operations for LEO Cube-Sats, this latency is inconsequential since the data has already experienced minutes or hours of latency while stored on the spacecraft. Note that latency of the optical link can make it challenging to use the optical link for real-time control purposes (e.g., link coordination, or closure of control loops).

For the purposes of this thesis, we will not delve deeper into the design and selection of an error correcting code or interleaver. We will proceed with under the assumption that a low overhead code will be used and that the underlying physical layer can deliver a 1×10^{-4} BER. Since this is a transmit-only design, the SWaP-constrained transmit hardware only needs to implement FEC encoding (as opposed to decoding) which is feasible in modern FPGAs. The interleaving process will also be performed by an FPGA and attached memory. This too is relatively straightforward to provide given that a (convolutional) interleaver only requires a 50 Mbit of memory to provide a 1 s interleaving depth for a 100 Mbps link. In the flight design, we assume that both FEC and interleaving functions will be provided by the same FPGA that performs modulation and framing.

2.4   Link Budgets

Link budgets were used to predict performance of the downlink laser communications channel and the uplink beacon signal. The analysis approach for each link differs due to the differences in detector technology: an APD and a focal plane array, respectively. The bi-directional RF link is not in the scope of the thesis, it is assumed to exist and to be reliable [85].

---

[5]A code block re-transmit mechanism is another alternative to interleaving, however, it comes at the price of overhead necessary to convey ACKs/NACKs back to the transmitter.

2.4.1   Optical Downlink

The link budget presented in Table 2.1 corresponds to a system consisting of a fiber amplifier transmitter and an APD detector providing a M-ary PPM communication link. Unlike the radiometric analysis presented in Section 1.3.4, this analysis incorporates performance of a COTS receiver based on manufacturer specification. Although many of the parameters included in this budget match the design as built and validated in Chapter 4, many other transmitter/receiver permutations were considered during the early stages of system design. Some of these intermediate design results are presented in Section 3.1.

Transmitter Parameters

The transmitter is assumed to be a master oscillator power amplifier (MOPA) design consisting of a directly modulated seed laser followed by an average-power limited erbium-doped fiber amplifier (EDFA), producing 200 mW at 1550 nm. A M-ary PPM waveform at a fixed slot rate of 200 MHz is also assumed. Modulation order M is allowed to vary between 4 and 64 resulting in channel data rates ranging from 18.75 Mbps to 100 Mbps. A finite extinction ratio of 33 dB is assumed, which minimizes transmitter "power robbing" effects at the modulation duty cycles of interest [36, 82]. A fiber collimator establishes a 2.1 mrad (0.12°) full-width, half-max downlink signal. An additional 3 dB of transmitter optical losses are included to account for implementation losses (e.g., couplers for self-test purposes, optical throughput of fine-steering mechanism, etc).

Channel Parameters

The channel is a 1000 km path length space-to-ground link, which corresponds to a 20° viewing elevation angle (equivalently, a 70° zenith angle) for a 400 km altitude LEO object. The standard free-space path loss equation is used to determine diffraction loss. Additionally, the link budget includes an atmospheric loss term that accounts for scattering, absorption and turbulence. Predictions from a MODerate Resolution Atmospheric TRANsmission (MODTRAN) model, as presented in [5], led to the use of 1 dB as a conservative baseline for atmospheric losses.

   A pointing loss term is also captured in the link budget. We assume a fixed pointing loss of 3 dB as a result of a requirement placed on the pointing subsystem. The pointing subsystem is required to provide 3-σ pointing performance better than the half-power beamwidth (i.e., -3 dB point) of the downlink signal. The pointing system may be capable of exceeding this performance requirement, which provides motivation for a *rate-scalable* transmitter that can provide link rates that are unfeasible under current system assumptions.

Receiver Parameters

At the ground station, a 30 cm aperture delivers the receive signal to a COTS APD-TIA module (Voxtel RDC1-NJAF). Coupling between the telescope and the detector

is accomplished with an acquisition sensor and fine-steering mechanism as described in section 2.2.2. The coupling loss between the telescope aperture and the detector is assumed to be $2\,\mathrm{dB}$. The receive optics also include an optical bandpass filter ($1\,\mathrm{nm}$ bandwidth) centered at the communications wavelength to reject stray light, such as a day-time sky radiance.

The receiver sensitivity analysis accounts for shot noise (signal and background) as well as detector noise. Even though APD output statistics are best modeled as Poisson processes, this application uses relatively high photon flux (greater than 100 photons per "mark" slot) where a Gaussian approximation is sufficient [86, 35]. Additionally, the detector's TIA contributes thermal noise to the receive signal which is also Gaussian distributed. Use of Gaussian statistics greatly simplifies the performance analysis and allows closed-form solutions for BER given the "mark" and "space" signal means and variances. A detailed description of the receiver performance analysis is provided in Appendix A.

2.4.2 Beacon Signal

The beacon signal is used by the lasercom terminal to estimate the boresight offset of the coarse pointing stage. The beacon receiver is essentially a camera which images the coarse stage pointing uncertainty region. The beacon signal generates a spot on this image which undergoes a centroid calculation to determine a displacement on the detector. This displacement is subsequently mapped into an angle relative to the system boresight. This process is divisible into two steps:

1. Unambiguous identification of the beacon signal from other signals in the receiver's field of view (FOV).

2. Centroid calculation performed upon a region of interest (ROI) defined as a result of the previous step.

The first step, unambiguous beacon identification, is complicated by a variety of link and environmental effects. First, the beacon signal is subject to scintillation and fading due to the atmosphere. This well-studied problem is best mitigated with spatial diversity at the ground station (i.e., use of multiple beacon apertures) [66, 87]. Second, the beacon receiver field of view is filled with terrain and cloud features which can produce significant optical signals in the band of interest, these potentially lead to false positives. The OPALS system, which uses an uplink beacon at $975\,\mathrm{nm}$, frequently experienced beacon tracking disturbances due to optical glints from water bodies, snow-covered mountains, and clouds that were in the vicinity of the ground station [88]. These interference events can be mitigated in a variety of ways including optical bandpass filtering, modulation of the beacon or by providing extra power margin[6].

The second step, centroiding, uses a center-of-mass calculation to determine the center of the beacon spot. This calculation is typically only performed on a small

---

[6]Even very slow modulation rates (i.e., $< 2\,\mathrm{Hz}$), which are compatible with camera frame rate limitations, can be effective against background noise.

Input Parameters	Low rate	Mid Rate	High Rate	Units	Notes
Channel data rate	18.75	31.25	50	Mbps	Calculated channel data rates (excludes FEC, frame overheads)
Target BER	1.00E-04	1.00E-04	1.00E-04	-	
Slot rate	2.00E+08	2.00E+08	2.00E+08	Hz	Fixed slot rate (constrained by laser chirp, clock recovery)
PPM order	64	32	16		Number of slots per symbol
Laser Transmitter					
Average optical output power	0.20	0.20	0.20	W	Average optical output power
Laser wavelength	1550	1550	1550	nm	Peak wavelength
Extinction ratio	33.00	33.00	33.00	dB	Only used for "power robbing" correction.
Half-power beamwidth	0.120	0.120	0.120	degrees	
	2.094	2.094	2.094	mrad	Full cone angle where power is half of peak intensity
Transmit optical losses (dB)	-1.50	-1.50	-1.50	dB	Conservative estimate for collimator+EDFA output coupler+mirror loss
Channel					
Path length	1000	1000	1000	km	LEO at 400km can be tracked down to 20 degrees above horizon
Atmospheric loss	-1.00	-1.00	-1.00	dB	Absorbtion, scattering, turbulence
Pointing loss	-3.00	-3.00	-3.00	dB	Worst-case placeholder
Receive Telescope & Optics					
Focal length	3	3	3	m	Used to calculate FOV of sensor for background noise
Aperture diameter	30	30	30	cm	
Receive optics losses	-2.00	-2.00	-2.00	dB	Placeholder, based on JPL OPALS
Background Noise (Sky Radiance)					
Field of view (full cone angle)	6.67E-05	6.67E-05	6.67E-05	rad	Voxtel APD is 200um diameter
Sky Spectral Radiance	6.00E-04	6.00E-04	6.00E-04	W/(cm^2*Sr*um)	Daytime. 2 km above sea level at 975 nm [5, Fig 8.16]
Optical filter bandwidth	1	1	1	nm	
Receiver Electronics					
APD Gain	20	20	20	-	APD/TIA module: Voxtel RDC1-NJAF
Responsivity	1.00	1.00	1.00	A/W	From device test report (measured value)
Transimpedance	44,600	44,600	44,600	ohm	From device test report (nominal value), not used in calculations at present
Excess noise factor	4.3	4.3	4.3		From device sales sheet
Noise equivalent power	2.80E-09	2.80E-09	2.80E-09	W	From device test report
Noise equivalent bandwidth	3.00E+08	3.00E+08	3.00E+08	Hz	This is greater than signal bandwidth, assumes single pole LPF [35, pg 123-124]
Link Budget Summary					
Laser avg. optical power (dBW)	-7.0	-7.0	-7.0	dBW	200 mW average output power EDFA
Transmit optical losses (dB)	-1.5	-1.5	-1.5	dB	Placeholder
Transmit antenna gain (dB)	65.6	65.6	65.6	dBi	Uniform plane wave assumption. G=16/theta^2 [80, Eq 3.78]
Path loss (dB)	-258.2	-258.2	-258.2	dB	Standard free-space path loss equation
Atmpheric loss	-1.0	-1.0	-1.0	dB	MOD/TRAN model
Pointing loss	-3.0	-3.0	-3.0	dB	ADCS three-sigma performance better than HPBW
Receive antenna gain (dB)	115.7	115.7	115.7	dBi	Diffraction limited gain
Receive optics losses	-2.0	-2.0	-2.0	dB	Placeholder
Signal power at detector	-91.4	-91.4	-91.4	dBW	Sum of above terms. Represents average power.
Signal power required for BER=1e-4	-93.7	-91.5	-89.2	dBW	
Margin for BER=1e-4 at 1000 km	**2.4**	**0.2**	**-2.2**	**dB**	Maximum range
Margin for BER=1e-4 at 600 km	**4.6**	**2.4**	**0.0**	**dB**	Nominal range (time average over pass)

Table 2.1: Optical downlink link budget for three rate configurations. Low (PPM-64), medium (PPM-32) and high rate (PPM-16) configurations are presented. All other parameters are matched.

58

ROI surrounding the brightest pixel in the frame. Background subtraction, which reduces bias imparted by upwelling light, is usually performed prior to the center-of-mass calculation. The performance of this aspect of the system has been thoroughly studied in [39].

2.5   Design Summary

The top-level design parameters for the CubeSat lasercom system are presented in Table 2.2. These parameters are a result of the requirements flow-down methodology (Figure 2-1) and a subsequent mapping of prior lasercom techniques onto available COTS components that are also compatible with the extreme SWaP constraints of the application. Although the system architecture resembles other LEO lasercom designs (most notably AeroCube-OCSD and OPALS), it incorporates two novel developments to address implementation gaps that enable implementation on a resource-constrained platform: an optical steering mechanism, and a COTS-inspired rate-scalable laser transmitter.

In the remainder of this thesis these implementation gaps are addressed through surveys of available solutions, down-selection, and finally prototyping and validation. In the end, it is the lasercom system's competitiveness with a comparable RF solution that really matters. Thus, the overall effectiveness of the system will be measured in terms of meeting the design parameters outlined in Table 2.2 as well as in terms of the achieved link efficiency (joules-per-bit).

<div align="center">SYSTEM DESIGN PARAMETERS</div>

Optical Link Parameters		Notes/Rationale
Optical link rate	10 Mbps (threshold) 50 Mbps (stretch)	Uncoded channel rate
Bit error rate	1×10^{-4} BER	Uncoded link
Operational range	$\leq 1000\,\text{km}$	Appropriate for 400 km altitude LEO satellite
Downlink beamwidth	2.1 mrad (FWHM)	Radiometry-driven

Host Spacecraft ADCS Parameters		
Unassisted pointing	$\pm 2.5°, \pm 44\,\text{mrad}$ (3-σ)	Before beacon acq.
Beacon assisted pointing	$\pm 1.0°, \pm 17\,\text{mrad}$ (3-σ)	See Section 2.3.1
Body slew rate	$> 1°\,\text{s}^{-1}$	Ground target tracking

Lasercom Terminal Parameters		
Size	0.5 U	$5\,\text{cm} \times 10\,\text{cm} \times 10\,\text{cm}$
Mass	500 g	
Power	10 W (during TX) 1 W (idle)	Similar to RF solutions
PAT scheme	hybrid open/closed-loop	Using uplink beacon
Beacon detector FOV	$> 5° \times 5°$	Focal plane array
Fine steering range	$> \pm 1.0°$	Driven by beacon-assisted coarse stage performance
Fine steering resolution	0.21 mrad	FSM driven open loop
Fine steering performance	$\pm 1.05\,\text{mrad}$ (3-σ)	Absolute performance using beacon knowledge

Ground Segment Parameters		
Receive aperture	$\leq 30\,\text{cm}$	COTS telescope
Mass	50 kg	For portability
Coarse pointing	open-loop	Based on TLE/ephemeris
Fine pointing	closed-loop	Acq. camera driving FSM
Detector	APD, PMT, etc.	COTS unit desired
Uplink beacon	850 nm, 10 W	

<div align="center">Table 2.2: High-level design parameters for the lasercom system</div>

Chapter 3

Detailed Design

In this chapter, we present the results of our detailed trade study on system design and identify solutions for the previously identified implementatino gaps: the compact laser transmitter and the optical fine steering mechanism (Figure 3-1). We also discuss other supporting elements, notably the high-speed electronics and beacon tracking detector, as they influence the design process for the laser transmitter and the FSM. The design of the pointing, acquisition and tracking (PAT) algorithms are outside of the scope of this thesis, but reasonable design choices (e.g., choice of beacon detector bandwidth and FSM bandwidth) are described here to frame future work on these algorithms.
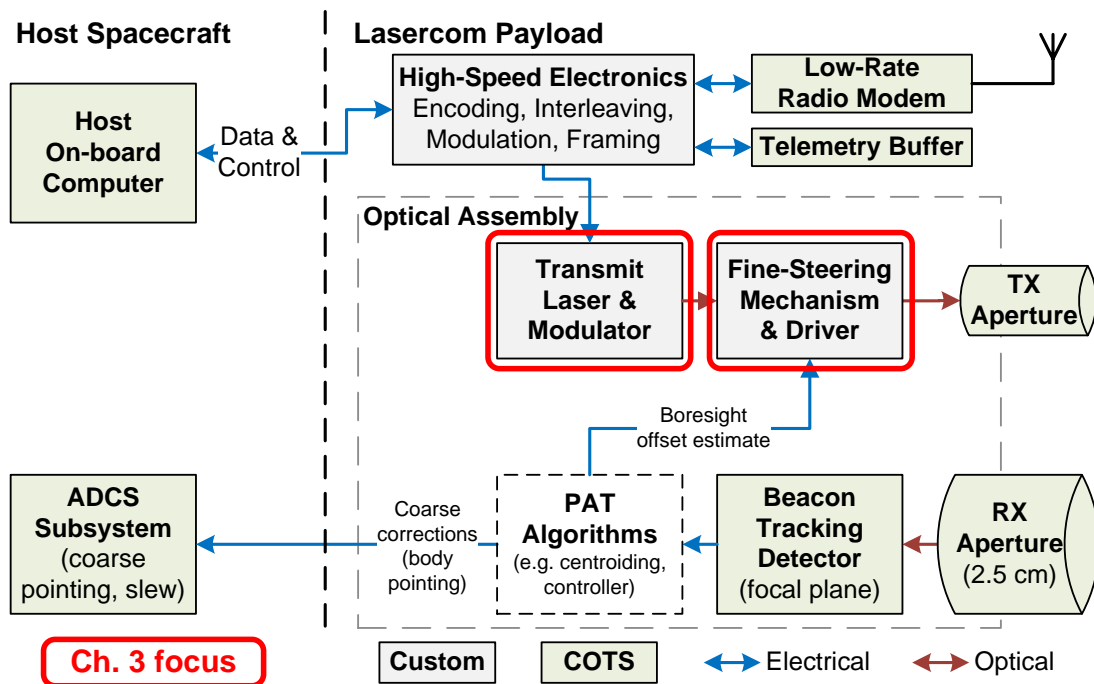
Figure 3-1: Functional block diagram for space segment design showing partitioning of functions between the lasercom terminal and the host spacecraft. Components addressed in this chapter are highlighted in red.

3.1 Transmitter Trade Study

Section 2.4 presented link budgets based on a MOPA transmitter architecture. Early in the project, it was not clear that this specific architecture was appropriate for the CubeSat transmitter application. In this section, we present the trade study that led to the selection of this architecture. We assume an 8 W power budget for the transmitter, which is the largest allocation from the total 10 W power budget for the lasercom terminal.

Preliminary system link budgets (Section 2.4) indicated that the CubeSat optical transmitter would need to produce approximately 1 W of optical output power to close the link at the required bit error rate (1×10^{-4}). This figure was largely a result of the downlink beamwidth (derived from system pointing capability), the link range (< 1000 km) and the sensitivity of the ground receiver (1000 photons-per-bit, appropriate for COTS detectors such as avalanche photodiode / transimpedance amp modules).

A survey of COTS optoelectronics components yielded two broad categories of 1 W-class optical sources: high power laser diodes (HPLD), such as a "pump" laser at 980 nm, and a master-oscillator power amplifier (MOPA) designs incorporating a fiber amplifier at either 1000 nm or 1550 nm. We assessed the effectiveness of each of these configurations for our system by considering the end-to-end link performance. This performance analysis incorporated realistic transmitter assumptions (e.g., modulation type) and receiver parameters (e.g., suitable detector technologies for a given transmitter wavelength). System parameters were matched where possible, but the resulting transmitter capabilities did not allow for all system parameters to be matched. Table 3.1 enumerates the important differences between the two configurations.

Table 3.1: Summary of the differences between the two configurations used in the transmitter trade study.

	HPLD	MOPA
Wavelength	980 nm	1550 nm
Transmit power (avg)	500 mW	200 mW
Modulation	on-off-keying (OOK)	PPM-16
Receiver bandwidth	Matched to modulation bandwidth	
Detector	Si APD/TIA	InGaAs APD/TIA
Performance limiter	Modulation bandwidth of HPLD	Wall-plug power

3.1.1 High-Power Laser Diode (HPLD) Transmitter

The HPLD configuration (Figure 3-2) consists of a directly modulated high-power laser, such as a 980 nm "pump" laser diode, which are available in convenient single mode fiber-coupled butterfly packages. The electrical-to-optical (EO) conversion efficiency of these lasers is excellent, typically greater than 30% with some devices

exceeding 50% efficiency. Operation at 980 nm is also advantageous from a receiver perspective as silicon detectors are near their peak responsivity $(A\,W^{-1})$[1].
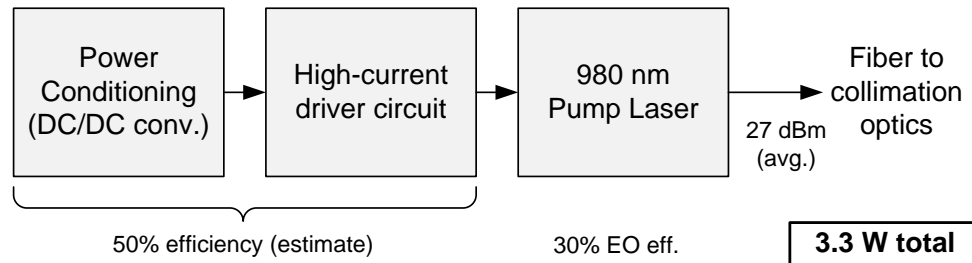
Figure 3-2: HPLD configuration block diagram show conservative power consumption and efficiency estimates for each component. Although the laser diode itself offers well-understood efficiency ratings that can be pulled from datasheets, the associated high-rate high-current driver circuit is less well understood.

The principle disadvantage of the HPLD stems from the limited modulation bandwidth (roughly 100 MHz, but highly depedent on laser diode packaging) and associated driver circuitry, which must modulate large drive of currents. Assuming on-off-keying (OOK), which minimizes modulation bandwidth relative to data rate, and a typical pump diode efficiency $(\eta = 0.6\,W\,A^{-1})$, the driver circuit would need to switch over 1.5 A at 10 MHz rates. This approach is feasible, and is used in some systems (e.g. laser video projection systems), but is fundamentally limited by the package parasitics of the laser. Most high-power laser diodes come in "butterfly" style packages and are designed to run in continuous power mode, the package lead inductances make high rate modulation challenging[2]. Aside from the modulation rate restrictions, this configuration could be well within power budget: 3.3 W estimated of 8 W budget and could operate with an estimated "wall-plug" efficiency (end-to-end, electrical to optical) of 15%.

3.1.2   Master Oscillator Power Amplifier Transmitter

The master oscillator power amplifier (MOPA) configuration (Figure 3-3) relies on an average-power-limited fiber amplifier such as an Erbium-doped fiber amplifier (EDFA) [89, 90, 27]. Average-power-limited amplification allows the system to take advantage of low duty-cycle waveforms which result in high peak-to-average ratios such as pulse position modulation (PPM) (see, e.g., [89, 36])[3]. The widespread use

---

[1]We note that in a electronics (thermal) noise limited receiver it is responsivity, not quantum efficiency, that is the best figure of merit for a detector. Appendix A describes the receiver performance analysis approach in detail.

[2]We note that it might be possible to repackage, or de-package, one of these lasers to mitigate these parasitics but that would go aheads the COTS-based design philosophy. Fiber-coupling the optical output of a repackaged device would also be an unwanted complexity.

[3]High peak-to-average power waveforms are advantageous on direct detection receiver-noise-limited systems such as the APD-based receiver assumed in this design.

of fiber amplifiers in the commercial telecommunications industry is supported by a wide selection of vendors offering high-reliability components.

Aerospace-grade fiber amplifiers are also available from a variety of sources, however, we were unable to identify any space-rated solutions which even remotely met the SWaP and cost constraints for this project. Although not space-rated, commercial-grade fiber amplifiers offer lower SWaP and cost profiles and are often subjected to rigorous qualification procedures (e.g., Telcordia GR-468 qualification [91]).
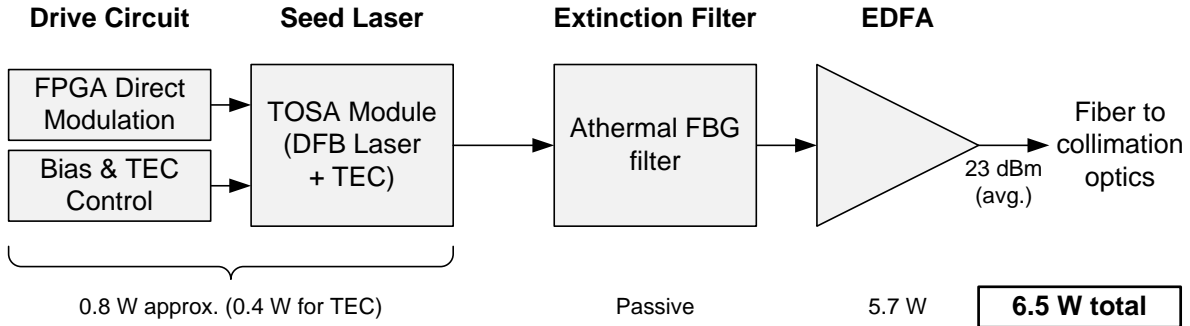
Figure 3-3: MOPA configuration diagram showing the power consumption of major components. The FPGA power consumption accounts only for transmitter-specific portions of the device which is shared with other lasercom terminal functions (e.g., beacon camera interface). The power ratings for the seed laser and associated bias and TEC controllers, as well as the EDFA, are based on vendor specifications.

We considered both Yttrium-doped fiber amplifiers (YDFA, 1050 nm) and Erbium-doped fiber amplifiers (EDFA, 1550 nm) for use in this application. Although YDFAs can provide roughly twice the wall-plug efficiency of EDFAs, these efficiency benefits are hard to realize at the low ($< 1\,\text{W}$) power levels [36, 92]. Additionally, YDFAs are less eye-safe and are generally much less available than EDFAs, making them less suitable for the COTS-based design approach. For the trade study, we baselined a 200 mW "MSA" (multi-source agreement) form-factor ($9\,\text{cm} \times 7\,\text{cm} \times 1.5\,\text{cm}$) EDFA that is compatible with the volume constraints of CubeSats. The lower output power of the MOPA (relative to the HPLD) is roughly balanced by the link margin gained from moving to PPM from OOK modulation on the average-power-limited EDFA[4].

Aside from the amplifier, the modulator is typically a large power consumer for low-SWaP MOPA designs. For PPM waveforms, this modulator must provide high extinction ratios (ER) in order to obtain high peak-to-average power ratios from the average-power-limited fiber amplifier (e.g. for PPM-128, ER $> 36\,\text{dB}$ [93]). To avoid the power penalty associated with an external modulator, a direct modulation approach was selected. The transmitter digital electronics (an FPGA) directly modulate the seed laser with the communication waveform. Only $\sim 10\,\text{dB}$ of ER can be expected from direct moduation if the laser is kept above its threshold current, which is necessary for wide-band modulation [6, 94, 95, 96, 97]. To further improve ER,

---

[4]It is important to note that the same benefit is hard to realize with the HPLD due to its limited modulation bandwidth. Migrating from OOK to PPM requires bandwidth expansion.

the laser's adiabatic frequency chirp [6] is used in conjunction with a narrow band-pass filter to perform frequency modulation (FM) to amplitude modulation (AM) conversion. Adiabatic frequency chirp is the laser's wavelength response to short-term (< 10 ns changes in charge carrier density or forward current (Figure 3-4). This technique has been demonstrated in both fiber [94, 95] and free-space [96, 97, 98] applications.
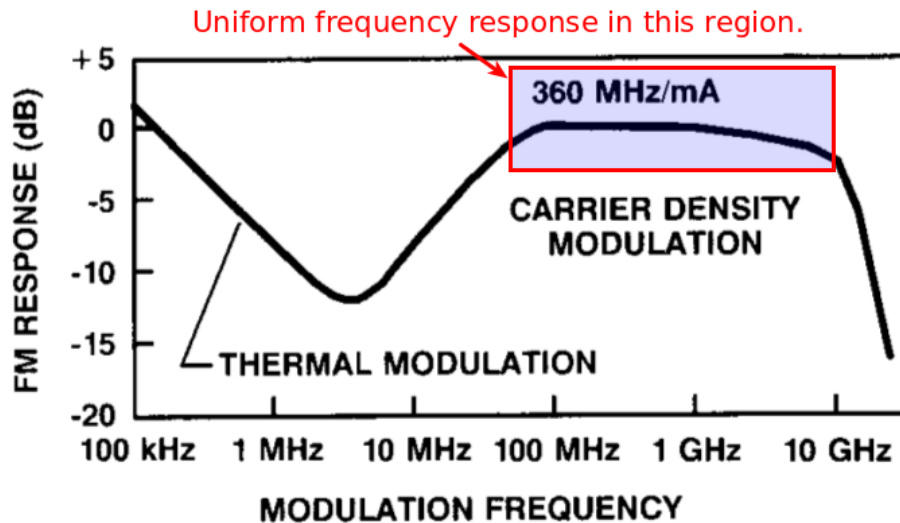
Figure 3-4: Results from [6] show a distributed feedback laser's frequency modulation (FM) response with respect to current modulation frequency. Above 100 MHz the FM response is uniform with frequency which allows deterministic mapping of drive current to laser wavelength.

The MOPA design is estimated to consume 6.5 W yielding a wall-plug efficiency of approximately 3%, driven largely by the power efficiency of the COTS EDFA. This is much lower than the HPLD design, but the MOPA is capable of producing higher fidelity waveforms at much faster modulation rates ($\gg 1$ GHz).

3.1.3 Selection Criteria

Table 3.2 gives a high-level comparison for the two transmitter architectures. Both configurations showed > 3 dB link margin at 10 Mbps. From a size, weight and power perspective, the HPLD is the clear winner but the design suffers from fundamental modulation bandwidth restrictions. Presently, our system data rates are primarily limited by available CubeSat power and the relatively broad transmit beamwidth (2.1 mrad FWHM) derived from CubeSat pointing capabilities. Pointing performance should improve in the coming years which will allow for narrower transmit beams and thus faster data rates. Although the MOPA has higher SWaP it remains within budget and can be constructed using readily available COTS components while providing excellent rate-scalability to support future systems with better pointing capability.

Table 3.2: Comparison of transmitter architectures

Parameter	HPLD	MOPA
Wavelength	980 nm	1550 nm
Size	$5\,\text{cm} \times 5\,\text{cm} \times 1\,\text{cm}$	$10\,\text{cm} \times 10\,\text{cm} \times 3\,\text{cm}$
Mass	100 g	250 g
Power (8 W budget)*	3.3 W	6.5 W
Max Modulation Bandwidth	$< 100\,\text{MHz}$ (package limits**)	$> 1\,\text{GHz}$
Peak-to-average Limit	Low (typ. < 10)	High (> 16)
Spectral Quality	Poor ($> 1\,\text{nm}$)	Excellent
Notable Risks	Driver circuit design Spectral quality	Wall-plug power Achieving high ER Component count

* Power estimates includes thermal stabilization for MOPA, but not for HPLD.
** Package parasitics (e.g., lead inductance) place practical limits on bandwidth.

3.1.4 Validation Criteria

The MOPA transmitter architecture is unquestionably more complex than the HPLD approach. Given that the MOPA is a dominant term in the system power budget, the power consumption of the prototype is a focus of initial validation activities. The extinction ratio of the seed laser, which is critical for achieving high peak-to-average power ratios, is also measured. The fidelity of the transmitted optical waveforms is also measured to ensure that pulse energy is well-confined and not spreading to adjacent time slots. Finally, the overall robustness of the design to a thermal fluctuations must be considered since the system operates at low duty cycles during short ground station passes (e.g., $\approx 5\,\text{min}$ every $90\,\text{min}$ orbit). It is unlikely that the design will be able to operate in thermal steady-state due to host power limitations.

3.2 Fine Steering Mechanism Selection

The beam divergence analysis presented in Section 2.3.1 showed that a gap exists between CubeSat body pointing capabilities and the pointing performance needed to support a 2.1 mrad (FWMH) downlink beam. We bridge this gap by adding a fine control stage that uses improved attitude knowledge from a beacon camera and improved actuation from a fine-steering mechanism.

Determination of a suitable range, resolution and bandwidth requirements for the beacon detector and the fine-steering mechanism were primarily driven by the capabilities of the coarse stage and COTS part availability. Figure 3-5 shows how field of view of the beacon camera compares to the field of regard (i.e., the steering range) of the FSM compare to each other. The steering range of the FSM "underfills" the camera field of view because analysis showed that the host's coarse pointing performance was sensing-limited prior to beacon acquisition [99]. Once the beacon

has been acquired, this knowledge allows coarse pointing improve so that total error can be reduced to within the field of regard of the FSM. The ability to use a smaller steering range device opens up the space of COTS options and also leads to improved resolution[5].
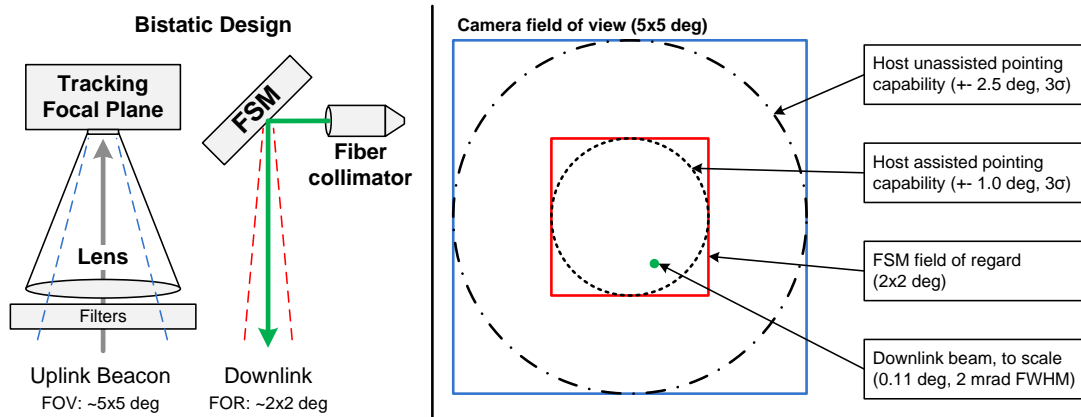
Figure 3-5: Diagram of angular field of beacon acquisition camera and fine steering mechanism, along with coarse stage (host ADCS) body pointing requirement.

We have selected a 2.5 cm diameter aperture for the uplink signal (driven by photon collection needs of the beacon detector [39]) and a much smaller (≈ 1 mm diameter) downlink aperture which is sufficient for achieving the desired 2.1 mrad beamwidth[6]. The uplink beacon detector functionality can be provided by a standard COTS "C-mount" lens and focal plane array. The downlink fine-steering architecture is a "gimbaled flat" design consisting of a fiber beam coupler (which establishes the desired beam divergence) followed by a fast-steering mirror. The requirements for the fast-steering mirror are summarized in Table 3.3.

3.2.1   COTS Fine Steering Mirrors

Three distinct classes of COTS fine steering solutions were considered for use in this project (Figure 3-6). These can be grouped by their actuation type: mechanical, piezoelectric, and microelectromechanical (MEMS) devices.

Conventional mechanical FSMs, which typically use voice coils for actuation, were eliminated early in the project due to their inability to meet size constraints. Many devices in this category, such as the Newport FSM-300, provide large mirrors (e.g. 25.4 mm) which are unnecessary for our application. These products also have large moving masses which make them more susceptible to shock and vibration damage[7].

---

[5]Single stage physical actuators typically have a limited range-to-resolution ratio. As a general design rule, and as corroborated by the devices considered in this study, this ratio is rarely larger than 10,000:1.

[6]The diffraction limited aperture size needed to produce a 2.1 mrad FWHM beam at 1550 nm is roughly 0.7 mm.

[7]These masses may be large enough to cause significant reaction forces on the spacecraft. This is certainly an unwanted side effect of the lasercom design that would be levied on the host CubeSat.

Table 3.3: Fine steering mechanism requirements & design goals

Parameter	Value	Justification / Driver
Actuation Type	2-axis (tip/tilt)	No space for two single-axis devices
Field of regard	$> \pm 17.4\,\mathrm{mrad}$	Coarse-stage pointing perf.
Accuracy	$\pm 0.21\,\mathrm{mrad}$ (3-σ)	1/10th of downlink beamwidth
Bandwidth	$> 10\,\mathrm{Hz}$	Max beacon detector readout rate
Diameter	$> 2\,\mathrm{mm}$	Mechanical alignment (Section 5.1.1)
Size goal	$< 2\,\mathrm{cm} \times 2\,\mathrm{cm} \times 2\,\mathrm{cm}$	Including driver electronics
Mass goal	$< 100\,\mathrm{g}$	Including driver electronics
Power goal	$< 100\,\mathrm{mW}$	While steering at full bandwidth

Example voicecoil FSM
[Newport FSM-200]

Example piezo FSM
[PI S-334]

Example MEMS FSM
[Mirrorcle Tech 3mm]
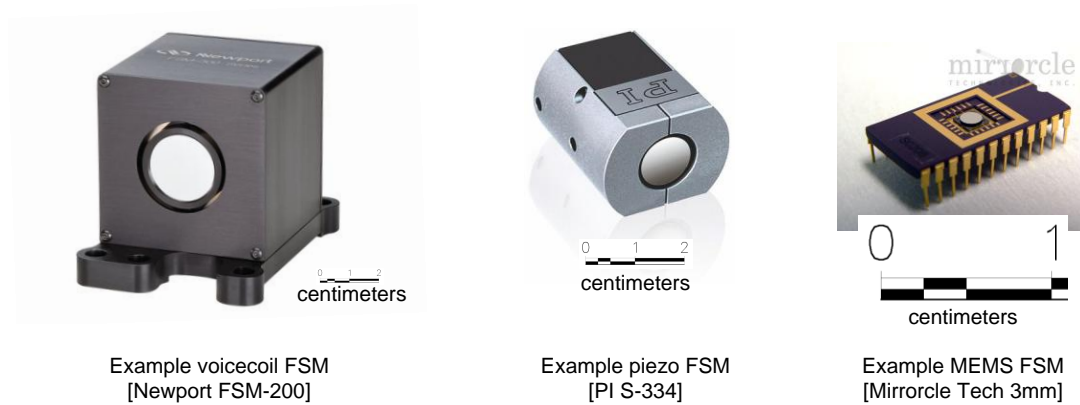
Figure 3-6: Photographs of fine-steering mirror solutions considered in this trade study: voicecoil, piezo and MEMS type devices with approximate scale bars.

Voice coils, which are current-driven, also tend to have high power consumption (some manufacturers quote figures $> 10\,\mathrm{W}$ [100]). This also exceeds our requirements. Finally, our prior experiences with designing and qualifying mechanical actuators for CubeSats has given us a healthy respect for amount of engineering time required to qualify a mechanical actuator [101].

Piezoelectric mirrors, such as the Physik Instrumente (PI) S-334, were also considered for this application. The PI S-334 offers sufficient steering range ($\pm 5\,\mathrm{mrad}$) and resolution ($\pm 5\,\mathrm{\mu rad}$ open-loop) for our application. Unfortunately, the underlying piezoelectric actuation technology exhibits strong non-linearity and hysteresis which requires the use of a complex closed-loop controller. Although the S-334 mirror ($4\,\mathrm{cm} \times 3.3\,\mathrm{cm} \times 2.5\,\mathrm{cm}$, $65\,\mathrm{g}$) fits roughly within our SWaP constraints, the smallest available controller, the PI E-616, does not ($19\,\mathrm{cm} \times 13\,\mathrm{cm} \times 10\,\mathrm{cm}$, $950\,\mathrm{g}$, $30\,\mathrm{W}$). It is likely that this controller could be miniaturized for use in our application, however, this too would require a significant engineering effort given that the design details of the COTS driver and underlying piezo actuator parameters are vendor-proprietary.

The third class of devices that were considered were MEMS tip-tilt mirrors. This category can be further divided into electrostatic and electromagnetic actuation units.

The Texas Instruments TALP1000B is an example of a electromagnetically actuated MEMS FSM. This FSM and driver circuit meet our SWaP requirements as described in [102]. Unfortunately this device is no longer in production, thus it was eliminated from consideration.

The second type of MEMS FSMs are electrostatically actuated. A wide variety of electrostatic MEMS FSMs are available from Mirrorcle Technology Inc (MTI). These chip-scale $(0.5\,\text{cm} \times 0.5\,\text{cm} \times 0.1\,\text{cm})$ devices have steering ranges exceeding $\pm 20\,\text{mrad}$ and are available with low-SWaP driver boards. The mirrors options range from $1\,\text{mm}$ to $6\,\text{mm}$ in diameter, large enough for our application. These devices do not incorporate built-in position sensors (which could be used for closed-loop control) but have well-behaved transfer functions that allow most users to operate them in an open-loop configuration (Figure 3-7).
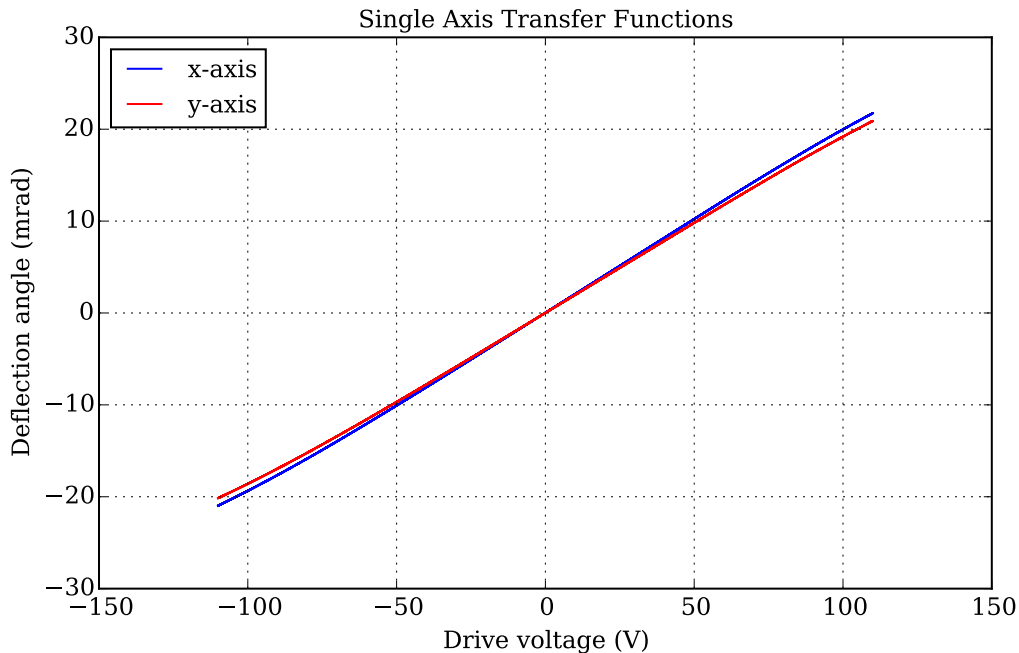
Figure 3-7: Example voltage-to-angle transfer function for an MTI MEMS device.

3.2.2   Selection Criteria

Table 3.4 compares the specifications of some of the FSM devices considered for this project. Only the MEMS devices, along with the required driver, were able to meet the SWaP requirements for this application. Both the electromechanical and piezo designs offer superior pointing performance, but the vendor-proprietary driver designs are far to large and complex to miniaturize for this application. A MEMS unit with a $2.4\,\text{mm}$ diameter mirror and a $\pm 1.25°$ steering range were selected for the design from MTI's offerings. None of the products considered have known space heritage, but MTI has indicated that their MEMS FSM products have been used successfully

69

in both vacuum and cryogenic environments [103]. Other MEMS devices, some with similar actuator technology, have undergone space qualification [49, 51, 52, 50, 53].

Table 3.4: Specification comparison for typical fine steering mechanism solutions.

	Voice coil	Piezo	MEMS
Product name	Newport FSM-300	PI S-334	MTI 13L2.2
FSM Size	$205\,\mathrm{cm}^3$	$300\,\mathrm{cm}^3$	$0.5\,\mathrm{cm}^3$
FSM Mass	$450\,\mathrm{g}$	$250\,\mathrm{g}$	$10\,\mathrm{g}$
Range	$\pm 26.2\,\mathrm{mrad}$	$\pm 50\,\mathrm{mrad}$	$\pm 21.8\,\mathrm{mrad}$
Accuracy (3-σ)	$< 3\,\mathrm{\mu rad}$	$5\,\mathrm{\mu rad}$	$100\,\mathrm{\mu rad}$*
Driver Type	Closed loop	Closed loop	Open loop
Driver Size	$5100\,\mathrm{cm}^3$	$2470\,\mathrm{cm}^3$	$28.8\,\mathrm{cm}^3$
Driver Mass	$2.5\,\mathrm{kg}$	$950\,\mathrm{g}$	$20\,\mathrm{g}$
Power	$3.3\,\mathrm{W}$	$6.5\,\mathrm{W}$	$< 100\,\mathrm{mW}$
Bandwidth	$580\,\mathrm{Hz}$	$50\,\mathrm{Hz}$	$500\,\mathrm{Hz}$
Notable Risks	Power consumption	Driver complexity	Open-loop performance

* Estimated from vendor-provided repeatability data in device test report.

3.2.3 Validation Criteria

Vendor-provided data for the MEMS devices shows that they have a nearly linear transfer function (i.e., voltage to displacement angle) under standard room conditions. Additionally these data sets also indicate that they offer angular position repeatability better than 100 µrad which meets the fine stage accuracy requirement. Nevertheless, the open-loop mode of operation of these devices requires further characterization as the vendor provides no specific guarantees for performance across temperature. Preliminary test results conducted by other groups indicate that the devices had slight (approximately 1% of full range) thermal-induced angular errors [104]. Validation of device performance across operating temperature range will be described in detail in Chapter 4.

3.3 Resource Budgets

3.3.1 Size Budget: Terminal Physical Layout

Figure 3-8 shows a notional physical layout for the lasercom terminal design. This layout has "side looking" apertures which allows the terminal to be installed anywhere within a 3U CubeSat stack. The end faces of 3U CubeSats are frequently used for payload sensors such as images, so we avoid occupying this potentially valuable real estate.

The largest and highest power dissipation unit within the design is the fiber amplifier module. Single mode fibers are used to deliver the transmit signal from the amplifier module to the transmit collimator. A small optics bench serves as a rigid mount point for the uplink aperture (likely a COTS camera lens) and the transmit collimator and FSM. Alignment errors between the transmit and receive optical paths will be calibrated on-orbit using raster-scan downlink steering in conjunction with power measurement at the ground station. A formal thermal analysis of the optics bench is left for future work (Section 5.2.3).
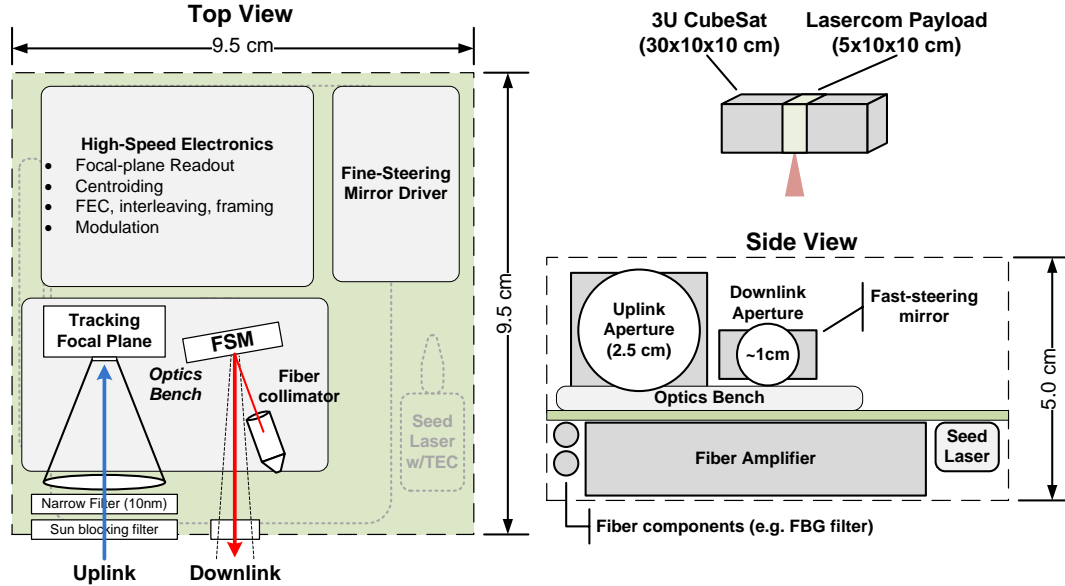
Figure 3-8: Physical layout of lasercom terminal design showing parts placement within the target $10\,\text{cm} \times 10\,\text{cm} \times 5\,\text{cm}$ volume envelope.

3.3.2 Mass Budget

A mass budget for the lasercom terminal is provided in Table 3.5. The budget is high level due to the fact that the flight packaging design is still in progress. Major system components that have been used in the validation activities have been weighed to confirm vendor specifications. Miniaturization, packaging and integration concerns are discussed in Section 5.1.1.

3.3.3 Power Budget

A power budget for the lasercom payload design is provided in Table 3.6. Analysis of power consumption assumed a variety of different operating modes, including idle (i.e., between communication passes), acquisition (i.e., during initial beacon search but before comm) and transmit-active communications. Each mode consists of a distinct component duty cycle assumptions. For the sake of brevity, only the transmit active mode is shown in the power budget since it is by far the most demanding. Idle

Table 3.5: High-level mass budget with current best estimates.

Component	Mass (g)	Notes
High-speed Electronics	60	PCB, FPGA, memory
Fine-steering mechanism	20	Including driver circuit
Structural mounts	100	Est. for optics bench
Transmitter		
Seed laser	20	Measured value
Extinction filter	20	Measured value
EDFA	150	Measured value
TX collimator	10	Measured value
Fiber service loops, splices	20	Estimated value
Beacon Receiver		
Lens and filter assembly	100	Estimated
Focal plane array	50	Estimated
Total	550 g	600 g budget
Margin	+10%	

mode, which will be used the vast majority of the time, will be designed to minimize quiescent power consumption.

Table 3.6: Power budget for lasercom terminal based on current best estimates. Only shows the transmitter-active mode since this is the most stressing for the system.

Component	Power (W)	Duty cycle	P_avg	Notes
Focal plane array	2.00	100%	2.00	
PAT Processor	0.25	100%	0.25	Separate PAT processor?
Fast-steering mirror + driver	0.25	100%	0.25	
High-Speed Electronics				
FEC encoder	0.25	0%	0.00	Microcontroller, offline encoding
Non-vol telem. buffer (SSR)	0.25	100%	0.25	SD card or similar
Modulator/framer	1.00	100%	1.00	Spartan-6 FPGA LX45
Laser transmitter				
EDFA	5.70	100%	4.10	Measured in lab
Seed laser driver	0.25	100%	0.25	
Seed laser TEC	0.25	100%	0.25	
Radio Modem				
Receive only	0.10	95%	0.10	Astrodev Lithium-1 values
Transmit/receive	1.50	5%	0.08	Astrodev Lithium-1 values
Mode Total (W)			8.52	10.00 W budgeted
Power Margin (%)			+15%	

3.4 Summary

In this chapter, we have completed down-selections and identified "existence proofs" for two major components of the lasercom terminal design: the architecture for the laser transmitter and the selection of a fine steering mechanism. In the next chapter, these components are experimentally validated to ensure that they meet performance

requirements. End-to-end communication link functionality, which validates key link budget assumptions (e.g., detector sensitivity), are also discussed.

Chapter 4

Design Validation

In this chapter, we present experimental results that validate the system design choices and analyses that were presented in Chapter 3. A transmitter prototype was constructed primarily with path-to-flight components. The transmitter was used in conjunction with a loopback receiver, a simplified version of the ground station receiver, to perform fiber-coupled end-to-end communications experiments. We also designed and implemented a test rig for characterizing the fine steering mechanism. Finally, in this chapter we report on environmental test results that have targeted portions of the system with known or suspected thermal dependencies.

4.1 Key Performance Metrics

Three key performance metrics are established in this chapter. First, we validate the power consumption of the transmitter which is the dominant term in the overall lasercom terminal power budget (8 W of a 10 W total budget). These measurements include the EDFA as well as the control circuits needed to stabilize and align the seed laser. Second, we confirm the optical sensitivity of the flight APD/TIA detector. The noise floor of this device is presently the limiting factor on link data rate, thus, it is important to validate the vendor specification. Third, we characterize the performance of the MEMS fine-steering mechanism. The system design uses this device in an open-loop manner so it is essential to collect data on its input voltage-to-angle transfer function as well as overall position repeatability. We also present some preliminary environmental test results that build confidence that the design is adequate for the expected operating temperature range at LEO (0 °C to 40 °C inside CubeSat chassis).

4.2 Transmitter Prototyping & Validation

Table 4.1 summarizes the detailed design parameters for the transmitter subsystem of the lasercom terminal. The optical signal power and modulation parameters were a result of the transmitter architecture tradestudy (Section 3.1), the link budget analysis Section 2.4.1, and a survey of vendor component offerings (most notably,

compact EDFA modules). Power consumption is the most significant constraint facing the transmitter design which motivates validation of vendor-provided specifications.

4.2.1 High-speed Modulator

The lasercom terminal includes a field-programmable gate array (FPGA) to generate the communications waveform. FPGAs and other custom logic solutions (e.g., application specific integrated circuits, ASICs) are the most practical way to generate low-jitter, deterministic digital waveforms at high rates ($> 100\,\mathrm{MHz}$). For initial laboratory testing, we configure a Xilinx Spartan 6 evaluation board to produce pulse position modulation (PPM) waveforms. The PPM slot rate ($f_{slot} = 40$ or 200 MHz), the modulation order ($2 \leq M \leq 2^{16}$), and the number of guard slots ($0 \leq G \leq 2^8$) can be reconfigured using the attached control computer (Figure 4-1).

FGPA-generated PPM Modulation:
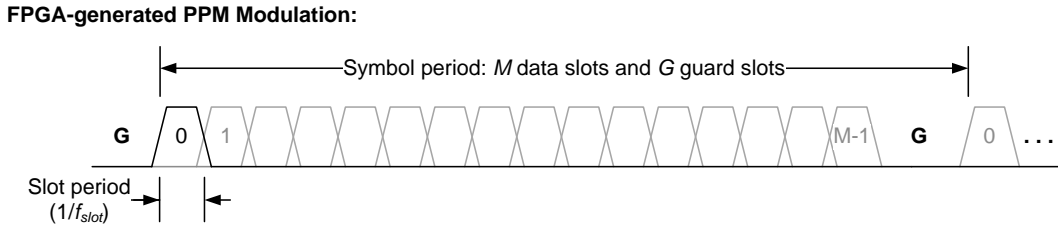
Figure 4-1: Diagram of the digital waveform produced by the FPGA-based PPM modulator. Configurable parameters include f_{slot}, M, and G.

A general purpose input/output (I/O) pin, configured as a $2.5\,\mathrm{V}$ single-ended output, is used to directly modulate the seed laser. The seed laser interface consists of an impedance matching network and an AC-coupling capacitor. Unlike many other much higher rate FPGA modulators, we avoid the use of power-hungry Gigabit transcievers (e.g. RocketIO) in this design. Instead, the design relies on the low-power serializer-deserializer (SERDES) functionality built into the FPGA's I/O buffers. The

Table 4.1: Design parameters for the MOPA transmitter. Optical signal parameters are derived from the link budget analyses in Section 2.4.1.

Parameter	Value	Justification / Driver
Optical output power	$> 200\,\mathrm{mW}$ avg	Link budget BER target
Modulation type	PPM, $M = [8 - 128]$	Enables high peak power levels
Modulation BW	$> 1\,\mathrm{GHz}$ desired	Able to scale to higher rates
Wavelength stability	$\pm 1\,\mathrm{nm}$	Ground receiver filter
Input power	$< 8\,\mathrm{W}$	Transmitter portion of terminal
Size goal	$< 10\,\mathrm{cm} \times 10\,\mathrm{cm} \times 3\,\mathrm{cm}$	Transmitter portion of terminal
Mass goal	$< 300\,\mathrm{g}$	Transmitter portion of terminal
Operating temp. range	$0\,°\mathrm{C}$ to $40\,°\mathrm{C}$	Typ. CubeSat values (internal)

SERDES allow operation at up to 600 MHz while maintaining much lower FPGA fabric clock rates.

4.2.2 Seed Laser Selection Criteria

The primary selection criteria for the seed laser was the power consumption of the integrated thermoelectric cooler (TEC). Accurate temperature control is necessary to stabilize the laser wavelength, and on many lasers the TEC requires significant amounts of power (> 1 W). The size and mechanical mount style were secondary selection criteria. Transmitter optical sub-assemblies (TOSA) were identified as a good match for our application: they have low power TECs (< 0.4 W) and are available in very compact fiber-coupled packages (20 mm × 8 mm × 5 mm, Figure 4-2). The TOSA selected for this design has 6 dBm CW output power in the 1550 nm C-band.
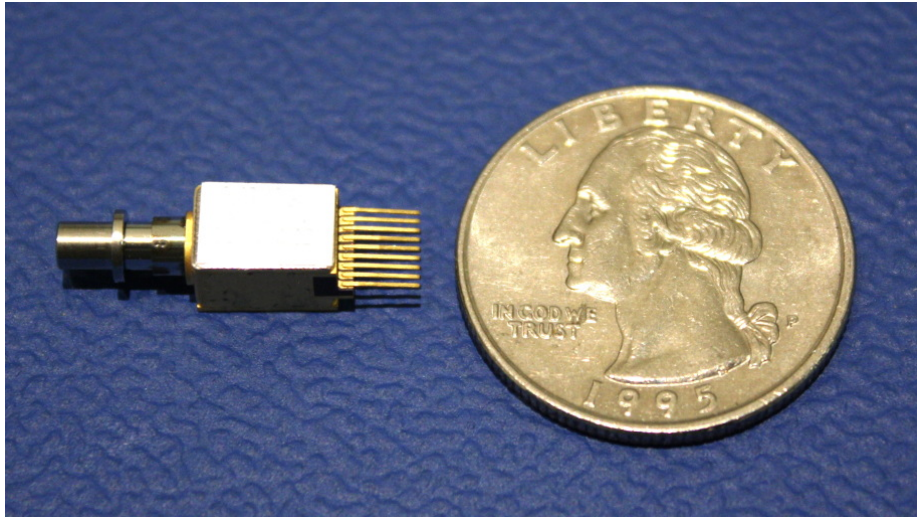
Figure 4-2: A transmitter optical sub-assembly (TOSA) was select for use as a seed laser because of its compact size and low TEC power requirements.

4.2.3 Seed Laser: Wavelength Tuning

We use an automated testbed (Figure 4-3) consisting of a laser diode controller, a wavemeter and an optical spectrum analyzer are used to characterize the wavelength tuning parameters of the seed laser (Figure 4-4). These tuning parameters form the basis for frequency-aligning the laser with the passband of the extinction ratio filter (Section 4.2.5, and [27, 105, 89]). The approximate tuning characteristics for a representative device were $\Delta\lambda/\Delta T = -11$ GHz/°C and $\Delta\lambda/\Delta i_{DC} = -0.45$ GHz/mA (see, e.g., [27, 105])[1]. We obtain these tuning coefficients by least-squares fitting a linear model to the measured data.

---

[1]When describing wavelength tuning and optical filtering, we tend to use wavelengths (e.g., nanometers) and frequencies (e.g., gigahertz) interchangeably. At the 1550 nm operating wavelength of this design 1 nm of wavelength shift equates to approximately 125 GHz of frequency shift.
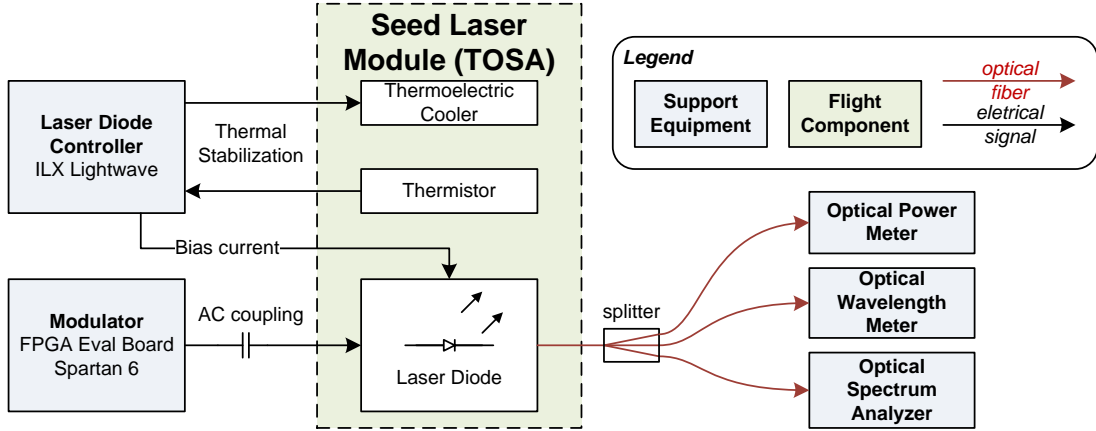
Figure 4-3: Experimental configuration used to characterize the seed laser. A commercial laser diode controller provides DC bias current and temperature control, while the FPGA provides modulation current. An optical wavelength meter and spectrum analyzer were used to monitor the laser output.

Although undesirable in most TOSA applications (e.g., WDM systems), we use the laser's AC wavelength "chirp" ($\Delta\lambda/\Delta i_{AC}$) in our design. The wavelength chirp is used to move the seed laser into and out of the passband of the extinction ratio filter [106, 94, 95, 27, 96, 97, 98]. To measure this aspect of the laser, the FPGA was configured to modulate the seed laser with a PPM-16 waveform with DC bias set above threshold. Observation of the seed laser output optical spectra with an optical spectrum analyzer showed two distinct power peaks corresponding to the "space" and "mark" wavelengths yielding $\Delta\lambda \approx 81\,\mathrm{pm}$ (10 GHz). When generating a PPM-16 waveform at $f_{slot} = 200\,\mathrm{MHz}$, the FPGA is able to deliver $50\,\mathrm{mA}$ of drive current into the seed laser. These two measurements imply an AC tuning coefficient of $\Delta\lambda/\Delta i_{AC} = 0.20\,\mathrm{GHz/mA}$ for a representative device.

The AC wavelength chirp ($\Delta\lambda/\Delta i_{AC}$) was also measured at a lower slot rate $f_{slot} = 40\,\mathrm{MHz}$. This lower slot rate was originally proposed to support lower channel rates and to enable more aggressive low-pass filtering in the receiver electronics. Unfortunately, at this lower slot rate $\Delta\lambda/\Delta i_{AC}$ degrades to approximately $0.10\,\mathrm{GHz/mA}$ which reduces the effectiveness of the FM-to-AM conversion process since the bandpass filter has a finite transition slope (Section 4.2.5). We hypothesize that the AC chirp degradation is due to proximity of f_{slot} to the laser's thermal chirp crossover point [6]. This discovery prompted us to move forward with a design that uses a fixed slot rate of $200\,\mathrm{MHz}$ and to add an additional high-order modulation mode (PPM-128) to provide support for the lower data rates. Using a fixed slot rate also allows the ground station receiver to use a single matched filter (i.e., a filter with an electrical bandwidth matched to slot rate, commonly $0.8 \cdot f_{slot}$) for all system data rates.
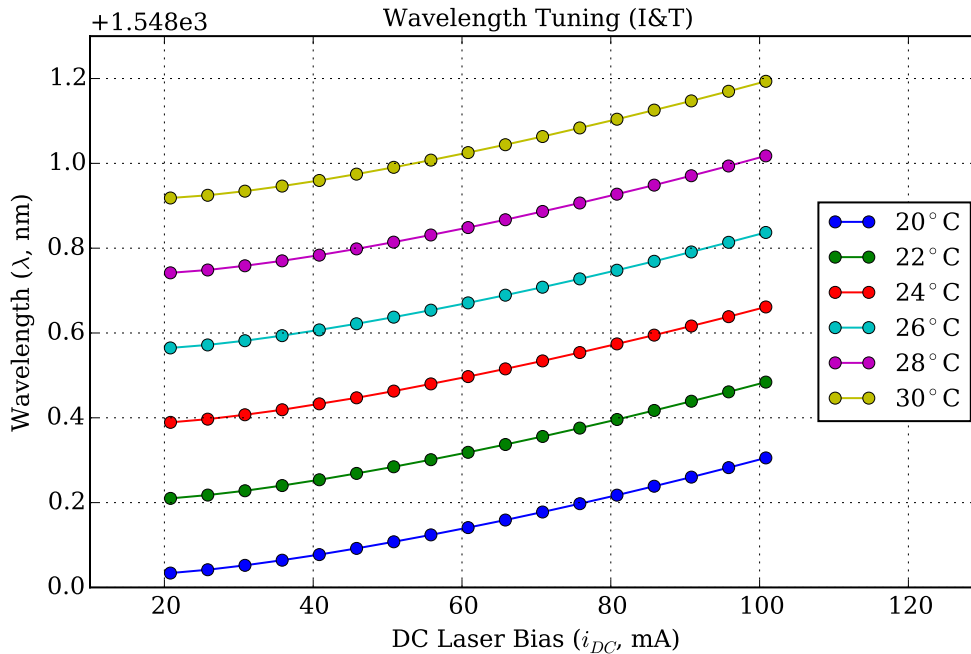
Figure 4-4: Seed laser temperature and DC current wavelength tuning relationships are nearly linear which allows deterministic and repeatable tuning.

4.2.4 Seed Laser: Thermal Stabilization Power Consumption

Seed laser temperature stabilization using the TOSA integrated TEC is essential for wavelength alignment of the laser with the extinction filter. The TEC allows the precise control of the laser diode's temperature T_{set} even if ambient temperature T_{amb} is changing. In this experiment we wanted to validate the vendor's TEC power consumption specification of $0.4\,\text{W}$ and understand how TEC power consumption changes as the $\Delta T = T_{amb} - T_{set}$ changes.

The TOSA's TEC power consumption was validated by measuring both V_{TEC} and i_{TEC} while the setpoint (T_{set}) was swept relative to ambient (T_{amb}). Figure 4-5 shows the measured power consumption as well as quadratic models for both heating and cooling modes. TEC power consumption was within the $0.4\,\text{W}$ budget across the expected operational range for the device ($0\,^{\circ}\text{C}$ to $40\,^{\circ}\text{C}$). The quadratic relationship between ΔT and power consumption agrees with analytical models presented in [107] and experimental measurements in [27].

Flight Laser Thermal Controller

We made the TEC power consumption measurements using a laboratory grade laser diode controlled that is inappropriate for the flight design. We wanted to gain experience with integrated TEC controller solutions to understand their performance (i.e., temperature stability) and efficiency (i.e., DC power input relative to power delivered to the TEC). The TEC's $0.4\,\text{W}$ power consumption is a small fraction of the
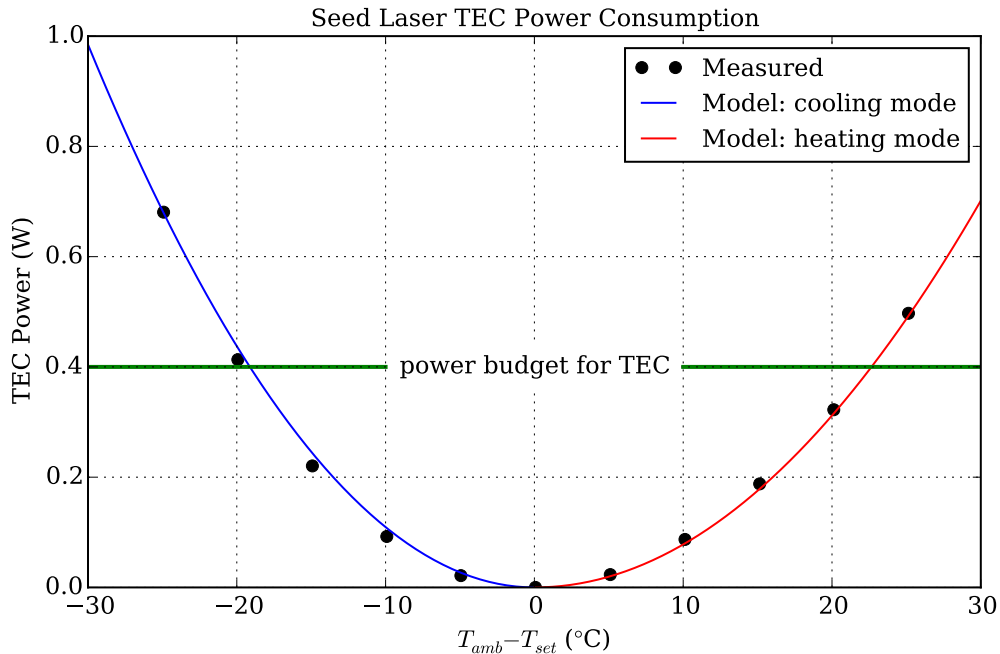
Figure 4-5: TEC power consumption as temperature set point is swept relative to ambient. Given a TEC power budget of 0.4 W, the data shows that the device can support a 40 °C operating range can be supported.

transmitter's 8 W power budget, however, this hinges on the efficiency of the driver circuit.

Compact TEC driver solutions are available from a variety of integrated circuit (IC) vendors (e.g., Linear Tech LTC1923, Analog Devices ADN8831). Most of these devices incorporate the entirety of the control loop and just need to be connected to the TEC and a temperature sensor. We selected the Linear Tech LTC1923 for testing because the vendor provides an evaluation board [108].

We identified an implementation complexity while configuring the LTC1923 evaluation board for use with the TOSA: the TEC used in the TOSA modules has a very low DC resistance of approximately $0.2\,\Omega$. This is roughly an order of magnitude lower than the resistance of TECs found in larger "butterfly" package lasers or for the TECs assumed in the LTC1923 design documentation. To achieve a given power input to the TEC, the TEC driver current must deliver higher currents to the device (relative to "typical" TECs which have higher resistance). High DC currents can lead to I^2R resistive losses which further motivated study of a flight-scale controller like the LTC1923.

Power measurements taken from the factory-configured LTC1923 evaluation board and the TOSA seed laser TEC are shown in Figure 4-6. Efficiency is very poor, approximately 25% across most of the operating range.

Analysis of the driver circuit identified the dominant losses in the circuit (Figure 4-7). Relative to the $0.2\,\Omega$ TEC element, the DC resistances of the switching
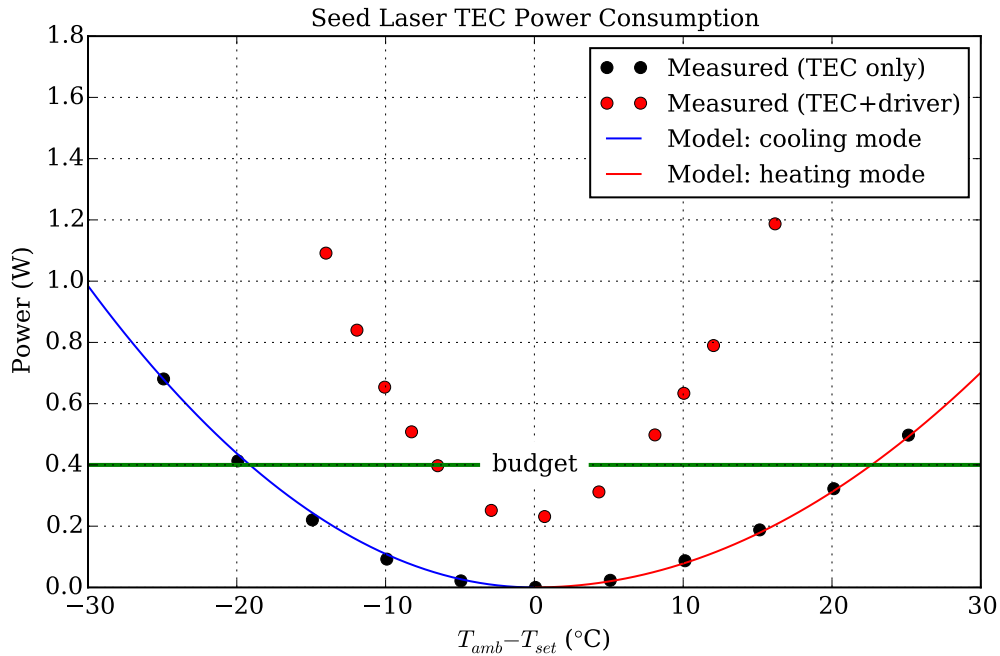
Figure 4-6: Power consumption measurements for the TEC+driver assembly as compared to the TEC-only data. The peak efficiency of the driver is approximately 25% at high ΔT. The driver also adds significant quiescent power consumption (0.25 W) even when the TEC is inactive ($\Delta T = 0$).

MOSFETs, ripple filter inductors, cabling and sense resistors are all relevant. Given the component parameters for the LTC1923 evaluation board, the overall predicted efficiency of the circuit was 26% which is in good agreement with the measured data. This gives confidence in the analysis process.

For the flight design a number of the circuit parameters can be optimized to improve driver efficiency. First, the cable loss term will approach zero since the TEC driver circuit will be implemented adjacent to the seed laser (TOSA) on one circuit board. Second, the sense resistor which is used by the LTC1923 to measure TEC current, can be reduced by a factor of ten and still produce an adequate sense signal for the controller. Third, the ripple filter inductors can be exchanged for components with lower series resistance. This is possible through the use of physically larger devices, or by increasing the controller's switching frequency which lowers the required inductance (and consequently series resistance). The efficiency analysis indicates that if these changes were implemented, the driver should be able to deliver 60% efficiency at a minimum.

Implementing the driver circuit changes would require a custom circuit board. Since the analytical model was validated with measurements from the stock configuration of the driver board, the build and evaluation of the more efficient driver board is planned future work for the flight configuration, including repeating validation measurements.
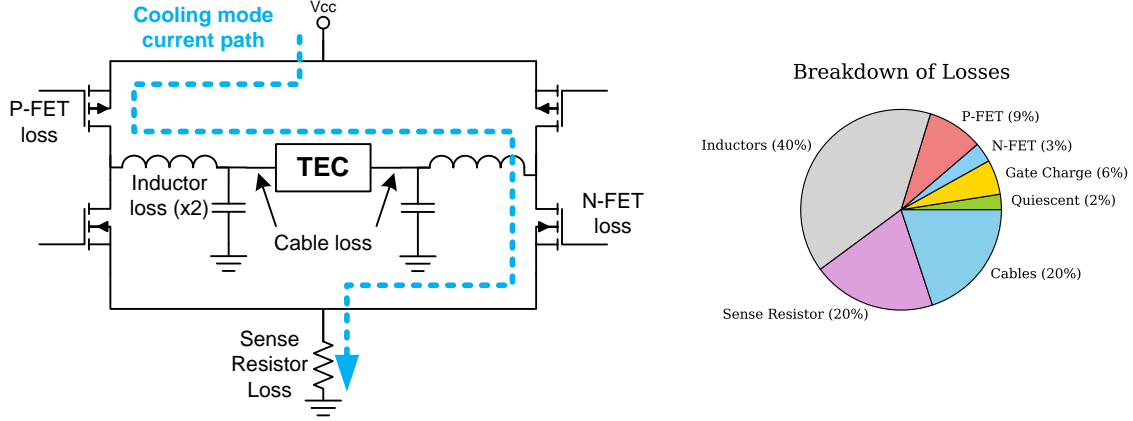
Figure 4-7: Simplified schematic of TEC driver power electronics showing dominant loss terms as well as comparison of the loss terms present in the LTC1923 evaluation board design.

4.2.5 Extinction Filter Characterization

The extinction filter is used to improve the ER of the seed laser signal through FM-to-AM conversion. Wavelength alignment between the seed laser and the filter passband is necessary to simultaneously achieve high ER and low insertion loss. In order to realize the peak power advantages of high order PPM modulations, such as PPM-128, it is necessary to improve the ER to $> 36\,\mathrm{dB}$ [93, 89, 27, 105].

Athermal fiber Bragg grating (FBG) filters are a convenient choice for narrow-band filtering of fiber-coupled signals. These devices can provide both steep transition regions ($\gg 1\,\mathrm{dB/GHz}$) and high stopband attenuation ($> 40\,\mathrm{dB}$) along with a thermally stable center wavelength ($\sim 100\,\mathrm{MHz/°C}$). A temperature sensor mounted to the FBG filter will be used to compensate for the slight thermal dependency of the FBG filter (Section 4.3.2). The overall wavelength shift of the transmitter ($\sim 4\,\mathrm{GHz}$ over full temperature range) during this compensation is acceptable since the ground station receiver optical filter bandwidth is $125\,\mathrm{GHz}$ (or $1\,\mathrm{nm}$ at $1.55\,\mathrm{\mu m}$).

Since the AC frequency chirp of the seed laser was unknown early in the project, we obtained two different Gaussian passband FBG filters with $5\,\mathrm{GHz}$ ($4\,\mathrm{pm}$) and $10\,\mathrm{GHz}$ ($8\,\mathrm{pm}$), $3\,\mathrm{dB}$ bandwidths. Since these filters are reflective in their passband, a fiber circulator is used to transform them into a transmission-mode filter (Figure 4-8).

An automated test bench consisting of a narrow line width tunable laser, a power meter, and a wave meter were used to sweep through the passband of the filter. Important performance metrics for the bandpass filter include its center wavelength, its bandwidth and its stopband rejection. Stopband rejection is critical for this application and can be compromised if the FBG is poorly terminated or if the fiber junctions surrounding the filter are contaminated or dirty. Figure 4-9 compares the insertion loss of two Gaussian passband FBG filters considered for this application along with the expected wavelength "chirp" ($\Delta\lambda/\Delta i_{AC}$) of the seed laser.
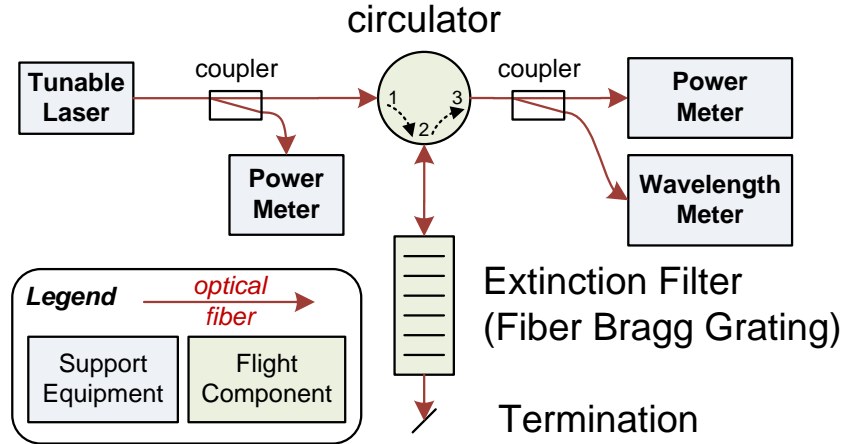
Figure 4-8: Experimental configuration used to characterize the extinction filter. A narrow line width tunable laser was swept through the passband of the filter while power meters were used to measure insertion loss.

4.2.6 Seed Laser Alignment & Extinction Ratio Validation

Alignment of the seed laser with the FBG filter was accomplished using the tuning characteristics of the seed laser (Section 4.2.3) and the measured center frequency of the FBG filter. Laser diode temperature was used for "coarse" tuning and laser bias current was used for "fine" tuning. Final alignment was accomplished manually by maximizing peak power of the "mark" symbol by observing the output of the FBG filter with a high bandwidth photodiode (Figure 4-10). When properly aligned, the "mark" symbol is positioned at the center of the FBG passband and the "space" symbol is well into the filter's stopband[2].

Measurement of high ER is difficult because the measurement device must have a dynamic range exceeding the target ER ($> 36\,\text{dB}$). The high bandwidth photodiode is able to temporally resolve the mark and space symbols but the associated capture electronics (digitizing oscilloscope) only has about $20\,\text{dB}$ of dynamic range. Continuous wave power meters on the other hand have very low bandwidth ($\sim 1\,\text{Hz}$) but excellent dynamic range ($> 100\,\text{dB}$).

A swept duty-cycle ER measurement technique [109, 27] that only relies on low-BW high dynamic range power meters was used to validate ER. In systems with infinite ER, reducing the duty cycle by a factor of two results in optical power dropping by a factor of two. Systems with finite ER will deviate from this linear relationship and will "floor" at a relative power level equal to the ER. We use an automated test bed to make the ER measurements with two power measurements: one at the output of the filter (Power Meter B) and one at the input to the filter (Power Meter A). Power meter A allows for compensation of deviations in seed laser output power between the measurement points (Figure 4-10).

---

[2]The inverse case, where the "space" symbol is in the filter passband, is easily identified as inversion of the signal as seen at the monitor photodiode.
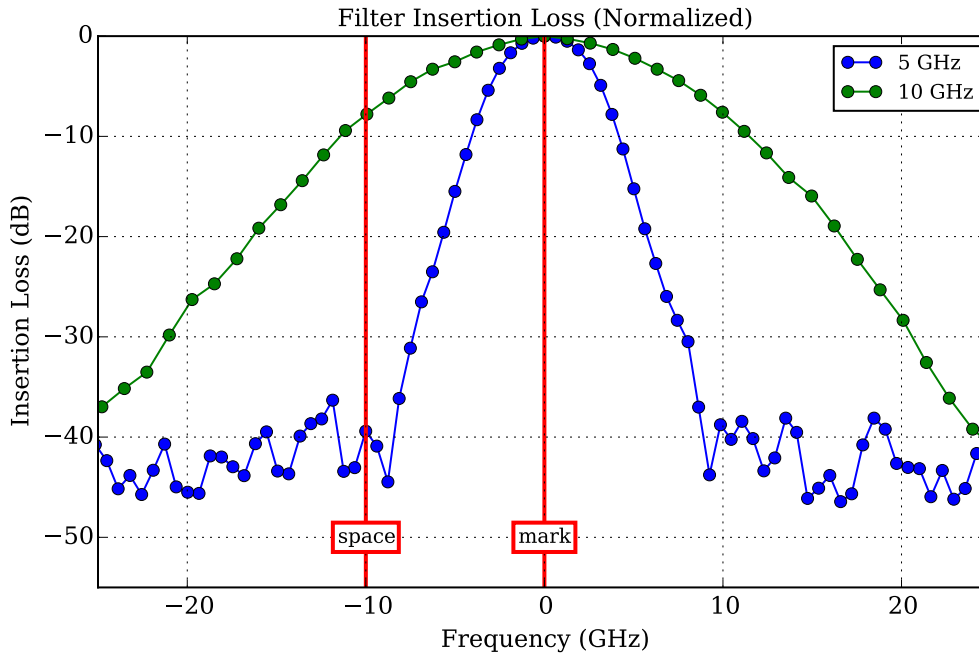
Figure 4-9: Passband comparison of 5 GHz and 10 GHz filters. The seed laser "space" and "mark" wavelengths, seperated by the AC chirp shift are also marked.

The swept duty-cycle ER measurements showed that the combined seed laser plus extinction filter achieved an ER of $> 40\,\mathrm{dB}$ at $f_{slot} = 200\,\mathrm{MHz}$ (Figure 4-11). This ER is sufficient for low duty-cycle waveforms such as 128-ary PPM. The same measurement was completed at $f_{slot} = 40\,\mathrm{MHz}$ which showed a slightly degraded ER ($\approx 28\,\mathrm{dB}$). We believe that this is due to fact that the modulation frequency is closer to the transition point where thermal effects begin to dominate charge carrier density effects [6]. Based on these results, we plan to operate the transmitter at a fixed $f_{slot} = 200\,\mathrm{MHz}$ and will vary the modulation order (M) to achieve a variety of link rates. This design decision also allows for simplifications at the receiver (e.g., a single matched filter design can support all system data rate).

4.2.7 Fiber Amplifier Validation

Erbium-doped fiber amplifiers (EDFAs) are widely available due to their use in the telecommunications industry. Because of the budgetary constraints facing most Cube-Sat programs, it was desirable to select a low-cost, mass-produced EDFA. The industry standard multi-source agreement (MSA) form-factor is ideal for CubeSat applications as its size ($9\,\mathrm{cm} \times 6\,\mathrm{cm} \times 1.5\,\mathrm{cm}$) just fits within the $10\,\mathrm{cm} \times 10\,\mathrm{cm}$ CubeSat chassis cross-section.

MSA form-factor EDFAs are offered in a variety of power output levels and gains. We selected a higher power output variant ($200\,\mathrm{mW}$ average optical) that fell within our electrical power budget ($8\,\mathrm{W}$ for entire transmitter). The vendor made minor
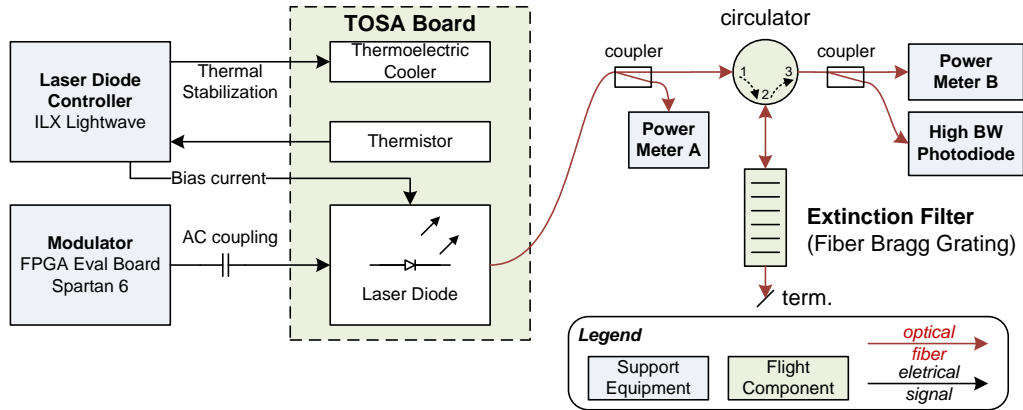
Figure 4-10: Experimental configuration for seed laser alignment with the FBG filter and for measurement of output signal extinction ratio. The high bandwidth photodiode diode was used for alignment diagnostics. The two power meters were used to infer the extinction ratio (ER) using a swept duty-cycle approach.

mechanical modifications (moved the fiber egress position on chassis) to the unit so that fiber bend radius constraints can be observed within the $10\,\text{cm} \times 10\,\text{cm}$ chassis cross-section.

The EDFA was connected to the output of the seed laser and extinction filter assembly and the output was monitored with an optical power meter and an optical spectrum analyzer (OSA). Time domain observations of the amplifier output were also completed using a high-bandwidth photodiode, which confirmed that the output pulse waveform was well-shaped and that energy was contained within the $5\,\text{ns}$ signal slots (Figure 4-12). The OSA allowed measurement of the EDFA's amplified spontaneous emission to ensure that the amplifier was being driven well into saturation.

Peak Output Power Measurements

Figure 4-13 shows the achieved peak output power from the EDFA at various duty cycles. Because the EDFA behaves in an average-power-limited fashion, lower duty cycle waveforms result in higher peak power levels. As constructed, the prototype is able to delivery peak power levels within $0.15\,\text{dB}$ of theory in the lowest duty cycle mode (PPM-128). This data validates the peak-to-average power ratio that is present in the receiver noise analysis and which forms the basis for the energy storage capability of the EDFA.

4.2.8   Overall Transmitter Power Consumption

Transmitter power consumption is one of the primary performance limiters of implementing a lasercom terminal on a nanosatellite. Table 4.2 gives a power consumption breakdown for the entire transmitter. All of the values in this table are measured values, with the exception of the FPGA logic term which was estimated using power
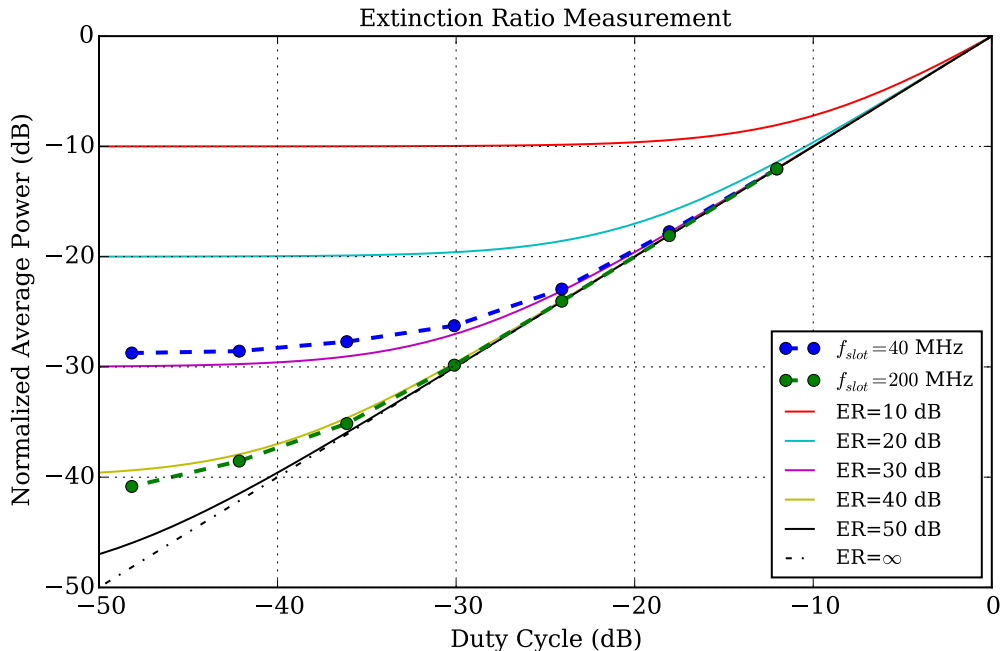
Figure 4-11: Duty-cycle sweep extinction ratio measurement data for two f_{slot} rates considered for the application. The 40 MHz slot rate has degraded ER because the laser has lower AC frequency chirp at this modulation frequency. At 200 MHz the system achieves ER greater than 40 dB.

dissipation prediction software from the FPGA vendor. The EDFA, which is the dominant power consumer, was actually measured 4.1 W even through the manufacturer specification states 5.7 W. We suspect this is because the manufacturer specification is very conservative (as is common with telecommunications components) and assumes end-of-life (10 year) and worst-case thermal conditions (0 °C to 65 °C).

4.3   Loopback Receiver

Testing the end-to-end performance of the communications link was a high priority during the validation effort. The achievable data rate of the link for the system is currently limited by the noise parameters of the communications detector, a COTS APD/TIA module. Validating the vendor noise specification of this device was a crucial step towards building confidence in the link budget.

Instead of implementing a stand-alone PPM receiver, we implemented a low-complexity "loopback" receiver (Figure 4-14), which can be used to provide real-time feedback on transmitter performance as in [87, 105, 110]. This receiver consists of a comparator-based analog front-end that converts the input analog electrical signal into digital for processing by the FPGA. A digital to analog converter (DAC) is used to generate a threshold voltage that can be adjusted to optimize the error rate.
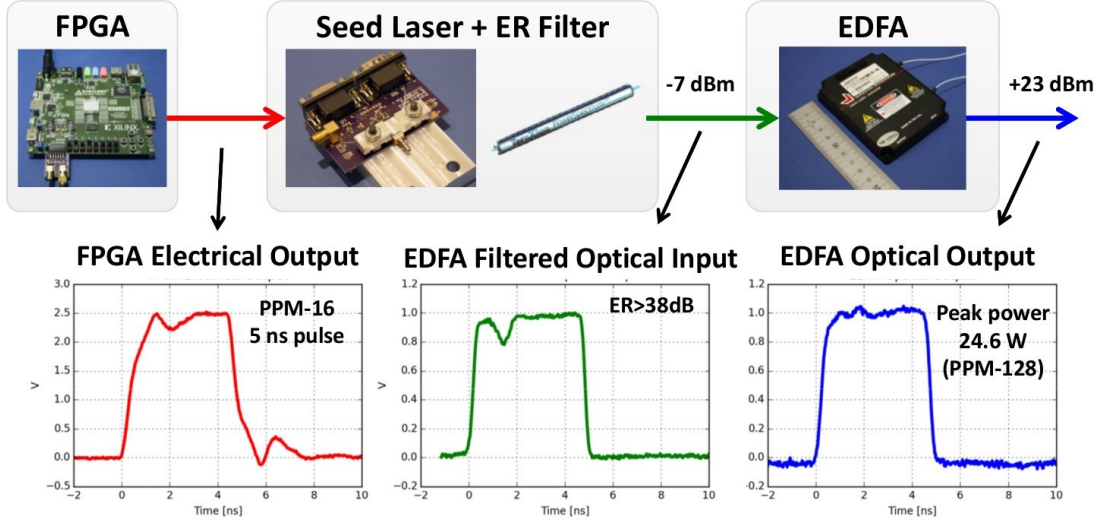
Figure 4-12: Representative electrical and optical waveforms of the mark slot while the transmitter was modulating PPM-16 at $f_{slot} = 200\,\mathrm{MHz}$.

Table 4.2: Transmitter power consumption summary

Parameter	Value	Notes
EDFA	5.7 W	Manufacturer worst case specification
Seed laser TEC	0.7 W	Peak over 0 °C to 40 °C*
Seed laser DC bias	0.2 W	Worst case
Seed laser AC drive	0.01 W	50 mA, 1/16 duty cycle
FPGA logic	0.2 W	Transmitter portion of FPGA**
Total	6.71 W	
Margin	1.29 W	8 W budget for transmitter

* Includes 60% efficient TEC driver circuit
** The FPGA is shared with other functions in the lasercom terminal

Inside the FPGA, the received digital signal is compared to a delayed copy of the transmit signal. Differences between the two bit streams are identified with an exclusive-OR (XOR) gate and subsequently counted. The FPGA also keeps count of the total number of cycles that have elapsed which allows calculation of a slot error rate (SLER). Given knowledge of the PPM order M, it is possible to map SLER into a symbol error rate and, subsequently, bit error rate (Appendix A.2).

The main advantage of the loopback receiver is that it operates from the same reference clock as the transmitter. For this reason, it is not necessary to implement clock and data recovery (CDR) functionality. Although CDR will be needed for a flight demonstration, we view this as a straightforward application of prior works [67, 68, 69].
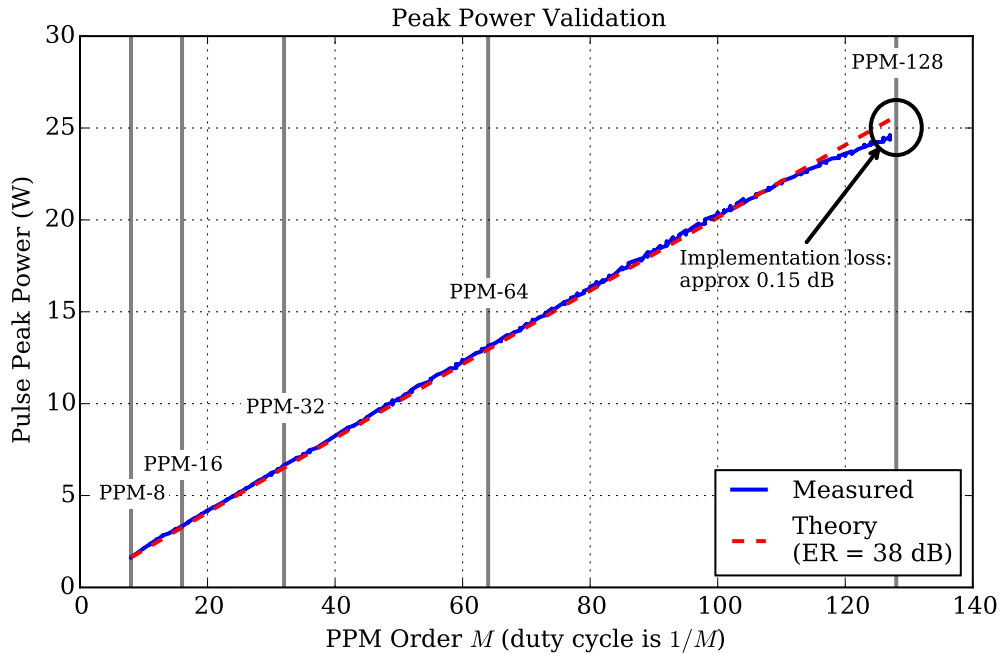
Figure 4-13: A linear photodiode was used to measure the peak output power of the EDFA at various duty cycles. The design exhibits average-power-limited behavior and produces peak output power levels to within $0.15\,\mathrm{dB}$ of predicted performance.

4.3.1 Receiver Sensitivity Validation

Most communication systems are validated in an end-to-end fashion through the collection of BER curves, or data that shows how BER degrades as the receiver's input power is decreased. This optical output of the transmitter is attenuated by both fixed and variable attenuators to establish an optical power at the detector module that is similar to the levels predicted by the link budget (Section 2.4.1). This attenuation simulates the aperture gain terms, path loss, and other loss terms predicted for the link. Attenuation is generally swept from the error-free regime (BER $\approx$ 0) to the point where the error rate has reached the maximum possible value (BER = 0.5). Attenuation step sizes of $0.1\,\mathrm{dB}$, which are well within the capabilities of a laboratory grade variable attenuator, are generally sufficient to resolve the BER curve.

The BER curve measurement process has been fully automated. This greatly improves experimental repeatability and allows many trials. An operating point for the transmitter is defined by the tuple (M, L_{atten}). At each operating point two additional degrees of freedom exist in the receiver: the value of the delay block t_{delay} and the value of the threshold voltage, V_{DAC}. The value of t_{delay} matches the delay of the signal as it propagates through the seed laser, extinction filter, EDFA, attenuators, and detector circuit. In practice this was measured once with an oscilloscope and then hard-coded in the automation script. The optimal value of V_{DAC} (i.e., the value that minimizes BER) depends on the signal levels present at the comparator input. To
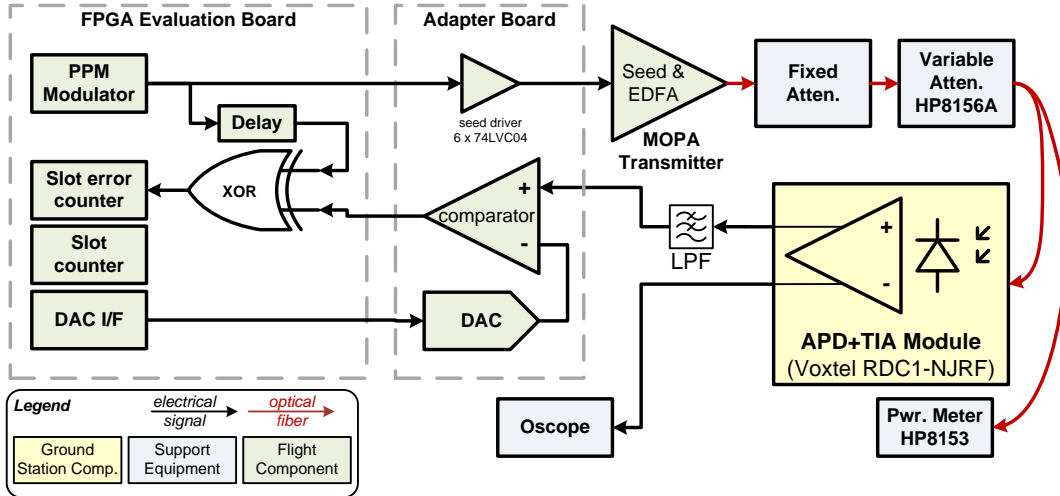
Figure 4-14: The loopback receiver compares the received digital signal to a delayed version of the transmit signal in order to infer slot-error-rate. A DAC and a comparator form a 1-bit ADC that is used to convert the input analog waveform into a digital signal.

find this value, the test automation script exhaustively tests all possible values and reports the best BER found during the search. This process is repeated at every (M, L_{atten}) operating point. The BER automation script also collects power meter measurements to precisely document the input power to the detector.

Once collected, the data is post-processed to incorporate calibration parameters from the test apparatus (e.g., coupler ratios). The receiver power figure is also normalized into photons-per-bit for comparative purposes. The measured data shows that the receiver is approximately 2.4 dB to 3.0 dB less sensitive than predicted depending on the mode. Lower rate modes, such as PPM-128, are closer to the predicted sensitivity than the high rate modes (e.g., PPM-8). Both measured and theoretical BER curves (derived in Appendix A) are given in Figure 4-15.

The sensitivity shortcomings of the prototype system have been the subject on an ongoing investigation. In the theoretical sensitivity analysis, the detector APD and its noise parameters set the overall sensitivity of the system (model source code in Appendix A.3). In the current laboratory prototype, we believe that electrical noise sources after the APD/TIA module, especially on the "adpater board" which hosts the comparator decision circuit (see Figure 4-14) may be to blame. The seed laser modulation traces lie in close proximity to the decision circuit so crosstalk is likely an issue. Despite these limitations, we view the experimental demonstration of end-to-end (transmitter to receiver) performance less than 3 dB from theory as being one of the most significant results in this thesis.

4.3.2 Built-In Self-Test Provisions

The loopback receiver has utility beyond ground testing [87, 105, 110]. We envision that a variant of this receiver will be integrated into the flight design to provide a
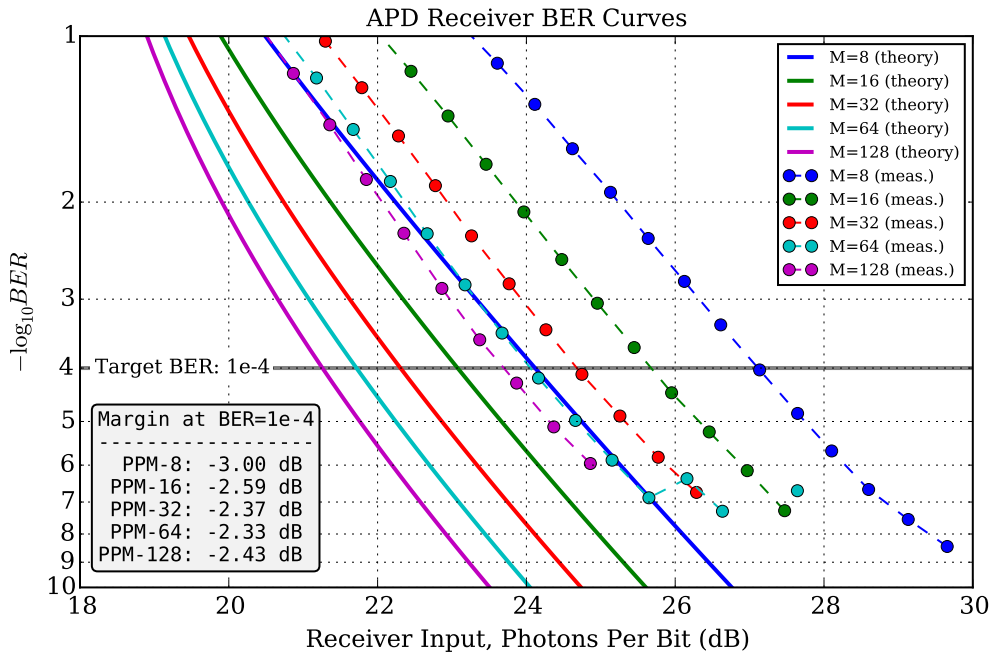
Figure 4-15: Bit error rate (BER) curves for the end-to-end communication link including the prototype transmitter and fiber-coupled variant of the ground station APD/TIA receiver module. The design is 2.4 dB to 3.0 dB from predicted sensitivity. The source of this descrepancy is currently under investigation, but electrical cross talk between the seed laser driver and the comparator decision circuit is suspected. Code used to generate the theoretical curves can be found in Appendix A.3.

built-in self-test (BIST) functionality. This receiver will be able to provide important diagnostic information about the health of the optical transmitter. In the event of failure of the pointing, acquisition and tracking (PAT) subsystem, this receiver can be used to establish partial mission success through on-orbit validation of the transmitter.

For the flight variant of the loopback receiver, it is not necessary to use a high-sentivity cooled APD/TIA module. Instead, low-power fiber-coupled photodiode(s) will be used to monitor the transmit signal at various points in the transmitter chain. Monitoring the signal at strategic points in the transmitter chain can give insight into the operating performance of the transmitter (Figure 4-16).

Given a transmitted signal $x(t)$, we assume that the BIST system has monitor capability at three points along the transmit chain:

- $y_A(t)$ is proportional to the EDFA output which includes peak power gains imparted by the average-power-limited amplification process

- $y_B(t)$ is proportional to the EDFA input, nominally a high ER signal consisting of "mark" symbols

- $y_C(t)$ is the seed signal rejected by the FBG filter, also nominally a high ER signal but consisting purely of "space" symbols

Each of the monitor points is connected to a comparator with a variable threshold as described in Section 4.3. The FPGA provides the ability to measure slot error rate (SLER) as well as the occurrence rate of high ("mark") and low ("space") slots.
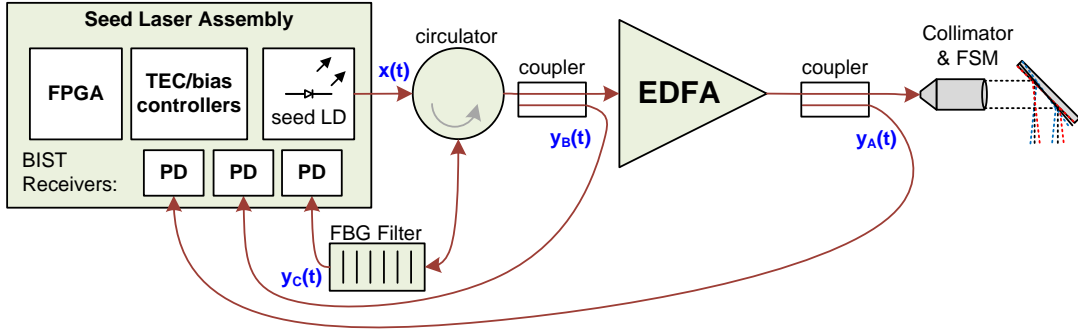
Figure 4-16: BIST functionality expands upon the loopback receiver design by monitoring the transmitter optical chain at various points. Each of these signals can be converted to the digital domain (configurable threshold) and compared to delayed copies of the transmit signal.

EDFA Peak Power Measurement

In order to maximize delivered signal power and SNR at the receiver [27, 82], the transmitter must maximize its peak output power while maintaining crisp 5 ns optical pulses. Monitor signal $y_A(t)$ can be use to monitor peak power. Unlike the loopback test presented previously, this test does not attempt to adjust the receiver parameters to minimize slot error rate. Instead, the decision threshold voltage is adjusted to find the peak of the optical waveform (a similar design is presented in [111]).

A counter was added to the FPGA design to track the number of slots where the input signal is high (or a "mark" slot), we call this value n_{mark}. The FPGA also maintains count of the total elapsed slots, n_{total}. Both of these counters can be reset and sampled or "latched" simultaneously and can be used to calculate $P1$, the duty cycle of the signal and occurrence rate of high slots.

$$P1 = \frac{n_{mark}}{n_{total}} \tag{4.1}$$

For a given PPM modulation order M, the signal's nominal $P1$ value is $1/M$. Furthermore, $P1$ is monotonically decreasing as V_{DAC} is increased (Figure 4-17). We are able to obtain an estimate for the peak power by maximizing V_{DAC} subject to obtaining $P1 = 1/M$.

The receiver must have sufficient dynamic range for the expected range of transmit powers, for a PPM-8 through PPM-128 system, this is approximately 12 dB, which is straightforward to implement. Another implementation challenge associated with this

90

approach is the need to "sweep out" the wide range of DAC values where $P1 = 1/M$ in order to find the maximum for V_{DAC}. A more efficient approach is to search for the transition region where $P1$ drops from $1/M$ to zero (shown in green in Figure 4-17). Laboratory experimentation showed that a target value of $P1 = 0.9/M$ produced repeatable measurements. Additionally, the monotonic nature of $P1$ relative to V_{DAC} allows the use of a binary search algorithm which completes after $\log_2 k$ measurements with a k bit DAC.
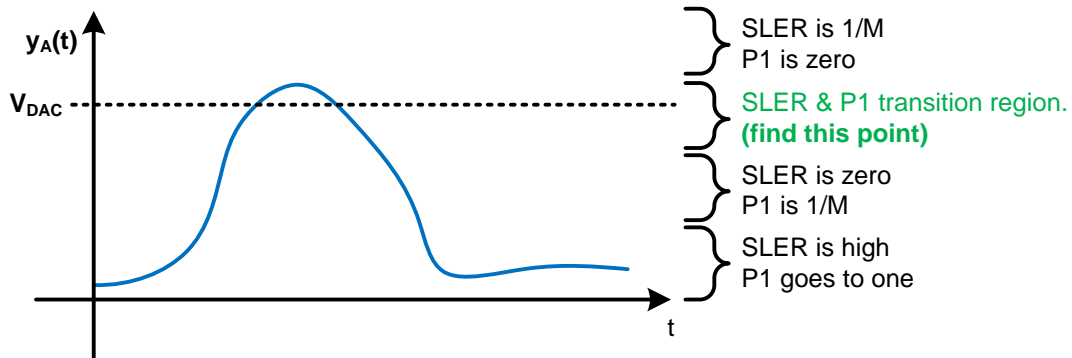
Figure 4-17: The receiver threshold voltage V_{DAC} is adjusted to find the peak of the optical waveform. At low values, near the noise floor of the receiver, the slot error rate (SLER) will be very high. Above that, SLER will reach a minimum at the optical decision voltage. $P1$, the occurrence rate of "high" slots is decreases monotonically with increasing V_{DAC}.

Experimental results, which validate this measurement technique are provided in Figure 4-18. The transmitter peak output power was varied by changing the modulation order M. A highly-linear photodiode along with an oscilloscope was used to measure the true peak power of the optical waveform. Simultaneously, the peak power estimation feature of the BIST receiver was used to collect peak power estimates. The measurement technique has strong correlation ($R^2 = 0.9993$) with the truth value and the design requires minimal FPGA resources. The binary search based measurement procedure currently takes approximately $1\,\mathrm{s}$ to complete, however, this could be sped up significantly ($> 10\,\mathrm{Hz}$ is estimated) by migrating the algorithm from the control PC into the FPGA.

Seed Laser Auto-Alignment Capability

Proper alignment of the seed laser with the fiber Bragg grating (FBG) filter is crucial for establishing a high extinction ratio. As mentioned in Section 4.2.5 the FBG filter has a thermal dependency ($\sim 100\,\mathrm{MHz/°C}$) that needs to be compensated for given the $0\,\mathrm{°C}$ to $40\,\mathrm{°C}$ operating range. Fortunately, these thermal dependencies are very repeatable and can be modeled [112]. The flight design of the lasercom terminal would include a temperature sensor attached to the FBG grating and a look-up table would be used to predict the center frequency of the filter across operating
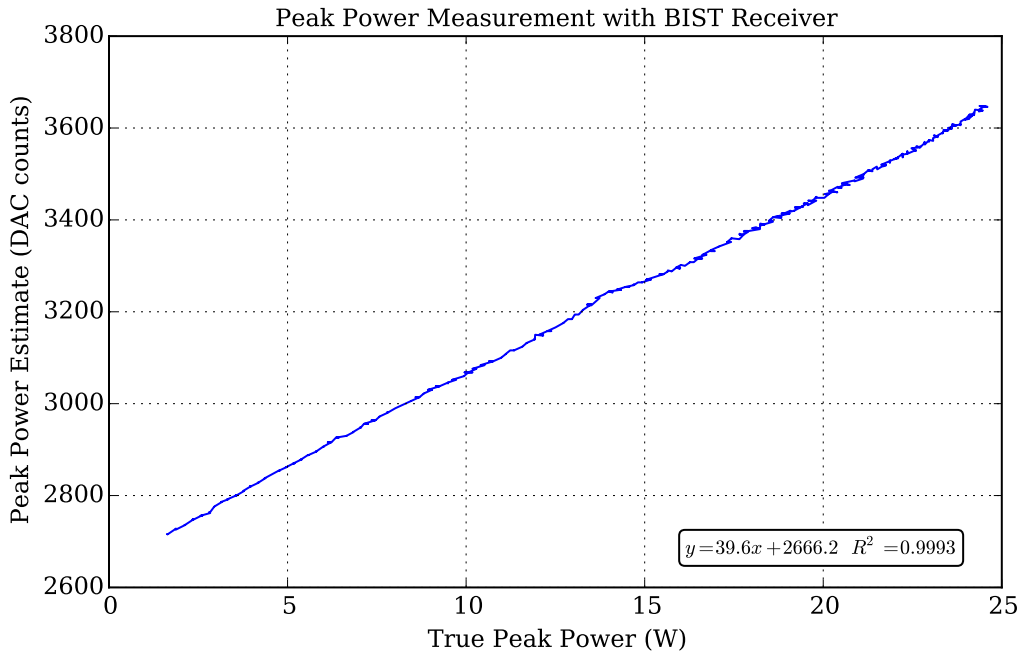
Figure 4-18: Peak power estimation measurement results using the BIST receiver as compared to true peak power measured with a highly linear photodiode and oscilloscope. A linear relationship ($R^2 = 0.9993$) exists between the truth data and the measurement.

temperature range. Due to device-to-device manufacturing variations, it is likely that this approach would require characterization of each FBG filter.

An alternative approach is to make use of the peak power measurement technique described in the previous section. Frequency tuning the laser, by sweeping through the laser temperature (T_{LD}) and laser bias (i_{DC}) space, while attempting to maximize the peak power ($P_{pk,est}$) can be used to establish alignment. A contour plot of $P_{pk,est}$ across the (i_{DC}, T_{LD}) tuning space is shown in Figure 4-19. Since both temperature and bias current can be used to tune the laser, there is a not a unique solution for maximum peak output power, however, the adjustment space is further constrained by our desire to minimize transmitter power consumption. An area for future research is to develop power-consumption-aware refinements to this alignment algorithm so that it can simultaneously find a suitable operating point while minimizing power usage.

As described in Section 4.2.4, the TEC power required to establish a given T_{LD} is dependent on the difference relative to the ambient temperature of the transmitter. Similarly, the minimizing diode current i_{DC} is also desirable for power savings. Finally, a certain minimum bias current $i_{DC,min}$ must be provided in order to ensure sufficient optical drive at the EDFA input. We propose a (i_{DC}, T_{LD}) search methodology that observes these three constraints while attempting to maximize peak optical power.
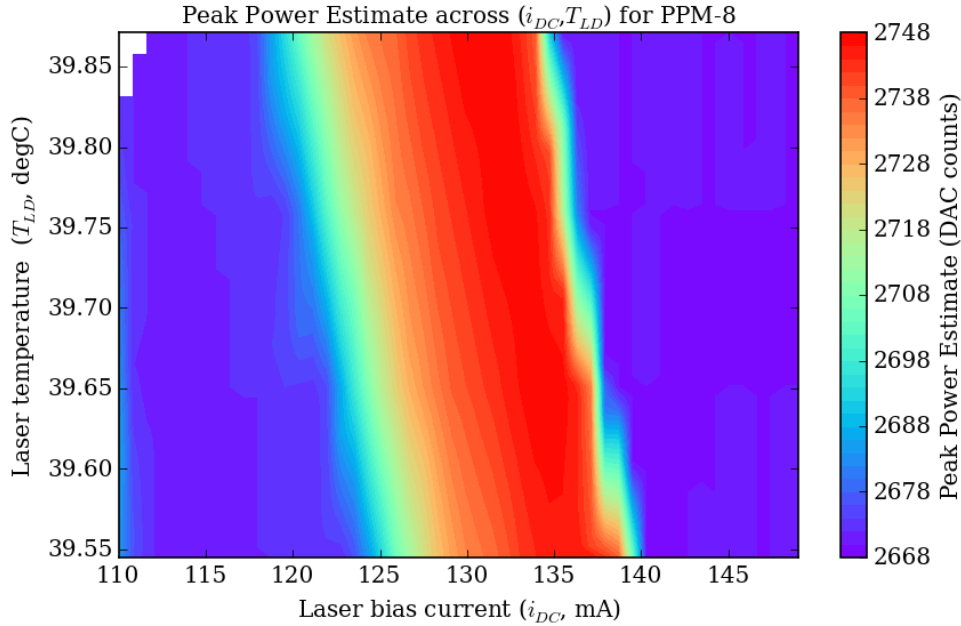
Figure 4-19: Contour plot showing peak power estimates across the (i_{DC}, T_{LD}) wavelength tuning space.

4.4 Fine Steering Mechanism Characterization

In this section we analyze the performance of the MEMS FSM and present methods under consideration for determining the proper drive voltages needed to achieve a desired steering angle. Since we will be operating the mirror in an open-loop configuration, the driver will need to be capable of compensating for nonlinearities in the high-voltage drive electronics and MEMS actuator. The analysis that follows is based on a batch order (quantity 4) of 13L2.2 MEMS actuators fitted with 3 mm mirrors. This device has approximately a ± 21.8 mrad ($\pm 1.25°$) steering range in both axes.

4.4.1 Measurement Apparatus

To measure the voltage-to-angle transfer functions of the FSMs, we developed a test bed capable of driving the mirror with known voltages while measuring the mirror's angular deflection. A block diagram and picture of this apparatus is shown in Figure 4-20. A control PC has been configured to command a vendor-provided FSM driver board (an MTI "PicoAmp"). This driver board provides a digital-to-analog converter (DAC) and a high-voltage amplifier capable of generating the ± 120 V drive voltages needed by the FSM. A converging 650 nm laser beam reflects from the mirror surface and is focused on a focal plane array (FPA). The focal length of the system and the relative spacing of the lens, FSM and FPA must be carefully selected to avoid unwanted reflections and to maximize the usable resolution of the focal plane array.

The displacement of the spot on the FPA is estimated using a center-of-mass
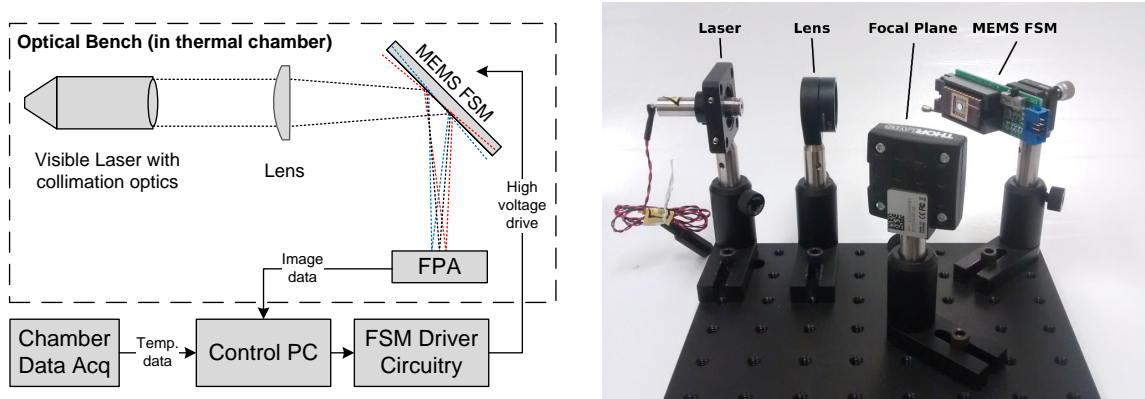
Figure 4-20: Block diagram and photo of the FSM measurement testbed. Focused laser light is reflected off the FSM and focused on to a bare focal plane array.

centroiding algorithm and this result is then converted into an angle estimate for the FSM. Centroiding algorithms typically yield measurement accuracy better than 10% of pixel size [113]. The FPA that is currently being used in the setup is a monochrome 1280×1024 pixel device with $5.2\,\mu m$ pixel pitch. The spacing between the FSM and the FPA were adjusted such that the FSM's full range ($\pm 25\,mrad$) spans most of the FPA area. Given these parameters, the apparatus yields measurement precision better than $10\,\mu rad$.

One notable limitation of this test bed is measurement bandwidth, which is limited by the frame rate of the focal plane array ($\sim 10\,Hz$). This is sufficient for our measurement approach since we intend to command the device at approximately $1\,Hz$. The FSM vendor uses a much different measurement approach. Their test apparatus is based on a position sensitive photodiode (PSD) which provides higher measurement bandwidth but with reduced precision [103].

4.4.2 Transfer Functions

Preliminary transfer function measurements focused on the single-axis behavior of the FSMs. Figure 4-21 shows the single axis measurements from a representative device. Qualitatively, the device response is primarily linear with slight roll-off near the range limits. We fit both linear and polynomial models to these measured data to generate residual error plots. A linear model was insufficient for capturing the transfer function of the device while remaining within the accuracy requirement ($\pm 0.11\,mrad$, 3-σ). A fifth order polynomial, however, was sufficient.

Interestingly, one of the devices tested (S4045) showed symptoms of hysteresis during the single-axis tests (Figure 4-22). We have not been able to identify the underlying cause for this hysteresis as the vendor has informed us that it is generally not observed in this type of MEMS actuator. A closer inspection of the vendor-provided data for this device also showed the hysteresis, though it was mostly obscured by measurement noise. At a minimum, this particular device has given us confidence in our ability to screen devices for this effect.
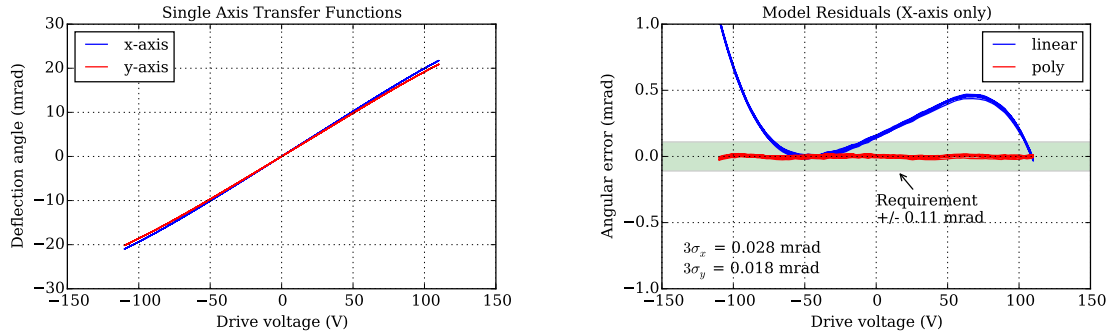
Figure 4-21: Single-axis transfer functions as well as residuals after linear and polynomial models were fitted and subtracted from the measured data.

The single-axis measurements and polynomial models do not account for mechanical coupling that occurs between the two axes. To understand the two-axis behavior of the device, a 32×32 grid of sample points distributed evenly across the full range of the device were collected. Using this sample grid as a truth reference, we measured the angular error relative to the angle established with the previously defined single-axis polynomial models. With this approach, the achieved accuracy is insufficient across much of the device's 2D range (Figure 4-23). Because of the 2D non-uniformities of the FSM, it will likely be necessary to interpolate across a 2D look-up table to linearize the device.

4.4.3 Repeatability

The fine steering mechanism (i.e., the FSM and the driver) must be able to reliably revisit commanded points. A test script was developed to randomly drive the mirror between five predetermined points in a "dice" pattern (Figure 4-24). Each point of the five points was visited 100 times and the walk sequence was designed to avoid repeated positions within the sequence. Once the mean point positions have been removed, it is clear that the points are tightly clustered (± 0.028 mrad 3-σ) within the required accuracy region (± 0.11 mrad 3-σ).

4.5 Environmental Testing

All of the tests described below have been conducted at standard atmospheric pressure in a thermal oven. The expected operating range for the lasercom payload components is $0\,°C$ to $40\,°C$, however, we have opted to test across $-20\,°C$ to $60\,°C$. We expect these experiments to be repeated under vacuum conditions once the flight-packaged version of the terminal has been assembled (Section 5.2.3).

4.5.1 Fine Steering Mechanism

Given the open-loop drive technique, validating that the MEMS fast-steering mechanism (FSM) was consistent across temperature was a high priority. The measurement

95
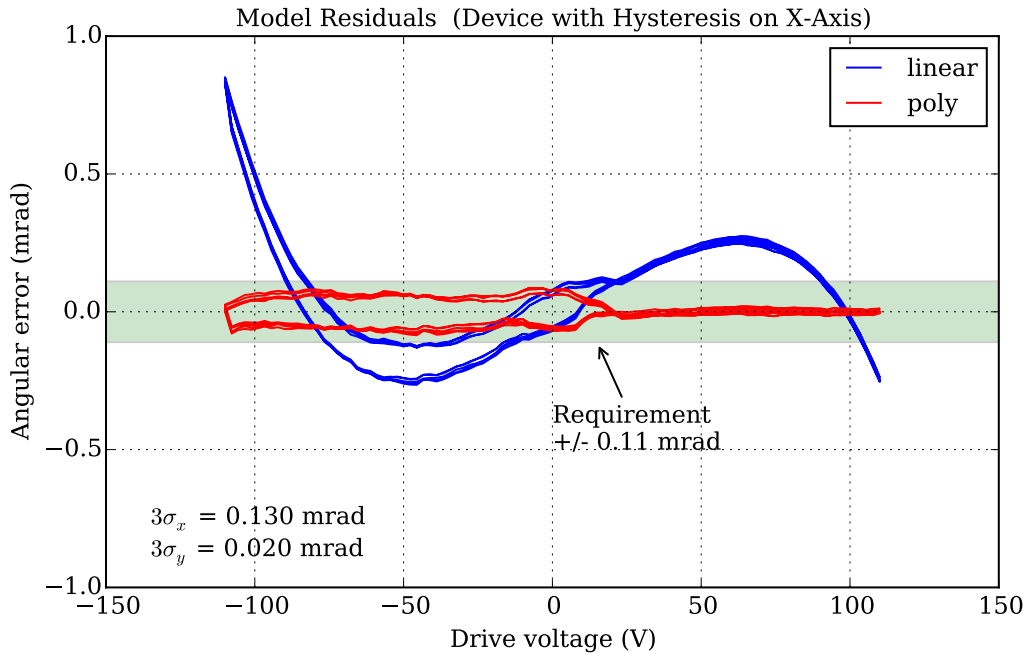
Figure 4-22: Hysteresis was discovered during single-axis measurements of one device of the batch tested. Hysteresis is highly undesirable in open-loop systems like this one. Even though this device met the accuracy requirement, it would not be selected for flight usage.

apparatus described Section 4.4.1 was installed in a thermal oven and cycled from $-20\,°C$ to $60\,°C$. Since these tests were primarily intended to test the MEMS device itself, the control electronics and driver board were left outside of the oven at room temperature.

Numerous challenges were encountered during these experiments. First, the thermal oven produces a great deal of vibration when running due to the circulation fans and compressor. This vibration would corrupt the angle estimation process due to blurring of the camera image. To work around this issue, we "soak" the test jig at a desired temperature then momentarily (10 min) disable the oven while the measurements were collected. The oven has sufficient thermal inertial to maintain the set point through this period.

Another significant challenge was that of thermal expansion and contractions of the test assembly. Even though all components were securely mounted to an optical breadboard, variations in material coefficients of thermal expansion (CTE) caused significant measurement deviations (approximately equivalent to 0.2 mrad in angle space). These deviations were first observed by monitoring the FSM's neutral position across temperature.

Despite the CTE-related deviations, it was still possible to perform relative measurements at different temperatures. A 32x32 two dimensional grid of points was measured at each temperature step. These grids would translate due to the CTE
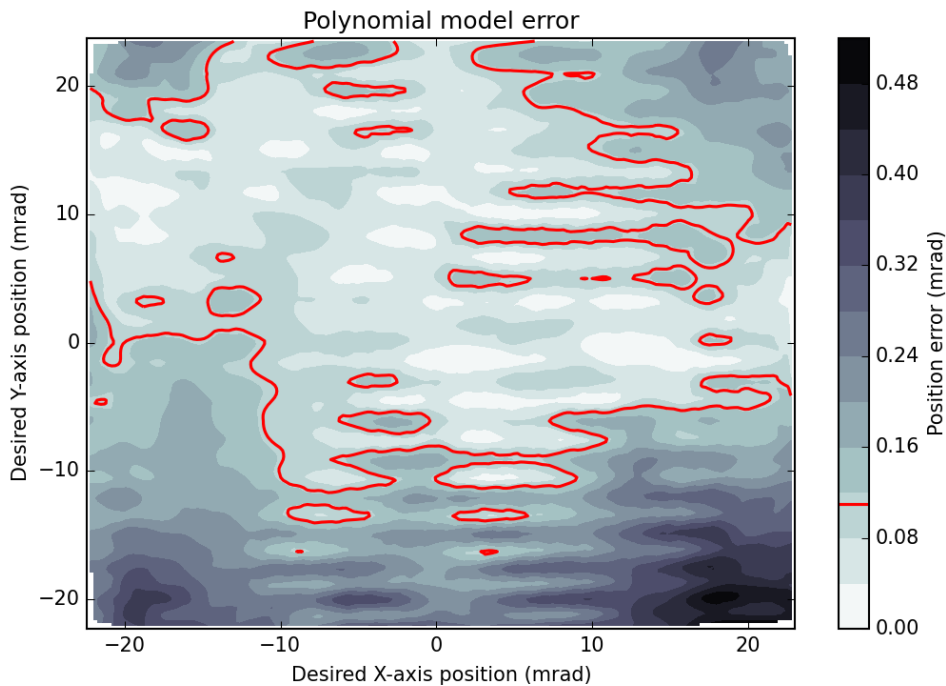
Figure 4-23: Contour plot showing position error between the polynomial FSM model and the two-axis data. The required performance threshold ($\pm 0.11\,\mathrm{mrad}$) is shown in red.

limitations of the apparatus, but could be realigned in post-processing using a least squares approach. This post-processing step rejects any absolute pointing errors that may be present in the device, but it still allows for comparative analysis of the 2D transfer functions across temperature.

Figure 4-25 shows the 2D position errors relative to the nominal grid points across temperature. One behavior that is apparent is that the device's voltage-to-angle transfer function appears to become more sensitive at lower temperatures. This is likely being caused by CTE effects in the electrostatic actuator mechanisms: lower temperatures cause contraction of the capacitive actuator structures, which increases the force imparted by the actuator for a given voltage. Without temperature compensation, the device is just above specified repeatability accuracy ($\pm 0.11\,\mathrm{mrad}$ 3-σ) at the low end of the operating temperature regime. Incorporating lookup tables for coarse temperature ranges (e.g., for every $10\,^\circ\mathrm{C}$ range) would likely be an effective way to compensate for this behavior of the device.

The measurement testbed should be redesigned to address the presumably CTE-related drift issues.Once these are corrected it will be enable absolute measurements of mirror angle relative to device package (which presumably will be rigidly mounted to the optics bench in the flight design). Alternatively, it may be possible to model the package (ceramic) and die attachment materials of the device itself to gain insight into any drifts that may arise due to device material CTE issues.
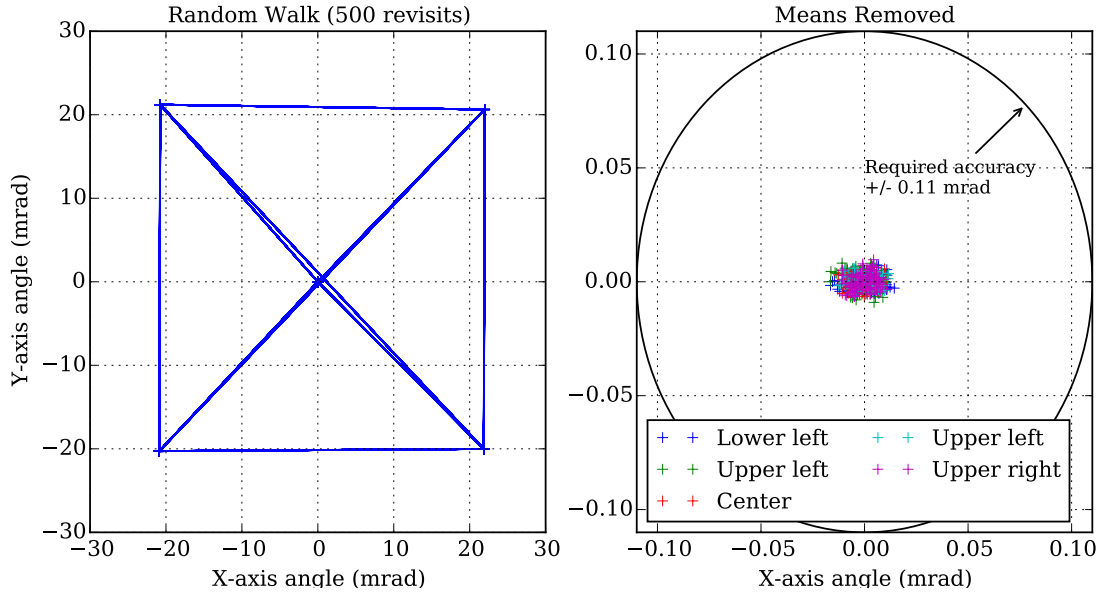
Figure 4-24: A random walk between five points in the FSM's range was used to measure position repeatability. The right-hand plot is the same data with the mean removed. The points are clustered well within(± 0.028 mrad 3-σ) the required accuracy region.

4.6 Validation Summary

This chapter has provided empirical results that validate critical aspects of the laser-com terminal design. The effectiveness of the transmitter to generate high fidelity optical waveforms for the modulation modes of interest was demonstrated. This included characterization of the FBG filter used to improve the seed signal extinction ratio to > 40 dB, which is adequate for the PPM modulation modes planned for this system (PPM-8 through PPM-128). The overall power consumption of the transmitter, which represents 80% of the lasercom terminal's power budget, was also measured. We also confirmed the efficiency of a path-to-flight TEC controller. The transmitter was augmented with a loopback receiver which allowed measurement of BER curves using the intended APD/TIA receiver module. These measurements showed new transmitter-to-receiver operation within 3 dB of theory, giving credence to the accuracy of receiver noise analysis used in the system link budget. The loopback receiver functionality was also expanded for use during the mission to provide built-in self-test functionality. The BIST design can validate performance of the transmitter even if other aspects (e.g., pointing, acquisition and tracking) are not able to meet mission requirements. The BIST features can also be used to close transmitter control loops, such as those needed to align the seed laser with the FBG filter. Finally, we presented preliminary thermal testing results showing the FSM repeatability behavior across the $0\,°C$ to $40\,°C$ operating range.
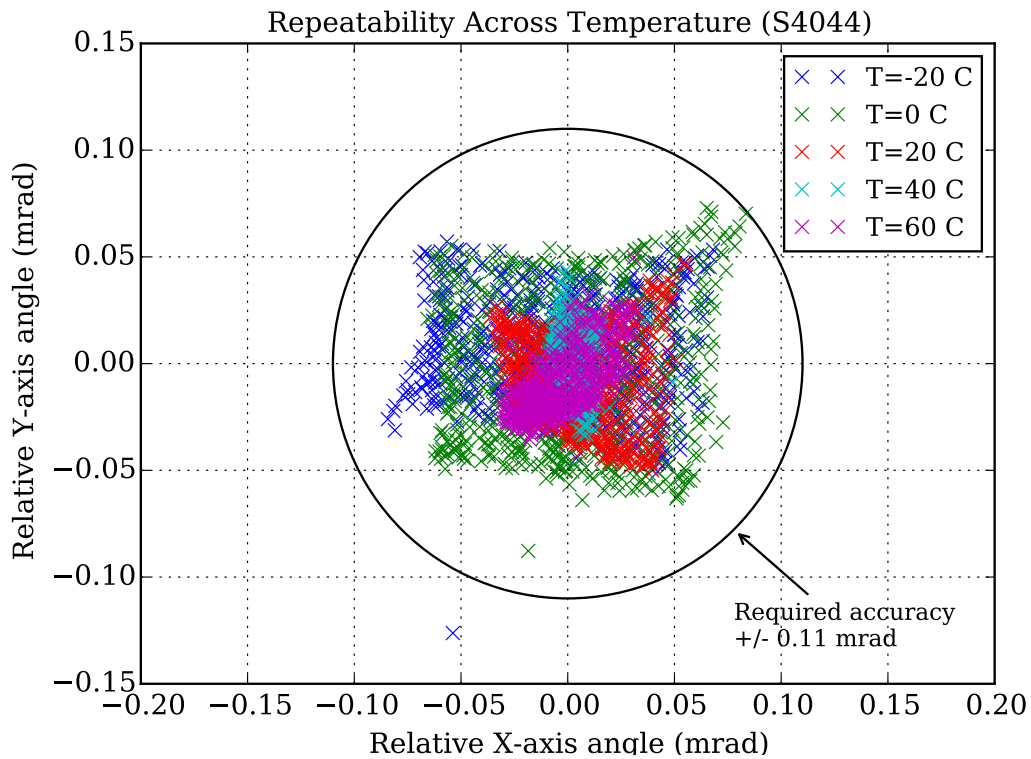
Figure 4-25: Position repeatability across temperature sampled on a 32x32 point grid across the field of regard of the device. At T=0 °C and T=−20 °C the device is slightly out of specification at ±0.15 mrad and ±0.13 mrad (3-σ), respectively.

Chapter 5

Path To Flight & Conclusions

This chapter summarizes the remaining design and analysis activities that are necessary to implement a flight demonstration of the lasercom system. First we describe the remaining engineering work that is necessary to field an on-orbit demonstration. Second, interface requirements between the host CubeSat and the terminal are also described at a high level. We close with a discussion of the applications that are enabled by lasercom technology on CubeSats and describe some directions for future research.

5.1 Remaining Implementation Tasks

Even though this thesis has addressed the key implementation gaps, notably through the development of a compact optical transmitter and the qualification of a fine-steering solution, there is still a significant amount of engineering ahead to realize a packaged terminal design that is ready for integration with a CubeSat. This section summarizes the remaining implementation tasks and provides suggested approaches for addressing them.

5.1.1 Miniaturization, Integration and Packaging

The main building blocks of the lasercom terminal design (e.g., EDFA, seed laser, FSM, etc.) are identical to the components that would be used in a flight demo, however, many of these devices require supporting infrastructure such as custom circuit boards and mounts. For laboratory experimentation, we used many vendor-provided mounting jigs and evaluation boards. For the flight design it will be necessary to design custom circuit boards and mounts to integrate these devices into the 0.5U form factor. We expect these to be relatively straightforward from an engineering perspective but note that the terminal mass budget is a rough estimate at this point and needs refinement.

The mechanical supports for the optical components, namely the structure that connects the beacon camera (receive aperture) to the FSM assembly (transmit aperture), need to be designed to survive launch and provide consistent alignment across

operating temperature range. Because the beacon camera field of view is much larger relative to the FSM field of regard (Figure 3-5) there is ample "margin" for misalignment between the two apertures, roughly $\pm 1.5°$. An on-orbit calibration procedure, based on a spatial (e.g., raster or spiral) scan along with ground station power measurements, will be used to determine the alignment between the two apertures. Development of this calibration process, specifically the scan rates and how those relate to other channel-induced power fluctuations, is a area of future research.

Another area of future work pertains to the various fiber optic components used in the design. Although some effort has been made to provide clearance for fiber routing within the design (i.e., alteration of the EDFA chassis to change the fiber egress points to a more convenient location), it would be prudent to develop a 3D model to understand how this routing will be accomplished in the design. This model can also be used to plan the assembly process for the terminal and to minimize (or even eliminate) the number of fiber optic connectors in the design. Unlike larger lasercom systems, even the volume occupied by a common FC/PC fiber junction is significant in this application. Fused splices between components in the optical train are preferable provided they do not hinder the assembly process[1].

5.1.2 Pointing, Acquisition and Tracking

This thesis has only covered the basic building blocks (e.g., fine steering mechanism and beacon camera) that are needed for the lasercom system's pointing, acquisition and tracking (PAT) process. Further development, simulation, and validation of the end-to-end PAT system is the thesis topic of graduate student Kathleen Riesing [99, 114].

5.1.3 Communication Data Processing

The communication link performance tests presented in this thesis only considered uncoded link performance. The flight design needs to incorporate framing, forward error correction (FEC) and interleaving techniques to combat channel effects and to provide a means for clock and data recovery. These features will be implemented in the FPGA.

The framing process groups symbols (i.e., PPM symbols) in a systematic way and provides modulation features (e.g., pilot sequence and guard slots) that are used by the clock and data recovery system to resolve timing ambiguities between the transmitter and receiver. The interleaver, which serves to temporally de-correlate channel fades, will likely be provided by a convolution interleaver. Convolutional interleavers are desirable because they have a compact memory format (half that of a block interleaver) and single-variable alignment (block interleavers have dual-variable alignment requirements). Finally, a low-complexity FEC such as $RS(255, 239)$ will provide near

---

[1]We do admit that the extra fiber connections added by the BIST functionality (Section 4.3.2) complicate this aspect of the design, however, being able to validate the fully-integrated design is worth the effort.

error-free output for an input signal with 1×10^{-4} bit error rate (consistent with link budget analysis) while only requiring 7% overhead.

Currently the FPGA only incorporates the modulation and BIST functionality, however, the device has ample resources (i.e., logic cells, external memory, etc) to host the other data processing features. Open-source implementations for the interleaver and FEC are available that can be used to accelerate the this integration effort. Once integrated, it would be worthwhile to test the effectiveness of the codes through additional bit error rate testing across a simulated channel (e.g., a variable optical attenuator modulated with a log-normal fading time series). It will also be necessary to incorporate a bulk memory to store telemetry from the host spacecraft that is waiting for a downlink opportunity.

5.1.4   Ground Station

For an initial flight demonstration, it would be most efficient to leverage an existing optical ground station. As designed, the system is nearly compatible with the Optical Communication Telescope Laboratory run by NASA JPL in support of the OPALS mission to the ISS. This ground station incorporates a telescope mount that is capable of tracking LEO objects. The downlink wavelength used for OPALS was also 1550 nm so the acquisition and tracking optics (camera and fine-steering mirror) can likely support our system. The uplink beacon wavelength for OPALS would need to be modified to operate at 850 nm instead of 975 nm since our design uses an uncooled Si focal plane array that has poor QE at 975 nm[2].

To detect the communication signal, the ground station would need to be retrofitted with a free-space coupled variant of the APD/TIA module that was tested in this thesis. A clock and data recovery (CDR) circuit, likely custom designed for the PPM modulation format used in this system, would need to be implemented and installed. Alternatively, it may be possible to over sample (e.g., $f_s > 2f_{slot}$) the output of the APD/TIA with a high-speed analog to digital converter and then perform CDR, deframing and decoding in software.

5.2   Host Spacecraft Interfaces

The lasercom terminal design presented in this thesis has been structured to be compatible with the "typical" 3U CubeSat. In doing so, a variety of assumptions have been made about the capabilities of the host. If this terminal were commercialized, these details would be captured in a host spacecraft interface control document.

5.2.1   Attitude Control Interfaces

The host spacecraft attitude determination and control systems (ADCS) acts as the coarse stage in the lasercom system design and must provide pointing and slew per-

---

[2]OPALS employed a cooled CCD detector as the uplink beacon receiver focal plane array, however, the designers of that project had a much less constraining power budget.

formance parameters as specified in Table 2.2. During initial acquisition of the laser-com beacon signal, the host ADCS is responsible for translating the CubeSat from mission-defined attitude into an attitude where the beacon camera is pointed towards the ground station. This maneuver could have implications for the attitude sensor requirements of the host. For example, some CubeSats rely on narrow field of view earth horizon sensors. Depending on the orientation of these sensors, they may not be able to maintain "lock" throughout this critical maneuver.

Once the lasercom terminal's beacon camera has acquired the signal from the ground station, additional ground-station-relative attitude error knowledge is available on board the CubeSat. The host-to-terminal interface should have a provision for relaying this attitude knowledge (i.e., bore sight error and derivative terms) to the host ADCS. This additional knowledge will allow the sensing-limited host ADCS to dramatically improve its pointing performance.

The MEMS FSM devices that are used in the lasercom terminal are resonant at around $1\,kHz$. Care should be taken to ensure that these resonances are not excited by the host ADCS (e.g., from reaction wheel vibrations). It may be necessary to isolate the terminal's optical assembly with passive vibration damping mounts.

Precision orbit determination is also required for this application. Recent studies have cast doubt on the accuracy and reliability of publicly-available orbit determination solutions (e.g., JSPoC), especially at lower orbits ($< 450\,km$) [77]. GPS-based orbit determination is still an uncommon feature on most satellites and we are hesitant to levy that requirement on the host CubeSat. Instead, we would recommend that the low-rate RF transceiver incorporate an incoherent two-way ranging function which have recently been shown to yield $0.5\,km$ (1-σ) orbit determination accuracy.

5.2.2 Electrical Interfaces

Power

The host CubeSat is responsible for generating power for the lasercom terminal. The $10\,W$ of power required by the terminal during transmission can easily be satisfied with one of the numerous COTS CubeSat power system solutions (e.g., Clyde Space, Pumpkin, GomSpace). The lasercom terminal design would likely be designed to accept an unregulated bus voltage (commonly $7.2\,V$) which would be internally converted into voltages required by the internal components. This approach allows the designer of the lasercom terminal to account for DC/DC conversion efficiency and invest extra effort in optimizing these parameters on high-power loads (e.g., the EDFA which is powered from a $5\,V$ bus).

Command & Data

The command and data interfaces are used to transfer telemetry (downlink direction) and commands (uplink direction) between the lasercom terminal and the on-board computer of the host CubeSat. These interfaces will also be used to transfer attitude determination and control knowledge between the fine stage (FSM) and coarse stage

(host ADCS). We have not selected a specific protocol for this interface. However, the data rate of this interface should be sufficient to allow real-time transfer of telemetry from the host to the lasercom terminal (i.e., as it is generated). The lasercom terminal should be responsible for adding forward error correction bits and interleaving to the telemetry stream before it is stored in a bulk memory (e.g., flash) where it awaits downlink (Figure 2-2).

5.2.3   Mechanical & Thermal Requirements

Mechanical and thermal interface requirements for the lasercom terminal will depend strongly on the flight packaging scheme that is developed. At a minimum, the mechanical interface between the lasercom terminal and the host spacecraft needs to ensure a alignment between the ADCS reference frame and the lasercom terminal's reference frame. This alignment specification would be derived from the coarse stage performance ($\pm 1.0°$) rather than the fine stage performance, so we do not anticipate this to be a hard requirement to satisfy.

The lasercom terminal has a $0°$ to $40°$ operating temperature range. This was derived from on-orbit data from prior CubeSat missions, so we do not expect it to be a challenging requirement either. The thermal design of the terminal as well as the host spacecraft should account for the transient nature of terminal operations (e.g., 5 min every 90 min, assuming a system with one ground station).

5.3   Closing Remarks

In this thesis we have designed and prototyped a solution to address one of the central limitations of CubeSat technology today: high-speed, power-efficient communications. Existing laser communications technologies were reviewed and mapped onto CubeSat capabilities (e.g., pointing performance and SWaP). During this process, we identified two significant implementation gaps that stood in the way of realizing the link-efficiency benefits of lasercom: the lack of suitable fine-steering solutions, and the unavailability of compact high-rate optical transmitters. Solutions were developed to address these implementations gaps, prototyped, and validated in the lab. Along the way, many of the design decisions were driven by the pragmatic COTS-based approach common to most aspects of CubeSat design.

For a flight demonstration, some work lies ahead. Additional engineering effort, particularly with regard to packaging and integration, are likely to be a significant portion of this work. Further development of the pointing, acquisition and tracking (PAT) procedures is also necessary and being pursued in parallel by another graduate student. Finally, it will be necessary to conduct environmental testing on the packaged terminal design to ensure robustness to both on-orbit (e.g., thermal) and launch-induced (e.g., shock and vibration) stresses.

The design presented in this thesis is currently limited by achievable pointing performance. As PAT performance improves with time, the laser transmitter will

eventually become the limiter due to processing electronics limitations[3]. Once this limit is reached, the next step will be to follow in the steps of fiber telecommunications systems by adopting wavelength diversity (also known as wavelength division multiplexing or WDM).WDM can be used to provide even higher data rates while keeping electrical signaling rates within the capabilities of modern FPGAs. Given adequate pointing performance, a four wavelength WDM design could conceivably provide 10 Gbps link rates while maintaining the desired COTS-based approach.

Looking ahead, high-rate power-efficient communications is a vital capability for CubeSats as remote sensing platforms. Miniaturization of higher resolution sensors, particularly hyperspectral imagers, will certainly increase demand for better communication solutions. Additionally, spectrum crowding and regulatory difficulties are likely to diminish the viability of RF solutions especially as the LEO regime becomes more crowded with CubeSats. Unless there is a dramatic shift in the regulatory environment surrounding RF solutions, lasercom is certainly the only long-term solution to the high-rate communications problem.

---

[3]The current FPGA-based design provides modulation rates up to 600 Mbps, however, similar FPGAs can achieve 2.5 Gbps modulation rates using specialty multi-gigabit transceivers.

Appendix A

Receiver Performance Analysis

This section describes the receiver performance analysis that was completed for the system. This analysis assumes a PPM modulated, average-power-limited transmitter with finite extinction ratio (ER). The receiver is an avalanche photodiode, transimpedance amplifier (APD-TIA). Perfect clock recovery is assumed in this analysis.

For PPM modulation, the relationship between the bit error rate ($P_{bit,error}$) and the symbol error rate ($P_{sym,error}$) is

$$P_{bit,error} = \frac{M}{2(M-1)} P_{sym,error} \tag{A.1}$$

since each symbol encodes $\log_2 M$ bits of information.

One advantage of PPM modulation over OOK is that it is "self thresholding." PPM receivers simply need to pick the slot with the highest intensity/power. It is not necessary for the receiver to determine the optimal threshold between the "0" and "1" states (e.g., in an OOK receiver).

Symbol errors arise when the signal slot is not the slot with the highest intensity (e.g., due to background light or electronics noise) or when all slots have equal power (in which case the receiver guesses at random). A common analysis approach is to apply Boole's inequiality (union bound) to the possibility that each of the non-signal slots is more intense than the signal slot [115]. If I_u is the intensity of slot u, and we assume that $u = 0$ is the intended signal slot, then

$$
\begin{aligned}
P_{sym,error} &\leq 1 - Pr\{I_0 > I_u \mid u \in \{1, \ldots, M-1\}, s = s_0\} \\
&\leq (M-1)Pr\{I_1 > I_0 \mid s = s_0\}
\end{aligned}
\tag{A.2}
$$

The system under study operates at high photon flux (> 100 photons per signal slot) and includes additive white Gaussian noise (AWGN) from the TIA. These factors are sufficient for us to assume that the light intensity in both the signal present ("mark") and signal absent ("space") slots follows a Gaussian distribution. Furthermore, we assume perfect slot clock recovery and that the transmitter output energy is contained within the intended slot. Thus, all slots are independent and identically distributed Gaussian random variables.

With the Gaussian approximation, we can apply Q-factor analysis [35] to find

$P_{sym,error}$ given details of the means and variances of the "mark" and "space" slots with:

$$P_{sym,error} \leq (M-1)Q\left\{\frac{\mu_1 - \mu_0}{\sqrt{\sigma_0^2 + \sigma_1^2}}\right\} \tag{A.3}$$

The mean signal values (in amperes) are defined as

$$\begin{aligned}
\mu_0 &= R(\lambda)g(P_0 + P_{bg}) \qquad [\text{A}] \\
\mu_1 &= R(\lambda)g(P_1 + P_{bg}) \qquad [\text{A}]
\end{aligned} \tag{A.4}$$

where P_0 and P_1 are the "mark" and "space" optical powers, $R(\lambda)$ is the APD's responsivity in A W^{-1} and g is the APD's gain. The background power, P_{bg}, cancels in the numerator of the Q-factor analysis and is only included for clarity. Both P_0 and P_1 incorporate correction for the transmitter's finite ER:

$$\begin{aligned}
P_0 &= P_{tx,avg}\left[1 - \frac{1}{M}\left(1 - \frac{1}{ER}\right)\right]^{-1} \qquad [\text{W}] \\
P_1 &= P_{tx,avg}\left[\frac{1}{M} + ER\left(1 - \frac{1}{M}\right)\right]^{-1} \qquad [\text{W}]
\end{aligned} \tag{A.5}$$

Signal variances, which capture the various noise sources in the system, including shot noise and Johnson (thermal) noise from the TIA are defined as

$$\begin{aligned}
\sigma_0^2 &= 2qR(\lambda)g^2 F(P_0 + P_{bg})f_{NEB} + \sigma_{amp}^2 \qquad [\text{A}^2] \\
\sigma_1^2 &= 2qR(\lambda)g^2 F(P_1 + P_{bg})f_{NEB} + \sigma_{amp}^2 \qquad [\text{A}^2]
\end{aligned} \tag{A.6}$$

where q is the charge of an electron, F is the APD excess noise factor, f_{NEB} is the noise equivalent bandwidth of the APD-TIA module, and σ_{amp}^2 is the APD-TIA noise contributions.

APD noise specifications, which quantify both multiplied and unmultipied dark current as well as additive Johnson noise, are poorly standardized between vendors [116]. The APD under consideration for this application is a Voxtel RDC1-NJAF with a $200\,\mu\text{m}$ senstive area and a $300\,\text{MHz}$ bandwidth. For this particular APD, the vendor provides a noise equivalent power (NEP) which specifies amplifier noise in terms of an equal power input optical signal. An excess noise factor (F) is also specified which captures effect of the (stochastic) multiplication process on the shot noise of the system. The device test report for the unit purchased reports an NEP of $2.8\,\text{nW}$ at $g = 20$ and excess noise factor $F = 4.3$. The APD-TIA noise contributions σ_{amp}^2 are defined as

$$\sigma_{amp}^2 = (\text{NEP} * R(\lambda) * g)^2 \qquad [\text{A}^2] \tag{A.7}$$

which assumes that the receiver sees the APD's full noise bandwidth.

APD-TIA noise is primarily white so many direct detection receivers follow the

APD-TIA with a filter that is matched to the communication waveform. The present analysis does not include this noise mitigation technique. The PPM waveform under consideration has a slot rate of $200\,\mathrm{MHz}$ whereas the APD-TIA has around $300\,\mathrm{MHz}$ of signal bandwidth. Matched filtering, which balances signal attenuation against noise bandwidth, could potentially provide about $3\,\mathrm{dB}$ of SNR improvement.

A.1 Calculating Power Required at Receiver

Given a target bit error rate, $P_{bit,error}$, and knowledge of the optical background power, P_{bg}, it is possible to calculate the required optical signal power P_1. By combining eq. (A.1) with eq. (A.3) and solving for the Q function's parameter, we obtain the required Q-factor, q_{req}:

$$q_{req} \geq Q^{-1} \left\{ \frac{2}{M} P_{bit,error} \right\} = \frac{\mu_1 - \mu_0}{\sqrt{\sigma_0^2 + \sigma_1^2}} \tag{A.8}$$

Further substitution of eq. (A.4) and eq. (A.6) allows us to solve for μ_1 and subsequently P_1. Assuming that shot noise is not significant, which is true for this application where amplifier noise is the dominant noise source, it is possible to obtain a closed-form solution:

$$\mu_1 \approx q_{req} \sqrt{\sigma_0^2 + \sigma_1^2} - \mu_0 \qquad [\mathrm{A}] \tag{A.9}$$

$$P_1 \approx \frac{\mu_1}{R(\lambda) * g} - P_{bg} \qquad [\mathrm{W}] \tag{A.10}$$

A.2 Mapping Slot Error Rate to Bit Error Rate

As described in Section 4.3.2, slot error rate for a pulse position modulation (PPM) system is trivially measured with an XOR operation and counters within the transmitter FPGA. Converting slot error rate (SLER) into bit error rate (BER) is desirable to enable comparison across various modulation orders (PPM-8, PPM-16, etc.) and with other communication system implementations.

In order to map SLER into BER, we first map SLER into symbol error rate (SER). We assume a threshold-based PPM receiver that compares the photodetector output to a voltage v_{th}. A correct PPM-M symbol consists of a mark slot with the observation V above the threshold and $M - 1$ slots with observations below the threshold. The probability of a correct symbol is given by:

$$\Pr(\text{symbol correct}) = 1 - SER = \Pr(V \geq v_{th})^1 \Pr(V < v_{th})^{M-1} \tag{A.11}$$

The receiver adjusts v_{th} to minimize the SLER probability[1], which corresponds to

---

[1]In the built-in self-test receiver implementation, this was implemented initially with a brute-force search of all available threshold settings ($v_{th} = V_{DAC}$). Heuristics involving simultaneous monitoring of the waveform duty cycle were later implemented to speed up this process.

a v_{th} such that:

$$\Pr(V \geq v_{th}) = \Pr(V < v_{th}) \tag{A.12}$$

Substituting Equation (A.12) into Equation (A.11):

$$1 - SER = (1 - SLER)^M \tag{A.13}$$

Finally we use the substitute Equation (A.13) into the SER-to-BER relationship for M-ary orthogonal modulations as described in [117, 27]:

$$BER = SER \cdot \frac{\frac{M}{2}}{M - 1} \tag{A.14}$$

giving:

$$BER = \left(1 - (1 - SLER)^M\right) \cdot \frac{\frac{M}{2}}{M - 1} \tag{A.15}$$

A.3 Theoretical Bit Error Rate Curves

The Python code below served as the basis for the link budgets and was used to calculate the theoretical BER curves used elsewhere in the thesis (e.g., Figure 4-15).

```python
"""
 Link Theoretical Models

 Author: Ryan Kingsbury

 This module contains functions that generate theoretical performance
 predictions for the lasercom link.  Most of these are based directly
 off the link budget spreadsheet.
"""
import scipy.constants
from scipy.special import erfc
from numpy import sqrt,clip

import scipy.constants
from numpy import log2,log10

def Prx_to_BER(P_RX_dBm, M):
    """ Compute theoretical BER from received optical power

    Thermal noise from APD/TIA is dominant term.
    """
    q = scipy.constants.elementary_charge

    Pbg = 9.34e-13  # background light [W]

    # Receiver params
    M_APD = 20.0                # APD gain [unitless]
    R_APD = 1.00                # Responsivity [A/W]
    F = 4.3                     # Excess noise factor [unitless]
    NEP = 2.80e-9               # Noise equiv power across device BW [W]
    B = 300e6                   # Noise equiv bandwidth [Hz]

    # Extinction ratio
    ER_dB = 38.0                   # Transmitter extinction ratio [dB]
    ER = 10**(-ER_dB/10.0)
    off_ratio = (1.0/(M*ER)+(1.0-1.0/M))**-1
    on_ratio  = 1.0/((1.0/M)+ER*(1.0-(1.0/M)))

    # Covert average receive power into watts
    Prx = 0.001*(10**(P_RX_dBm/10.0))

    mu_on  = M_APD*R_APD*(Pbg + Prx*on_ratio)
    mu_off = M_APD*R_APD*(Pbg + Prx*off_ratio)
```

```python
        Namp = (M_APD*R_APD*NEP)**2  # amplifier/detector noise [A^2]
        sigma2_on  = 2*q*R_APD*(M_APD**2)*F*B*(Pbg+Prx* on_ratio) + Namp
        sigma2_off = 2*q*R_APD*(M_APD**2)*F*B*(Pbg+Prx*off_ratio) + Namp

        Qfactor = (mu_on - mu_off)/sqrt(sigma2_on+sigma2_off)

        # Symbol error rate from Q factor
        SER = (M-1)*0.5*erfc(Qfactor/sqrt(2))

        # Map symbol error rate into bit error rate
        BER = M/(2.0*(M-1))*SER

        return clip(BER,0,0.5)

def Prx_to_PPB_dB(P_RX_dBm, M, wavelength=1550e-9,slotrate=200e6):
    """ Convert received power to photons per bit """

    # Link paramters
    bitrate = (slotrate/M)*log2(M)

    # Covert average receive power into watts
    Prx = 0.001*(10**(P_RX_dBm/10.0))

    # Photons per second
    photon_rate = Prx/photon_energy(wavelength)
    PPB = photon_rate/bitrate
    PPB_dB = 10*log10(PPB)

    return PPB_dB

def SLER_to_BER(SLER,M):
    """ Convert slot error rate into bit error rate """
    return (1.0-(1.0-SLER)**M)*(M/2.0)/(M-1.0)

def slotrate_to_bitrate(slotrate,M):
    """ Calculate bitrate given slot rate and M"""
    return (slotrate/M)*log2(M)

def photon_energy(wavelength):
    """ Photon energy given wavelength in meters"""
    return scipy.constants.h*scipy.constants.c/(wavelength) # [joules]
```

Appendix B

Ground Network Design

The ground station network, a set of one or more compatible ground stations, is an important part of designing any satellite communication system. Factors such as satellite orbit, required latency (e.g., time-to-downlink) and regulatory restrictions all factor into the design of this network. Optical communication systems, and even some microwave radio systems, must also account for weather which can affect availability of ground stations.

Although the design presented in this thesis primarily focused on minimizing ground station complexity and cost, primarily through the use of COTS parts (e.g., APD detectors and small telescopes), we wanted gain insight into how an optical ground station network would be deployed. In particular, we wanted to assess the downlink latency for a constellation of LEO satellites to a network of strategically placed ground stations, even in the face of random weather outages. We also wanted to understand how latency improves as additional ground stations are added to the network.

A simulation was created for a constellation of LEO orbit satellites, a ground station network, and a stochastic weather availability model. The LEO satellites used in this study were based on published orbit information (two-line element sets) for the Planet Labs constellation of Earth imaging CubeSats. As of November 2014, this constellation consisted of 12 CubeSats in the ISS orbit and 11 CubeSats in a sun synchronous orbit. These are very common orbits for CubeSats because of ride-share opportunities to these orbits. An orbit propagator (PyEphem [118]) was used to compute the location of these satellites across a 30 day period.

A hypothetical ground station network consisting of 11 geographically dispersed ground stations was also created (Figure B-1). The locations of the ground stations were chosen to coincide with existing astronomical observatories since these locations typically have good atmospheric seeing conditions (desirable for free-space optical links) and existing infrastructure (power, internet connectivity, etc. for "backhaul" of data)[1]. A stochastic weather model was defined to simulate occasional ground station outages due to weather (e.g., cloud cover). This weather model was very simple: for each four hour period the weather was favorable with probability 0.75.

---

[1]Additional work is needed to understand if scattering of uplink beacon laser light would be objectionable to these observatories.

The four hour period was chosen to model the short term consistency of weather at each site. The weather at each site was assumed to be independent of all the other sites due to their geographic spacing [119, 120].
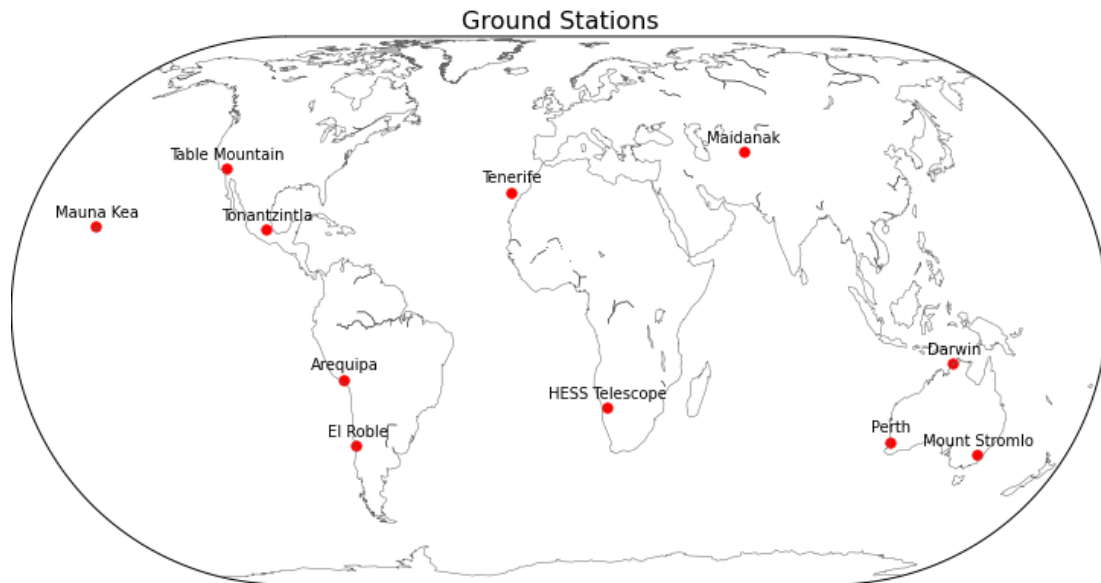
Figure B-1: Ground station locations used in the simulation were placed in locations with existing observatories.

Access times, or times when the satellite can "see" a ground station, were determined by checking for line-of-sight geometry. During a given access interval, three additional criteria were checked to determine if the access was viable for the optical link:

1. Favorable weather at the ground station site.

2. The satellite must be at least 20° above the horizon at the ground station site. This criteria is derived from the maximum acquisition range of the optical link as well as the poor optical channel conditions that exist at low elevation angles.

3. The satellite must remain above 20° for at least 120 s. This criteria is intended to capture the overhead needed for pointing acquisition and link synchronization.

The occurrence times of viable access times, or times when a give satellite is able to optically downlink telemetry, were recorded for latency analysis. Over the 30 day simulation period, there were a total of 10,000 access events for the constellation with the 11 station ground network.

Latency can be measured in a variety of ways. For this analysis, we consider the worst-case latency which we define as the time between viable access opportunities. This is roughly equivalent to the delay between when a bit of data is produced on the satellite and the next downlink opportunity. Many remote sensing missions (e.g.,

weather satellites) carry data timeliness requirements, which is what led us to this metric.

The latency metric is highly dependent on the number of ground stations available in the network. Since it is unlikely that a demonstration mission would have an 11 station network, we wanted to understand how latency is improved as the ground station network is deployed. To do this, we computed the max-latency metric for all subsets of the 11 station ground network (Figure B-2)[2].
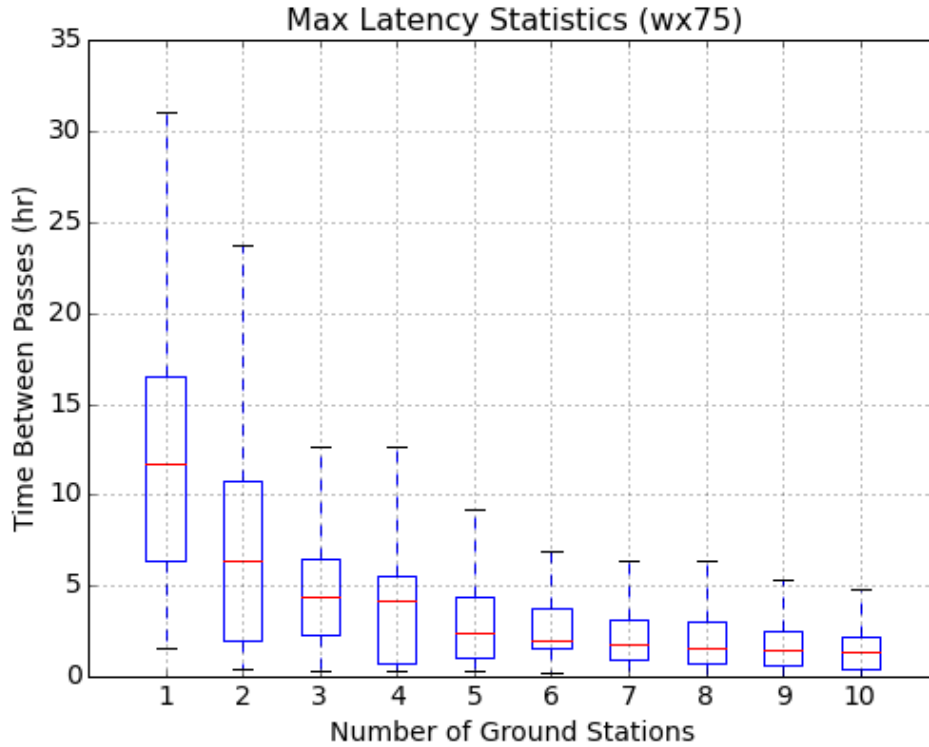
Figure B-2: Maximum latency for the constellation of satellites assuming a ground station availability of 75%. The boxes represent the the inter-quartile range, the red line is the median, and the whiskers represent the full range of data points.

With a small ground station network, latency statistics are primarily constrained by the footprint of the LEO satellite. A modest network of 4 or 5 ground stations is able to provide better than 12 hour worst-case latency, even with 25% weather outages at each of those ground stations. The results also show that even with a very large ground network, it is not feasible to achieve real-time coverage for constellation. Again, this is due to the limited footprint size of LEO satellites in this direct-downlink system. Cross-links between satellites would be necessary to provide real-time access.

---

[2]All possible permutations of ground stations were considered and the best subset (measured in terms of 90th percentile of max latency) for each network size was chosen.

Bibliography

[1] Isaac I Kim, Brian Riley, Nicholas M Wong, Mary Mitchell, Wesley Brown, Harel Hakakha, Prasanna Adhikari, and Eric J Korevaar. Lessons learned for STRV-2 satellite-to-ground lasercom experiment. In *Photonics West 2001-LASE*, pages 1–15. International Society for Optics and Photonics, 2001.

[2] Toshihiro Kubo-oka, Hiroo Kunimori, Hideki Takenaka, Tetsuharu Fuse, and Morio Toyoshima. Optical communication experiment using very small optical transponder component on a small satellite RISESAT. In *Proc. International Conference on Space Optical Systems and Applications (ICSOS)*, 2012.

[3] Yuka Mizoguchi, Kaihua FENG, Takanori Soda, Toshiki Otsuka, Tatsuro Kinoshita, Kohei Nishimoto, Yoshiyuki Kawamura, and Takushi Tanaka. Observation of the LED signal from FITSAT-1. In *UN/Japan nano satellite symposium*, 2012.

[4] Siegfried Janson and Richard Welle. The NASA optical communication and sensor demonstration program. In *AIAA Small Satellite Conference*, 2013.

[5] Hamid Hemmati. *Near-earth laser communications*. CRC Press, 2009.

[6] Richard S Vodhanel, Aly F Elrefaie, MZ Iqbal, Richard E Wagner, J Gimlett, and Shinji Tsuji. Performance of directly modulated DFB lasers in 10-Gb/s ASK, FSK, and DPSK lightwave systems. *Lightwave Technology, Journal of*, 8(9):1379–1386, 1990.

[7] Yoshinori Arimoto, Morio Toyoshima, Masahiro Toyoda, Tetsuo Takahashi, Motokazu Shikatani, and Kenichi Araki. Preliminary result on laser communication experiment using (ETS-VI). In *Photonics West'95*, pages 151–158. International Society for Optics and Photonics, 1995.

[8] Jose Romba, Zoran Sodnik, Marcos Reyes, Angel Alonso, and Aneurin Bird. ESA's bidirectional space-to-ground laser communication experiments. In *Optical Science and Technology, the SPIE 49th Annual Meeting*, pages 287–298. International Society for Optics and Photonics, 2004.

[9] Takashi Jono, Yoshihisa Takayama, Nobuhiro Kura, Koichi Ohinata, Yoshisada Koyama, Koichi Shiratama, Zoran Sodnik, Benoit Demelenne, Aneurin Bird, and Katsuyoshi Arai. OICETS on-orbit laser communication experiments. In

Lasers and Applications in Science and Engineering, pages 610503–610503. International Society for Optics and Photonics, 2006.

[10] CalPoly San Luis Obispo. Cubesat design specification. Technical report, CalPoly San Luis Obispo, Feb 2014.

[11] Spaceflight Incorporated. Space flight services pricing plans. `http://spaceflightservices.com/pricing-plans/`. Online; accessed 12-May-2015.

[12] Daniel Selva and David Krejci. A survey and assessment of the capabilities of cubesats for earth observation. *Acta Astronautica*, 74:50–68, 2012.

[13] Hamid Hemmati and David Caplan. Optical satellite communications. *Optical Fiber Telecommunications Volume VIB: Systems and Networks*, page 121, 2013.

[14] Steven Constantine, Laura E Elgin, Mark L Stevens, Joseph A Greco, Kenneth Aquino, Daniel D Alves, and Bryan S Robinson. Design of a high-speed space modem for the lunar laser communications demonstration. In *SPIE LASE*, pages 792308–792308. International Society for Optics and Photonics, 2011.

[15] Don M Boroson, Joseph J Scozzafava, Daniel V Murphy, Bryan S Robinson, and H Shaw. The lunar laser communications demonstration (LLCD). In *Space Mission Challenges for Information Technology, 2009. SMC-IT 2009. Third IEEE International Conference on*, pages 23–28. IEEE, 2009.

[16] William Blackwell, G Allen, C Galbraith, R Leslie, I Osaretin, M Scarito, Mike Shields, E Thompson, D Toher, D Townzen, et al. MicroMAS: A first step towards a nanosatellite constellation for global storm observation. In *Proceedings of the USU/AIAA Conference on Small Satellites*, 2013.

[17] Christopher John Lowe, Malcolm Macdonald, and Stephen Greenland. Through-life modelling of nano-satellite power system dynamics. In *64th International Astronautical Congress 2013*, pages Article–IAC, 2013.

[18] Dae Young Lee, James W Cutler, Joe Mancewicz, and Aaron J Ridley. Maximizing photovoltaic power generation of a space-dart configured satellite. *Acta Astronautica*, 111:283–299, 2015.

[19] Karan Sarda, Cordell Grant, Stuart Eagleson, Daniel D Kekez, and Robert E Zee. Canadian advanced nanospace experiment 2 orbit operations: two years of pushing the nanosatellite performance envelope. In *ESA Small Satellites, Services and Systems Symposium*, 2010.

[20] Michael Aherne, Tim Barrett, Lucy Hoag, Eric Teegarden, and Rohan Ramadas. Aeneas–colony i meets three-axis pointing. In *25th Annual AIAA/USU Conference on Small Satellites*, 2011.

[21] Christopher Pong, Matthew W Knutson, David W Miller, Sara Seager, Sungyung Lim, Timothy C Henderson, and Shawn D Murphy. High-precision pointing and attitude determination and control on ExoplanetSat. In *AIAA Guidance, Navigation, and Control Conference*, 2012.

[22] Bryan Klofas. Cubesat radios: From kilobits to megabits. In *Ground System Architectures Workshop*, 2014.

[23] Brian Klofas and Kyle Leveque. A survey of cubesat communications systems: 2009-2012. In *CalPoly CubeSat Developers' Workshop*, 2013.

[24] M Nishio, Y Harada, S Teshima, T Mutou, F Hori, T Tokifuji, H Ujihara, and Y Sakamoto. In-orbit verification of a compact Ku-band transmitter for a pico-satellite. In *Microwave Conference Proceedings (CJMW), 2011 China-Japan Joint*, pages 1–2. IEEE, 2011.

[25] Kenta Tanaka, Takushi Tanaka, and Yoshiyuki Kawamura. Development of the cubesat FITSAT-1. In *UN/Japan nano satellite symposium*, 2012.

[26] Morio Toyoshima. Trends of research and development on optical space communications technology. In *Proceedings of IEICE General Conference*, 2006.

[27] David O Caplan. Laser communication transmitter and receiver design. *Journal of Optical and Fiber Communications Reports*, 4(4-5):225–362, 2007.

[28] Angel Alonso, Marcos Reyes, and Zoran Sodnik. Performance of satellite-to-ground communications link between ARTEMIS and the optical ground station. In *Remote Sensing*, pages 372–383. International Society for Optics and Photonics, 2004.

[29] D.L. Begley. Free-space laser communications: a historical perspective. In *Lasers and Electro-Optics Society, 2002. LEOS 2002. The 15th Annual Meeting of the IEEE*, volume 2, pages 391–392 vol.2, 2002.

[30] Paul A Lightsey. Scintillation in ground-to-space and retroreflected laser beams. *Optical Engineering*, 33(8):2535–2543, 1994.

[31] Eric Korevaar, John Schuster, Prasanna Adhikari, Harel Hakakha, Richard Ruigrok, R Steiger, Lee Fletcher, and Brian Riley. Description of STRV-2 laser-com flight hardware. In *SPIE Free-Space Laser Communication Technologies IX Proceedings*, volume 2990, pages 38–49, 1997.

[32] Takashi Jono, Yoshihisa Takayama, Koichi Shiratama, Ichiro Mase, Benoit Demelenne, Zoran Sodnik, Aneurin Bird, Morio Toyoshima, Hiroo Kunimori, Dirk Giggenbach, et al. Overview of the inter-orbit and the orbit-to-ground laser communication demonstration by OICETS. In *Lasers and Applications in Science and Engineering*, pages 645702–645702. International Society for Optics and Photonics, 2007.

[33] Nicolas Perlot, M Knapek, D Giggenbach, J Horwath, M Brechtelsbauer, Y Takayama, and T Jono. Results of the optical downlink experiment KIODO from OICETS satellite to optical ground station Oberpfaffenhofen (OGS-OP). In *Proc. SPIE*, volume 6457, pages 645704–1, 2007.

[34] Siegfried W Janson Richard P Welle. Cubesat-scale laser communications. In *National Space Symposium*, 2015.

[35] Stephen B Alexander. *Optical communication receiver design*, volume 37. Society of Photo Optical, 1997.

[36] David O. Caplan. Laser communication transmitter and receiver design. In Arun K Majumdar and Jennifer Crider Ricklin, editors, *Free-Space Laser Communications: Principles and Advances*, volume 2. Springer, 2010.

[37] Michael Swartwout. The first one hundred cubesats: A statistical look. *Journal of Small Satellites*, Vol 2, Num 2:213–233, 2014.

[38] Michael Swartwout. Cheaper by the dozen: The avalanche of rideshares in the 21st century. In *Aerospace Conference, 2013 IEEE*, pages 1–12. IEEE, 2013.

[39] Tam Nguyen. Laser beacon tracking for high-accuracy attitude determination. In *Proceedings of the AIAA/USU Conference on Small Satellites*, pages SSC15–x–x, 2015.

[40] General Environmental Verification Standard. NASA publication GSFC-STD-7000, 2005.

[41] Christopher Boshuizen, James Mason, Pete Klupar, and Shannon Spanhake. Results from the planet labs flock constellation. In *Proceedings of AIAA/USU Conference on Small Satellites*, 2014.

[42] Lionel Jacques. *Thermal design of the oufti-1 nanosatellite*. PhD thesis, University of Liège, 2009.

[43] IEEE Standards Board. *IEEE Standard for Environmental Specifications for Spaceborne Computer Modules (IEEE Std 1156.4-1997)*. IEEE, 1997.

[44] D Heynderickx, B Quaghebeur, E Speelman, and EJ Daly. ESAs space environment information system (SPENVIS): a WWW interface to models of the space environment and its effects. *Proc. AIAA*, 371, 2000.

[45] Allan J Tylka, JH Adams, Paul R Boberg, Buddy Brownstein, William F Dietrich, Erwin O Flueckiger, Edward L Petersen, Margaret A Shea, Don F Smart, and Edward C Smith. CREME96: A revision of the cosmic ray effects on micro-electronics code. *Nuclear Science, IEEE Transactions on*, 44(6):2150–2160, 1997.

[46] R. Kingsbury, F. Schmidt, K. Cahoy, D. Sklair, W. Blackwell, I Osarentin, and R. Legge. TID tolerance of popular cubesat components. In *Radiation Effects Data Workshop (REDW), 2013 IEEE*, pages 1–4, July 2013.

[47] Richard Netzer, Keith Avery, William Kemp, Alonzo Vera, Brian Zufelt, and David Alexander. Total ionizing dose effects on commercial electronics for cube sats in low earth orbits. In *Radiation Effects Data Workshop (REDW), 2014 IEEE*, pages 1–7. IEEE, 2014.

[48] Keith Avery, Jeffery Fenchel, Jesse Mee, William Kemp, Richard Netzer, Donald Elkins, Brian Zufelt, and David Alexander. Total dose test results for cubesat electronics. *Signal*, 25:7, 2011.

[49] Byung-Wook Yoo, Jae-Hyoung Park, IH Park, Jik Lee, Minsoo Kim, Joo-Young Jin, Jin-A Jeon, Sug-Whan Kim, and Yong-Kweon Kim. MEMS micromirror characterization in space environments. *Optics express*, 17(5):3370–3380, 2009.

[50] HR Shea. MEMS for pico-to micro-satellites. In *Proc. SPIE*, volume 7208, page 72080M, 2009.

[51] Herbert R Shea. Radiation sensitivity of microelectromechanical system devices. *Journal of Micro/Nanolithography, MEMS, and MOEMS*, 8(3):031303–031303, 2009.

[52] Herbert R Shea. Reliability of MEMS for space applications. In *MOEMS-MEMS 2006 Micro and Nanofabrication*, pages 61110A–61110A. International Society for Optics and Photonics, 2006.

[53] Robert Osiander, M Ann Garrison Darrin, and John L Champion. *MEMS and microstructures in aerospace applications*. CRC press, 2005.

[54] International Telecommunication Union. Radio regulations. *Radiocommunication Sector. ITU-R. Geneva*, 2012.

[55] William Marshall and Chris Boshuizen. Planet labs remote sensing satellite system. In *Proceedings of pre-Conference: CubeSat Developers' Workshop at the AIAA/USU Small Satellite Conference*, 2013.

[56] ANSI. *ANSI Z136.1: American National Standard for Safe Use of Lasers*. Laser Institute of America, 2007.

[57] International Electrotechnical Commission. *IEC 60825-1: Safety of Laser Products*. Laser Safety Group, 2001.

[58] Nanoracks Inc. Payload requirements discussions. Personal communication, 10 2014.

[59] Federal Aviation Administration. Order jo 7400.2g: Procedures for handling airspace matters, part 6, chapter 26 (outdoor laser operations). Technical report, US Department of Transportation, 2008.

[60] European Optical Ground Station (OGS), Tenerife, Spain. Operations discussions. Personal communication, 10 2014.

[61] Steven D. Kramer. The impact of predictive avoidance restrictions on astronomical observatories. Technical report, Institute for Defense Analysis, 2010.

[62] Bogdan V Oaida, William Wu, Baris I Erkmen, Abhijit Biswas, Kenneth S Andrews, Michael Kokorowski, and Marcus Wilkerson. Optical link design and validation testing of the optical payload for lasercomm science (OPALS) system. In *SPIE LASE*, pages 89710U–89710U. International Society for Optics and Photonics, 2014.

[63] Software Bisque. Paramount MYT robotic telescope mount, May 2015.

[64] RC Optical Systems. Commercial LEO tracker, May 2015.

[65] W Thomas Roberts and Malcolm W Wright. Deep-space optical terminals (DOT) ground laser transmitter (GLT) trades and conceptual point design. *The Interplanetary Network Progress Report*, 42(183):1–13, 2010.

[66] Isaac I Kim, Harel Hakakha, Prasanna Adhikari, Eric J Korevaar, and Arun K Majumdar. Scintillation reduction using multiple transmitters. In *Photonics West'97*, pages 102–113. International Society for Optics and Photonics, 1997.

[67] HG Rao, CA Browne, DO Caplan, JJ Carney, ML Chavez, AS Fletcher, JJ Fitzgerald, RD Kaminsky, G Lund, SA Hamilton, et al. Electronics design of a multi-rate DPSK modem for free-space optical communications. In *SPIE LASE*, pages 89710Y–89710Y. International Society for Optics and Photonics, 2014.

[68] Felix Arnold, Martin Mosberger, Johannes Widmer, and Fabio Gambarara. Ground receiver unit for optical communication between LADEE spacecraft and ESA ground station. In *SPIE LASE*, pages 89710M–89710M. International Society for Optics and Photonics, 2014.

[69] Frederic M Davidson and Xiaoli Sun. Slot clock recovery in optical PPM communication systems with avalanche photodiode photodetectors. *Communications, IEEE Transactions on*, 37(11):1164–1172, 1989.

[70] Kuo-Chia Alice Liu. *Stochastic performance analysis and staged control system designs for space based interferometers*. PhD thesis, Massachusetts Institute of Technology, 2003.

[71] C. Pong. *High-Precision Pointing and Attitude Estimation and Control Algorithms for Hardware-Constrained Spacecraft*. PhD thesis, Massachusetts Institute of Technology, 2014.

[72] Kathleen Riesing. Development of a pointing, acquisition, and tracking system for a cubesat laser communications module. Master's thesis, Massachusetts Institute of Technology, 2015.

[73] Stephen Arnold, James Armstrong, Clark Person, and Michael Tietz. QbX-the cubesat experiment. In *Proceedings of the 26th Annual AIAA/USU Conference on Small Satellites*, 2012.

[74] Siegfried W Janson, Brian S Hardy, Andrew Y Chin, Daniel L Rumsey, Daniel A Ehrlich, and David A Hinkley. Attitude control on the pico satellite solar cell testbed-2. In *Proceedings of the 26th Annual AIAA/USU Conference on Small Satellites*, 2012.

[75] Darren Rowen and Rick Dolphus. 3-axis attitude determination and control of the AeroCube-4 cubesats. In *AIAA/USU Conference on Small Satellites, 10th Annual CubeSat Developers' Workshop*, 2013.

[76] Blue Canyon Technologies Inc. *XACT High-Performance Attitude Determination for CubeSats Datasheet*.

[77] Kathleen Riesing. Orbit determination from two line element sets of ISS-deployed cubesats. In *Proceedings of the AIAA/USU Conference on Small Satellites*, pages SSC15–x–x, 2015.

[78] Francisco Eugenio and Ferran Marqués. Automatic satellite image georeferencing using a contour-matching approach. *Geoscience and Remote Sensing, IEEE Transactions on*, 41(12):2869–2880, 2003.

[79] Paul R Yoder. *Mounting Optics in Optical Instruments*, volume 181. Society of Photo Optical, 2008.

[80] Stephen G Lambert and William L Casey. *Laser communications in space.* Artech House Boston, USA, 1995.

[81] Xiaoming Zhu and Joseph M Kahn. Communication techniques and coding for atmospheric turbulence channels. *Journal of Optical and Fiber Communications Reports*, 4(6):363–405, 2007.

[82] DO Caplan, ML Stevens, and BS Robinson. Free-space laser communications: global communications and beyond. In *European Conference on Optical Communication*, 2009.

[83] DO Caplan, H Rao, JP Wang, DM Boroson, JJ Carney, AS Fletcher, SA Hamilton, R Kochhar, RJ Magliocco, R Murphy, et al. Ultra-wide-range multi-rate DPSK laser communications. In *Conference on Lasers and Electro-Optics*, page CPDA8. Optical Society of America, 2010.

[84] Shu Lin and Daniel J Costello. *Error control coding: fundamentals and applications*, volume 114. Pearson-Prentice Hall Upper Saddle River, 2004.

[85] Bryan Klofas. Cubesat communication system table. `http://www.klofas.com/comm-table/`, 2015. Online; accessed 13-Apr-2015.

[86] RM Gagliardi and G Prati. On gaussian error probabilities in optical receivers. *Communications, IEEE Transactions on*, 28(9):1742–1747, 1980.

[87] DO Caplan, JJ Carney, RE Lafon, and ML Stevens. Design of a 40 watt 1.55 μm uplink transmitter for lunar laser communications. In *SPIE LASE*, pages 82460M–82460M. International Society for Optics and Photonics, 2012.

[88] OPALS Team. Operations discussions. Personal communication, August 2014.

[89] DO Caplan, ML Stevens, DM Boroson, and JE Kaufmann. A multi-rate optical communications architecture with high sensitivity. *LEOS, November*, 1999.

[90] Emmanuel Desurvire. *Erbium-doped fiber amplifiers: principles and applications*. Wiley-Interscience, 2002.

[91] Telcordia. *GR-468-CORE: Generic Reliability Assurance Requirements for Optoelectronic Devices Used in Telecommunications Equipment*, 2 edition, Sept 2004.

[92] Neal W Spellmeyer, David O Caplan, and Mark L Stevens. Design for a 5-watt PPM transmitter for the mars laser communications demonstration. In *LEOS Summer Topical Meetings, 2005 Digest of the*, pages 51–52. IEEE, 2005.

[93] David O Caplan, Bryan S Robinson, Robert J Murphy, and Mark L Stevens. Demonstration of 2.5 Gslot/s optically-preamplified M-PPM with 4 photons/bit receiver sensitivity. In *Optical Fiber Communication Conference*, page PDP32. Optical Society of America, 2005.

[94] Chang-Hee Lee, Sang-Soo Lee, Hyang Kyun Kim, and Jung-Hee Han. Transmission of directly modulated 2.5-Gb/s signals over 250-km of nondispersion-shifted fiber by using a spectral filtering method. *Photonics Technology Letters, IEEE*, 8(12):1725–1727, 1996.

[95] D Mahgrefteh, PS Cho, J Goldhar, and HI Mandelberg. Penalty-free propagation over 600 km of non-dispersion-shifted fiber at 2.5 Gb/s using a directly laser modulated transmitter. In *Lasers and Electro-Optics, 1999. CLEO'99. Summaries of Papers Presented at the Conference on*, page 182. IEEE, 1999.

[96] David O Caplan, John J Carney, and Steven Constantine. Parallel direct modulation laser transmitters for high-speed high-sensitivity laser communications. In *CLEO: Applications and Technology*, page PDPB12. Optical Society of America, 2011.

[97] David O Caplan and John Carney. Power-efficient noise-insensitive optical modulation for high-sensitivity laser communications. In *CLEO: Science and Innovations*, pages SM4J–6. Optical Society of America, 2014.

[98] Steven Spector, Jeffrey M Knecht, Robert T Schulein, and David O Caplan. Silicon photonic filters for compact high extinction ratio power efficient (CHERPe) transmitters. In *CLEO: Science and Innovations*, pages SW1N–4. Optical Society of America, 2015.

[99] Kathleen Riesing. *Development of a Pointing, Acquisition, and Tracking System for a Nanosatellite Laser Communications Module.* PhD thesis, Massachusetts Institute of Technology, 2015.

[100] Newport. *Netport Fast Steering Mirror & Controller Manual, FSM-300-01.* Maryland Aerospace Inc., 2014.

[101] Eric Peters, Pratik Davé, Ryan Kingsbury, Meghan Prinkey, Anne Marinan, Evan Wise, Christopher Pong, Kerri Cahoy, William Thalheimer, Devon Sklair, et al. Design and functional validation of a mechanism for dual-spinning cubesats. *AIAA/USU Conference on Small Satellites*, Pre-conference Workshop, 2013.

[102] Joseph Kerivan Lane. *Control of a MEMS fast steering mirror for laser applications.* PhD thesis, Massachusetts Institute of Technology, 2012.

[103] Mirrorcle Technologies Inc. Product discussions. Personal communication, 10 2014.

[104] Barry L Stann, John F Dammann, Joseph A Enke, Pey-Schuan Jian, Mark M Giza, William B Lawler, and Michael A Powers. Brassboard development of a MEMS-scanned ladar sensor for small ground robots. In *SPIE Defense, Security, and Sensing*, pages 80371G–80371G. International Society for Optics and Photonics, 2011.

[105] DO Caplan, JJ Carney, JJ Fitzgerald, I Gaschits, R Kaminsky, G Lund, SA Hamilton, RJ Magliocco, RJ Murphy, HG Rao, et al. Multi-rate DPSK optical transceivers for free-space applications. In *SPIE LASE*, pages 89710K–89710K. International Society for Optics and Photonics, 2014.

[106] RS Vodhanel, Aly F Elrefaie, Richard E Wagner, MZ Iqbal, James L Gimlett, and S Tsuji. Ten-to-twenty gigabit-per-second modulation performance of 1.5-μm distributed feedback lasers for frequency-shift-keying systems. *Lightwave Technology, Journal of*, 7(10):1454–1460, 1989.

[107] Marko Labudovic and Jin Li. Modeling of TE cooling of pump lasers. *Components and Packaging Technologies, IEEE Transactions on*, 27(4):724–730, 2004.

[108] Linear Technology Corporation. *LTC1923: High Efficiency Thermoelectric Cooler Controller, datasheet*, Feb 2015.

[109] DO Caplan. A technique for measuring and optimizing modulator extinction ratio. In *Lasers and Electro-Optics, 2000.(CLEO 2000). Conference on*, pages 335–336. IEEE, 2000.

[110] NW Spellmeyer, CA Browne, DO Caplan, JJ Carney, ML Chavez, AS Fletcher, JJ Fitzgerald, RD Kaminsky, G Lund, SA Hamilton, et al. A multi-rate DPSK modem for free-space laser communications. In *SPIE LASE*, pages 89710J– 89710J. International Society for Optics and Photonics, 2014.

[111] Neal W Spellmeyer, Steven L Bernstein, Don M Boroson, David O Caplan, Andrew S Fletcher, Scott A Hamilton, Robert J Murphy, Marc Norvig, Hemonth G Rao, Bryan S Robinson, et al. Demonstration of multi-rate thresholded preamplified 16-ary pulse-position-modulation. In *Optical Fiber Communication Conference*, page OThT5. Optical Society of America, 2010.

[112] Alan D Kersey, Michael A Davis, Heather J Patrick, Michel LeBlanc, KP Koo, CG Askins, MA Putnam, and E Joseph Friebele. Fiber grating sensors. *Journal of lightwave technology*, 15(8):1442–1463, 1997.

[113] Michael K Cheezum, William F Walker, and William H Guilford. Quantitative comparison of algorithms for tracking single fluorescent particles. *Biophysical journal*, 81(4):2378–2388, 2001.

[114] Kathleen Riesing. Pointing, acquisition and tracking design discussions. Personal communication, 11 2014.

[115] Hien TT Pham and Ngoc T Dang. A comprehensive model for performance analysis of APD-based FSO systems using M-PPM signaling in atmospheric turbulence. *REV. J. Electron. Commun.*, 2:147–152, 2012.

[116] Voxtel. Avalance photodiode receiver performance metrics, technical note V803. Technical report, Voxtel Inc, Undated.

[117] John G Proakis, Masoud Salehi, Ning Zhou, and Xiaofeng Li. *Communication systems engineering*, volume 1. Prentice-hall Englewood Cliffs, 1994.

[118] Brandon Craig Rhodes. PyEphem: Astronomical ephemeris for python. *Astrophysics Source Code Library*, 1:12014, 2011.

[119] Gary S Wojcik, Heather L Szymczak, Randall J Alliss, Robert P Link, Mary Ellen Craddock, and Michael L Mason. Deep-space to ground laser communications in a cloudy world. In *Optics & Photonics 2005*, pages 589203– 589203. International Society for Optics and Photonics, 2005.

[120] Robert Link, Mary Ellen Craddock, and Randall J Alliss. Mitigating the impact of clouds on optical communications. In *Aerospace Conference, 2005 IEEE*, pages 1258–1265. IEEE, 2005.